SAPIENZA
UNIVERSITÀ DI ROMA

Inverse approach for load identification in structural dynamics

Silvia Milana

Dipartimento di Ingegneria Meccanica e Aerospaziale
Dottorato di Ricerca in Meccanica Teorica e Applicata

A thesis submitted for the degree of
Dottore di Ricerca

Supervisors
Prof. Antonio Culla

Prof. Annalisa Fregolent

December 2016

To my family

Abstract

Goal of this thesis is the identification of the external force field in the frequency domain at low and high frequency range.
At low frequency the solution of the investigated problem is carried out by modal analysis. Input-Output relationship between force and velocity is defined by using the Frequency Response Function (FRF) calculated both by modal expansion and measurements. The identification procedure is performed for deterministic and random loads.
By considering deterministic loads, the solution of this problem is obtained by the inversion of the FRF, that implies to deal with an ill-conditioning problem.
Since it can be shown that the ill-conditioning of FRF matrix is strictly related to the selection of the DoF considered on the structure, a procedure to investigate the best experimental setup that allows to identify the deterministic load is proposed, by using classical regularization techniques based on the Singular Values Decomposition (SVD). Then, with the same purpose the relationship between the modes contribute and the ill-conditioning of the problem is investigated.
Different input-output relationships from that used in the case of deterministic loads are adopted when random loads are considered. In fact, they are deduced by a probabilistic approach also for the solution of the direct problem. The results obtained by numerical simulation suggest that the identification of not deterministic loads requires a different methodology. So, a procedure based on the reduction of ill-conditioning it is not considered the conclusive approach; hence the issue has been tackled by a different modal formulation. In a first step the analysis of the coherence function allows to select the number of applied forces, once the position and the amplitude are identified. The validation of this proposed technique is tested in different experimental cases: Single Input Multi Output (SIMO) and Multi Input-Multi Output (MIMO). The numerical identification of deterministic and random loads is conducted also in the instance in which the measurement set of points do not overlap the excitation points.
Whilst the first part of the thesis is focused on the identification of deterministic and random loads at low frequencies, the second part is focused on the identification of random loads at high frequencies. Let us remind that a high frequency problem is one in which the wavelength of the waves propagating in the studied media is shorter than the characteristic dimension of the media itself. Therefore the solution of a high frequency problem by a classical technique implies the study of a very large number of degrees of freedom of the model. The consequence is a high computational cost and large uncertainty on the simulation results. Therefore the problem is tackled by using the Statistical Energy Analysis (SEA). The identification is performed in two steps. The first step considers the identification of a "*energy based*" model of the structure by using the Power Injection Method (this technique allows to carry out the SEA parameters of the structure by experimental tests). The second step is the identification of the power injected by using the identified model and solving an "*inverse problem*" of SEA.

CONTENTS

1 Force identification and connected issues **3**
1.1 The ill-conditioning in the force identification problem 4
1.1.1 Regularization techniques 5

2 Identification of deterministic forces at low-medium frequencies **10**
2.1 Identification of the best experimental setup 10
2.1.1 Numerical results 13
2.1.2 Results by experimental FRF 18
2.2 Reduction of ill-conditioning by a physical approach 25
2.3 Force identification: numerical results 28
2.3.1 Deterministic load 29
2.3.2 Not deterministic load 31

3 Identification by coherence based approach **40**
3.1 Theoretical background 40
3.2 Single input/ multi output model 46
3.2.1 SIMO identification: whole measurement points set 47
3.2.2 SIMO identification: reduced measurement points set 52
3.3 Multi input/ multi output model 57
3.3.1 MIMO identification: whole measurement points set 57
3.3.2 MIMO identification: reduced measurement points set 59

4 Identification by using Energy Based model **63**
4.1 Theoretical background of Statistical Energy Analysis 63
4.2 Power Injection Method 67
4.3 Identification of the injected power 69
4.4 Force model 70
4.5 Model parameters identification 71
4.6 Model validation and power identification 73
4.6.1 Single input/ multi output: experimental test 73
4.6.2 Multi input/ multi output: numerical test 80

4.7 "Rain-on-the-roof": experimental test 82

5 General conclusion **90**

INTRODUCTION

In several engineering applications the study of the vibration induced by external loads is fundamental. In fact, the knowledge of the force acting on a structure is basic, for example, to predict the response of the structure by numerical models (FEM,BEM) and to design control systems for the reduction of the vibrations either acting directly to reduce the external force, or as input of the control systems of the structure vibrations. Frequently the external forces can not be directly measured, so they must be identified by measurements of the structure response.
Since the identification procedure involves the inversion of the physical-mathematical model of the structure and the measurements of vibrations, corrupted by noise, the input of this procedure, the ill-conditioning of the model, is the main obstacle to the problem solution. Aim of this dissertation is to study how the position and the amplitude of external forces acting on a structure can be identified bypassing the ill-conditioning of the problem and its effects on the unpredictability of the load field. With this purpose, the investigation is focused on a solution of this kind of problem from an operative point of view.
In the first chapter, after a brief overview on the topic of this thesis, is presented the classical problem of load identification in frequency domain. The concept of ill-conditioning is introduced and some different regularization techniques, based on SVD, are proposed. The second chapter is focused on the study of the relationship between the ill-conditioning of the FRF matrix and the degrees of freedom taken into account for a low frequency problem when the solution of the investigated problem is performed by modal analysis. This relationship is firstly investigated through a numerical procedure, based on the singular values decomposition techniques, aimed to identify the optimal experimental setup to load identification. The results obtained from the numerical FRF are compared with the results obtained from the experimental one. In the second part of the chapter, the effect of the reduction of the degrees of freedom of the problem on the identification of multiple point force is investigated in two different condition: when the response of the structure is known in correspondence of the excitation points and when it is unknown. The numerical force identification is carried out for both deterministic and random loads. The results obtained for not deterministic loads suggest that the reduction of ill- conditioning can not be considered the conclusive approach.

Therefore in the third chapter a new operative procedure that allows to identify random loads is investigated. The procedure is performed in three steps: first the number of sources is established by an index based on the velocity coherence, then the position of the applied loads is identified and finally their amplitude. The identification of the position and the amplitude of the applied loads is carried out by an index named C_{vf}, computed as a virtual coherence between a dummy load, applied numerically on the structure, and the actual velocity.
The reciprocal of the frequency response function at the identified drive point is computed, so as to withdraw the ill-conditioning effect in correspondence of the identified position the amplitude of the load.
The identification procedure is conducted by using experimental measurement both for a single input multi output and for multi input multi output model. The obtained results confirm that this approach is a valid alternative, when the reduction of the ill-conditioning of the problem is not enough to obtain meaningful results.
The fourth chapter is focused on the identification at high frequencies. Let us remind that a high frequency problem happens when the wavelength of the waves propagating into the studied media is shorter than the characteristic dimension of the media itself. Therefore the solution of a high frequency problem by a classical technique implies the study of a very large number of DoFs of the model. The consequence is a high computational costs and large uncertainty on the simulation results. Therefore, the problem is tackled using an Energy Based model inspired by Statistical Energy Analysis balance equation. The procedure is entirely performed in operative conditions and consists of two steps. The first one is the identification of the energy based model performed by using Power Injected Method. The second step is the identification of the injected power by using the power balance equations. The last step is the identification of the power spectral density of the load by the knowledge of the injected power. In the second part of this chapter the experimental validation of the identified model and of the identification procedure are discussed. The results obtained from numerical and experimental tests suggest that an energetic approach is an interesting tool in the solution of the identification problems also at low frequency.

CHAPTER
ONE

FORCE IDENTIFICATION AND CONNECTED ISSUES

In the field of vibroacoustics, two different identification problems can be considered: the identification of applied loads on the structure by the knowledge of the responses and of the model, and the identification of the model of the structure by the knowledge of the applied loads and responses. Both these inverse problems, that sometimes present the same complexity, are open issues in structural dynamics [1].
By assuming the definition given by Hadamard [2], the inverse problems are ill-posed, the stability criterion is not satisfied and the solution is not unique. The introduction of the concept of generalized solution allowed to solve this problem that still remains ill-conditioned. The nature of ill-conditioning has been investigated by many authors. Hillary and Ewins investigated the relationship between the resonance frequencies and ill-conditioning [3], Fabumni established the relation between the force estimation error and the number of modes that contribute to the FRF at a certain frequency [4].
In the last decades, the external load identification issue was tackled widely, with the purpose to identify the actual position and the amplitude of external loads. Several approaches are proposed, some in frequency domain and some in time domain. Guyader and Pezerat developed the Force Analysis Technique (FAT) [5] based on the use of a finite difference scheme starting from the analytical equations of the structure; an early work focused on the identification of forces acting on a simple structure as a beam or a plate [6, 7]; successively the method was applied to more complex structures. The most evident advantage of this technique is that it does not require the knowledge of the dynamic behaviour of the whole structure. Indeed, the analysis depends on the studied area. In many applications, the filtering of the identified force is performed by a low-pass wavenumber filter. The most recent developed application by the same authors it is the CFAT that allows to obtain good results with a coarse measurement scheme and is also used in order to the material characterization [8].
Another interesting approach is the force identification in the wavenumber domain [9, 10]; as above, this technique is based on the knowledge of the analytical model in the frequency domain of the structure. The force is obtained starting from the measured response through the transformation from space to wavenumber domain made by Fourier

sine transform, then the force in space domain is computed by using the inverse Fourier transform or the Ibrahim Time Domain(ITD) method [11].

1.1 The ill-conditioning in the force identification problem

Let us consider a generic system excited by a force as in figure 1.1. The relationship input-output can be written in frequency domain as follow:

$$\mathbf{x}(\omega) = \mathbf{H}(\omega)f(\omega) \tag{1.1}$$

where in general $\mathbf{f}(\omega)$ is a (n $\times$ 1) vector of unknown forces, $\mathbf{x}(\omega)$ is a (m $\times$ 1) vector of measured responses and $\mathbf{H}(\omega)$ is the (m $\times$ n) Frequency Response Function (FRF) matrix.
The FRF matrix is the transfer function depending on the system properties; if an input (i.e. force, pressure,...) is known, equation (1.1) gives the system output (i.e. displacement, velocity, acceleration)
The force identification is correlated to the inverse problem. Starting from equation (1.1) it can be defined by the following relation:

$$\mathbf{f}(\omega) = \mathbf{H}^{+}(\omega)\mathbf{x}(\omega). \tag{1.2}$$

where the matrix $\mathbf{H}^{+}$ is the pseudo inverse of the matrix $\mathbf{H}$, defined as follow:

$$\mathbf{H}^{+} = [\mathbf{H}^{H}\mathbf{H}]^{-1}\mathbf{H}^{H}. \tag{1.3}$$

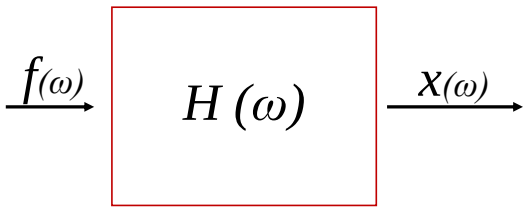

Figure 1.1: Input-Output model

The ill-conditioning of the problem, is the main reason for which the identification of actual loads can not be efficiently performed by the inversion of $\mathbf{H}$. A problem is ill-conditioned when a small error in the data generates large perturbations in the solution.

Considering the problem of equation (1.2), where the vector of the data $\bar{\mathbf{x}}$ is affected by the error ε, the solution of the inverse problem in absence of ill-conditioning is:

$$\mathbf{H}^{+}(\omega)\bar{\mathbf{x}}(\omega) = \mathbf{f}(\omega) + \tilde{\varepsilon} \qquad where \qquad \tilde{\varepsilon} \approx \varepsilon \tag{1.4}$$

If the FRF is ill-conditioned the solution becomes:

$$\mathbf{H}^{+}(\omega)\bar{\mathbf{x}}(\omega) = \mathbf{f}(\omega) + \tilde{\tilde{\varepsilon}} \qquad where \qquad \tilde{\tilde{\varepsilon}} \gg \varepsilon \tag{1.5}$$

For this reason it is necessary to reduce the ill-conditioning of the FRF matrix in order to obtain an acceptable result.

1.1.1 Regularization techniques

In this section, some classical regularisation techniques, which allow to improve the system conditioning, are presented. These techniques work directly on the solution written by the Singular Values Decomposition (SVD). The singular values of the matrix are deleted or filtered out in order to decreases its ill-conditioning. This mathematical procedure reduces the information included in the original matrix, but it does not allow to understand which physical information are excluded.
In this section three of these techniques are presented. In the next chapter they are employed for some tests and the obtained results are compared to verify the ability of each technique to improve results of the identification process.
Let us understand how the regularisation techniques are effective to reduce the consequences of the ill-conditioning in force identification problems.
The regularisation techniques used in this thesis are based on the decomposition of the matrix $\mathbf{H}$ by SVD [12]. A generic matrix $\mathbf{H}$ of dimension (m $\times$ n) can be decomposed on the product of three matrices, as follows [13]:

$$\mathbf{H} = \mathbf{U}\boldsymbol{\Sigma}\mathbf{V}^{H} = \sum_{i=1}^{n} \mathbf{u}_i \sigma_i \mathbf{v}_i^{H} \tag{1.6}$$

where $\mathbf{U}$ and $\mathbf{V}$ are matrices of orthonormal vectors $\mathbf{u_i}$ and $\mathbf{v_i}$, $\mathbf{U}$ is a (m $\times$ m) matrix in which the column are the left eigenvectors of $\mathbf{H}\mathbf{H}^{H}$, $\mathbf{V}$ is a (n $\times$ n) matrix of right eigenvectors of $\mathbf{H}^{H}\mathbf{H}$ for each row. Σ is the diagonal matrix of singular values such that [14]:

$$\sigma_1 \geq \sigma_2 \geq ... \geq \sigma_r \geq ... \geq \sigma_n \geq 0 \tag{1.7}$$

where σ_r is the smaller non-zero singular value; when $r \neq n$ it happens that $\sigma_{r+1}, ..., \sigma_n = 0$, then the matrix $\mathbf{H}$ is singular. The non-zero singular values are the square root of non-zero eigenvalues of both $\mathbf{H}\mathbf{H}^{H}$ and $\mathbf{H}^{H}\mathbf{H}$. Using SVD, the equation (1.2) is written:

$$\mathbf{f} = \sum_{i=1}^{n} \frac{\mathbf{u}_i^{H}\mathbf{x}\mathbf{v}_i}{\sigma_i} \tag{1.8}$$

The measure of the ill-conditioning is given by the condition number (CN) that is defined as follows:

$$CN = ||H||||H^{+}|| \tag{1.9}$$

In terms of SVD the values assumed by the 2-norm are the largest eigenvalues of $\mathbf{H}^H\mathbf{H}$ [13]; then, by using SVD the terms of the previous equation assume the values:

$$||\mathbf{H}|| = \sigma_1 \tag{1.10}$$

$$||\mathbf{H}^{+}|| = \frac{1}{\sigma_r} \tag{1.11}$$

The largest terms of $||\mathbf{H}^{+}||$ is the reciprocal of $1\backslash\sigma_n$, where σ_n corresponds to the minimum non zero singular values of the rectangular matrix $\mathbf{H}$. Hence the condition number can be expressed as follows:

$$CN = \frac{\sigma_1}{\sigma_r}. \tag{1.12}$$

The force identification is obtained by using the following three regularisation technique:

- Damped Singular Values Decomposition (DSVD)
- Truncated Singular Values Decomposition (TSVD)
- Tikhonov regularisation

Considering equation (1.8), it is clear that the presence of small singular values perturbs highly the solution of the problem; in order to limit this problem the use of regularisation filters is required. All these techniques, starting from equation (1.8), introduce a filter factor ξ that depends on a regularisation parameter λ. Equation (1.8) can be rewritten:

$$\mathbf{f} = \sum_{i=1}^{n} \xi_i(\lambda) \frac{\mathbf{u}_i^H \mathbf{x} \mathbf{v}_i}{\sigma_i} \tag{1.13}$$

There are a lot of different criteria aimed to select the correct value of the regularisation parameter λ. Among these methods three are selected to perform the numerical force identification:

- L-curve
- Quasi Optimality
- Generalized Cross Validation

Damped Singular Values Decomposition

The DSVD was introduced by Ekstrom [15], and the filter factor is defined as [14]:

$$\xi_i = \frac{\sigma_i}{\sigma_i + \lambda}. \tag{1.14}$$

The regularised solution becomes:

$$\mathbf{f} = \sum_{i=1}^{n} \frac{\sigma_i}{\sigma_i + \lambda} \frac{\mathbf{u}_i^H \mathbf{x} \mathbf{v}_i}{\sigma_i}. \tag{1.15}$$

Tikhonov

In Tikhonov regularisation [16] the reduction of ill-conditioning is obtained through the minimisation of the following functional:

$$R_\lambda = \|\mathbf{Hf} - \mathbf{x}\|_2^2 + \lambda^2 \|\mathbf{I}\ \mathbf{f}\|_2^2. \tag{1.16}$$

The first term is the residual and the second term is the value of the solution. In this case the filter ξ_i has the following expression:

$$\xi_i = \frac{\sigma_i^2}{\sigma_i^2 + \lambda_i^2} \tag{1.17}$$

and the regularised solution becomes:

$$\mathbf{f} = \sum_{i=1}^{n} \frac{\sigma_i^2}{\sigma_i^2 + \lambda^2} \frac{\mathbf{u}_i^H \mathbf{x} \mathbf{v}_i}{\sigma_i}. \tag{1.18}$$

It is clear that, the DSVD filter is smoother than the Tikhonov filter.

Truncated Singular Values Decomposition

TSVD [17] reduces the ill-conditioning of the matrix $\mathbf{H}$ by substituting the not full rank matrix $\mathbf{H}$ with a new full rank matrix [18] obtained by truncating the sum of equation (1.8) to a value $p < n$. Therefore, the sum in equation (1.8) becomes:

$$\mathbf{f} = \sum_{i=1}^{p} \frac{\mathbf{u}_i^H \mathbf{x} \mathbf{v}_i}{\sigma_i} \tag{1.19}$$

where $p < n$ is the truncation parameter. If the matrix $\mathbf{H}$ is singular, p can be equal to r, the minimum non-zero singular value. If $\mathbf{H}$ is ill-conditioned, p can be calculated in order to reduce the condition number of the matrix. In this case the filter factors assume only values 0 or 1.
In figure 1.2 the trend of the three regularisation parameters for a σ_i are shown.

L-curve

The choice of the optimal value of the filter is the critical point of the regularisation techniques. It is necessary to find the best compromise between the removal of components that amplify the errors of the data in the solution and the lost of information of the solution. The filter has to act without deleting those components that are necessary to have a meaningful solution: it is a critical point.
The L-curve allows to choose a parameter with a good compromise between the regularised solution and the residual norm. This point is shown in a log-log scale graph (figure 1.3) [14].
In the left of the graph the filtering is smaller and the solution is dominated by perturbation errors. In the right part the filtering increases and the solution is affected by

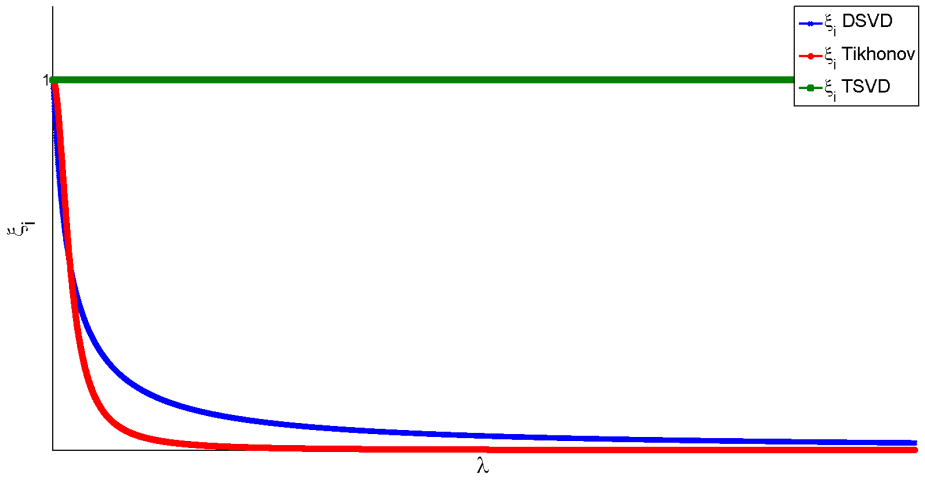

Figure 1.2: Comparison between the filters factor of different regularisation techniques

filtering errors. So in the vertical part of the curve the solution is sensitive to the change of regularisation parameter and in the horizontal one the residual is very sensitive to the regularisation parameter. The compromise between these two errors is the point in correspondence of the L-curve corner that corresponds to the values of the optimal regularisation parameter.

Quasi Optimality

The regularisation parameter can be found by the definition of the quasi optimality principle through the solution of following minimum problem [19]:

$$arg\min |f_{reg} - f_{actual}| \tag{1.20}$$

The values of actual f, f_{actual}, are unknown, therefore the parameter is chosen as the minimum value of the first term of the Taylor expansion of equation (1.20)

$$\mu(\lambda_{opt}) = \inf ||\lambda \frac{df_\lambda}{d\lambda}||_2 \tag{1.21}$$

Generalized Cross Validation

The Generalized Cross Validation starts from the measured data to choose the regularisation parameter [20, 21]. The solution f_λ^i is computed by eliminating each time one experimental observation, and the choice of the regularisation parameter should be independent respect an orthogonal transformation of f_λ^i [14]. Therefore λ is the value that

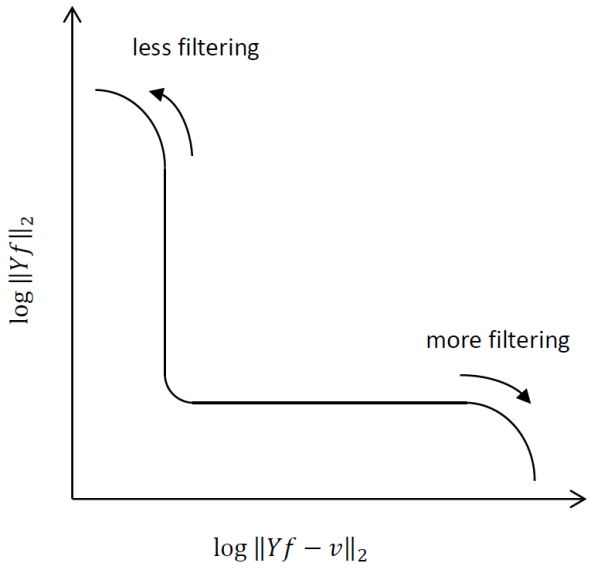

Figure 1.3: L-curve.

minimizes the sum of the errors:

$$C(\lambda) = \frac{1}{m} \sum_{i=1, i \neq \lambda}^{m} w_i (\mathbf{H}(\lambda) f_\lambda^i - x_i)^2 \tag{1.22}$$

where m is the number of measurement points. From equation (1.22) the functional $G(\lambda)$ is derived:

$$G(\lambda) = \frac{\frac{1}{m} ||(I - \mathbf{B}(\lambda))x||_2^2}{[\frac{1}{m} Tr(\mathbf{I} - \mathbf{B}(\lambda))]^2} \tag{1.23}$$

where $B(\lambda)$ is equal to:

$$B(\lambda) = \mathbf{H}_t (\mathbf{H}_t^H \mathbf{H}_t + \lambda \mathbf{I})^{-1} \mathbf{H}_t^H.$$

CHAPTER
TWO

IDENTIFICATION OF DETERMINISTIC FORCES AT LOW-MEDIUM FREQUENCIES

This chapter is focused on the study of the relationship between the ill-conditioning of the FRF matrix and the degrees of freedom taken into account for a low frequency problem when the solution of the investigated problem is performed by modal analysis. In operative condition, one of the main issue is the selection of the optimal measurement points configuration that allows to perform load identification. The relationship between this choice and the goodness of the results obtained from the identification, is investigated through a numerical procedure. This procedure, in which a numerical force identification is carried out by using different regularisation techniques based on Singular Values Decomposition (SVD), is aimed to identify the optimal experimental setup [22] to perform the identification of external forces. This is done by using both numerical FRF, calculated by the modal parameters obtained by a FEM of the structure, and an experimental FRF. Results are compared and discussed.
In the second part of the chapter the effect of a convenient reduction of the degrees of freedom, on the solution of this problem, is investigated.

2.1 Identification of the best experimental setup

The considered structure is made of three steel plates, 1.5 mm thick, coupled as shown in figure 2.1 with free boundary conditions. The dimensions of the structure are reported in table 2.1.
A number of points $N_t = 24$, located as shown in figure 2.1, are considered on the structure. The coordinates of the selected points are displayed in table 2.2.
Eigenvalues and eigenvectors of the structure are calculated by a Finite Element Model in the frequency range 1-2000 Hz. The numerical FRF is computed using the following

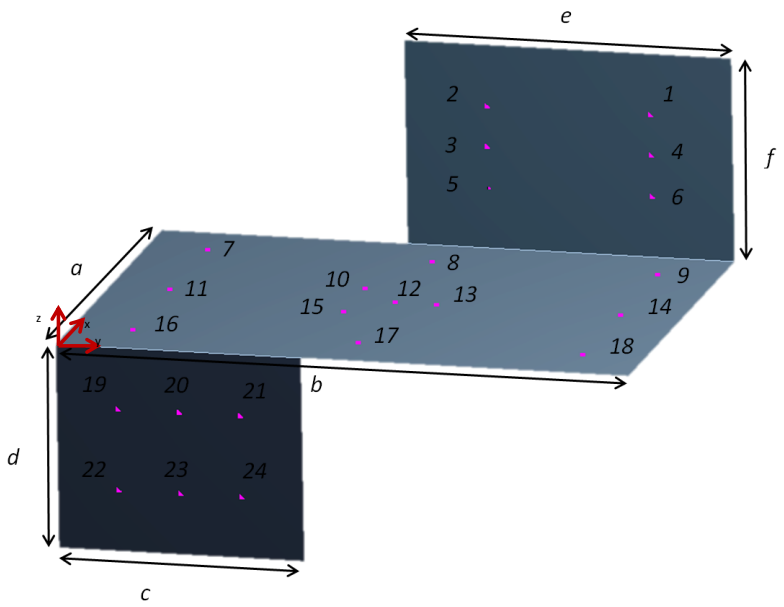

Figure 2.1: Test structure

Table 2.1: Structure dimensions

a[mm]	b[mm]	c[mm]	d[mm]	e[mm]	f[mm]
500	700	300	250	400	250

Table 2.2: Coordinates of the selected points

Node	***X [mm]***	***Y [mm]***	***Z [mm]***	***Node***	***X [mm]***	***Y [mm]***	***Z [mm]***
1	500	100	175	**13**	250	300	0
2	500	300	175	**14**	250	75	0
3	500	300	125	**15**	200	400	0
4	500	100	125	**16**	75	625	0
5	500	300	75	**17**	75	350	0
6	500	100	75	**18**	75	75	0
7	425	625	0	**19**	0	625	-75
8	425	350	0	**20**	0	550	-75
9	425	75	0	**21**	0	475	-75
10	300	400	0	**22**	0	625	-175
11	250	625	0	**23**	0	550	-175
12	250	350	0	**24**	0	475	-175

equation:

$$Y_{i,j}(\omega) = j\omega \sum_{q=1}^{n} \frac{\phi_q(x_i)\phi_q(x_j)}{M_q(\omega_q^2 - \omega^2 + j\omega(\alpha + \beta\omega_q^2)}. \tag{2.1}$$

where $\phi_q(x_i)$ and ω_q are respectively eigenvectors and eigenvalues previously obtained and α and β are, respectively, the mass-proportional and the stiffness-proportional damping coefficients.
The first step of this procedure is the computation of the numerical response of the structure as shown in figure 2.2. The velocity of each point is calculated by:

$$\overline{\mathbf{v}}(\omega) = \mathbf{Y}(\omega)\mathbf{f}(\omega) + \varepsilon(\omega) \tag{2.2}$$

where $\mathbf{f}$ is the force applied to the structure, $\varepsilon(\omega)$ is a noise proportional to the rms velocity and $\overline{\mathbf{v}}(\omega)$ indicates the velocity affected by noise and $\mathbf{Y}(\omega)$ is the mobility matrix.

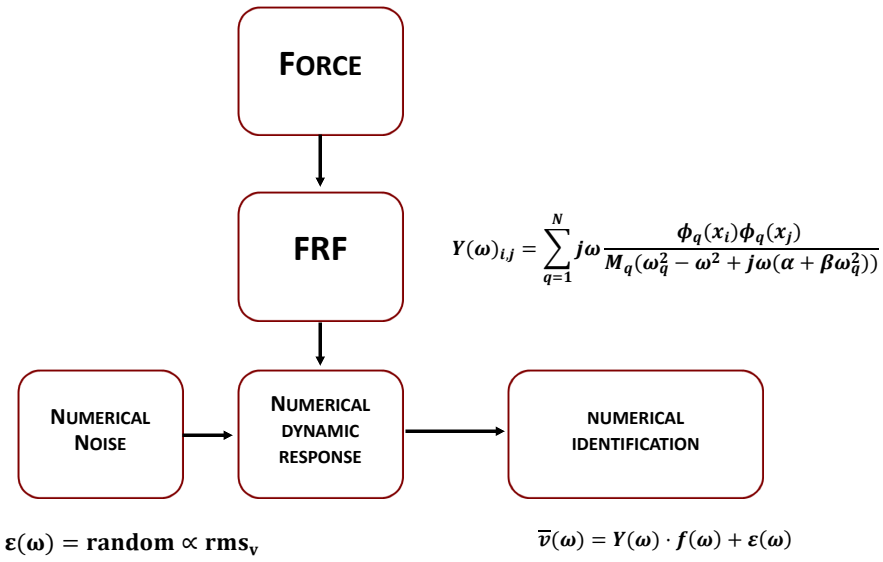

Figure 2.2: Diagram of the numerical identification procedure

The second step is the choice of the points number of the experimental setup: this is usually bound by the operative condition. In this application, the number of measurement points on the structure is set to $N_p = 12$. Therefore a large number of configurations are picked among the possible combinations of equation (2.3):

$$C_{N_t,N_p} = \binom{N_t}{N_p} \tag{2.3}$$

A deterministic load is applied to each point of the considered configurations. The reconstruction of the force field is performed using the three regularisation techniques presented in section 1.1. This analysis is carried out between 1 and 2000 Hz by averaging the results on constant bandwidths of 100 Hz.
As expected, the procedure generates a large number of results. To compare these results two indices are used that take into account the positioning error [23].
The first index I_{NORM} is the percentage error given by the norm of the difference between the magnitude of the actual force and the identified one, normalized on the first one:

$$I_{NORM} = \left[1 - \frac{\| |\mathbf{f}_{actual}| - |\mathbf{f}_{identified}| \|}{\|\mathbf{f}_{actual}\|}\right] \cdot 100 \tag{2.4}$$

The second index I_{AVG} is the percentage mean error computed by the relative difference between the amplitude of the identified force in the correct position and the mean of the spurious components of the forces on the whole set of points.

$$I_{AVG} = \left| \frac{|f_{identified}| - |\sum_{i=1, i\neq dp}^{n} \frac{f_{identified_i}}{n-1}|}{|f_{actual}|} \right| \cdot 100 \tag{2.5}$$

2.1.1 Numerical results

The numerical identification is performed by exciting each point of the considered configuration, by computing the response and by identifying the applied load taking advantage of the regularisation techniques. The considered configurations are shown in table 2.3. The values of the indices for all the considered configurations and for each frequency band, by considering each point of each configuration as drive point, are calculated.
The data interpretation is carried out by the indices averaged in frequency and in the drive points set, figure 2.3. For each configuration the values obtained by the three regularisation techniques and the different λ criteria are shown.
In table 2.4 the values of I_{AVG} are shown. Since the criterion to select the best configuration is to choose the highest I_{AVG} index values, configuration 50 is the best configuration (see table 2.4).
Note that, using the DSVD regularisation technique all the three criteria have the same I_{AVG} value, whilst Tikhonov with GCV and L-curve gives higher values of I_{AVG} than Tikhonov with Quasi Optimality. Using TSVD only GCV criterion gives high value of I_{AVG}, while the Quasi Optimality criterion in TSVD does not give good result.
Figure 2.4 shows the I_{AVG} values versus frequency of configuration 50. They change much for each frequency band and only averaging these values (figure 2.5) clear results can be obtained.

Table 2.3: Configuration of the points selected for the numerical test

Conf 1	1	2	4	8	10	13	15	16	18	20	21	22
Conf 2	1	2	6	8	10	12	14	15	18	20	21	22
Conf 3	1	2	6	7	8	12	14	15	18	19	20	24
Conf 4	1	2	6	7	8	12	14	15	18	19	22	24
Conf 5	1	2	5	7	8	9	11	13	14	19	20	24
Conf 6	1	2	5	7	8	9	10	14	15	19	20	24
Conf 7	1	2	6	8	10	12	14	15	18	19	22	24
Conf 8	1	2	6	8	10	11	12	15	18	20	21	22
Conf 9	1	2	6	7	8	12	14	15	18	19	22	23
Conf 10	1	2	3	7	11	14	15	17	18	21	23	24
Conf 11	1	2	6	7	8	10	12	15	18	20	21	22
Conf 12	1	2	5	7	10	12	13	15	16	20	21	22
Conf 13	1	2	6	7	8	12	14	15	18	20	21	22
Conf 14	1	2	6	8	11	12	14	15	18	20	21	22
Conf 15	1	2	4	7	9	10	11	12	15	20	21	22
Conf 16	1	2	6	9	11	12	14	15	17	19	20	23
Conf 17	1	2	6	8	10	12	14	15	18	19	21	22
Conf 18	1	2	3	7	11	12	15	17	18	21	22	24
Conf 19	1	2	4	8	11	12	14	15	18	20	21	22
Conf 20	1	2	4	7	8	11	12	14	18	19	22	24
Conf 21	2	5	6	8	11	14	15	17	18	21	22	23
Conf 22	2	4	5	7	10	12	13	14	17	21	22	23
Conf 23	2	5	6	8	9	11	12	16	17	19	21	23
Conf 24	1	3	5	7	9	11	12	15	16	20	21	22
Conf 25	3	4	5	8	10	12	15	16	18	21	22	24
Conf 26	2	3	4	8	9	11	13	15	17	20	21	22
Conf 27	1	2	4	7	8	12	13	14	15	19	20	23
Conf 28	3	4	5	9	12	13	15	17	18	19	20	24
Conf 29	1	5	6	8	9	14	16	17	18	19	21	22
Conf 30	1	2	6	8	13	14	15	16	17	20	22	24
Conf 31	1	4	6	8	9	10	11	12	14	22	23	24
Conf 32	4	5	6	7	9	10	13	16	18	21	22	23
Conf 33	1	4	6	7	9	14	15	16	17	21	22	23
Conf 34	4	5	6	7	10	11	13	16	18	21	22	23
Conf 35	1	3	6	7	9	13	15	16	17	21	22	23
Conf 36	4	5	6	8	12	13	15	16	17	21	22	23
Conf 37	3	4	6	9	13	14	15	16	18	21	22	23
Conf 38	1	4	5	7	8	9	15	16	17	21	22	23
Conf 39	3	4	6	7	8	9	15	16	17	21	22	23
Conf 40	4	5	6	7	8	10	16	17	18	21	22	23
Conf 41	4	5	6	7	14	15	16	17	18	21	22	23
Conf 42	1	4	6	7	14	15	16	17	18	21	22	23
Conf 43	3	4	6	7	8	13	15	16	17	21	22	23
Conf 44	3	5	6	7	9	13	15	16	17	21	22	23
Conf 45	1	4	6	9	12	14	16	17	18	22	23	24
Conf 46	3	4	6	7	14	15	16	17	18	21	22	23
Conf 47	4	5	6	7	10	13	14	16	18	21	22	23
Conf 48	4	5	6	7	8	13	15	16	17	21	22	23
Conf 49	3	4	6	7	9	13	14	16	18	21	22	23
Conf 50	4	5	6	7	9	13	14	16	18	21	22	23

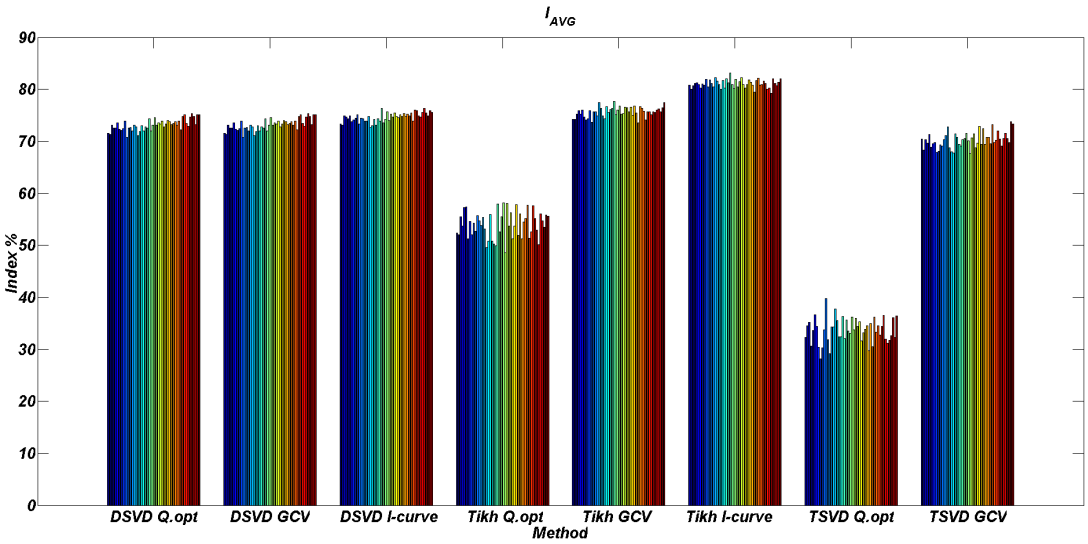

(a) Comparison between I_{AVG}: frequency and drive points average.

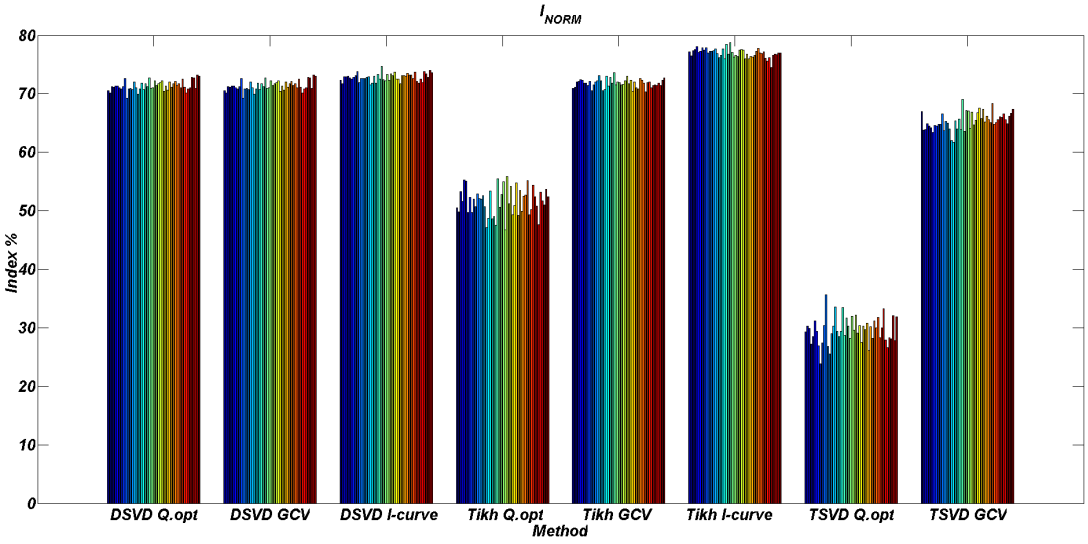

(b) Comparison between I_{NORM}: frequency and drive points average.

Figure 2.3: Comparison between indices obtained by numerical simulation with different configurations, indices averaged over frequency and drive points.

Table 2.4: I_{AVG} obtained by numerical simulation with different configurations, indices averaged over frequency and drive points

	DSVD			***Tikhonov***			***TSVD***	
	Q. Opt	***GCV***	***L-Curve***	***Q. Opt***	***GCV***	***L-Curve***	***Q. Opt***	***GCV***
Conf 1	72	72	73	52	74	81	32	70
Conf 2	71	71	73	52	74	80	35	68
Conf 3	73	73	75	56	75	81	35	70
Conf 4	73	73	75	54	76	81	31	70
Conf 5	73	73	74	57	75	81	34	71
Conf 6	74	74	75	57	76	81	37	69
Conf 7	72	72	74	51	75	80	34	70
Conf 8	72	72	74	55	74	81	30	70
Conf 9	72	72	74	52	74	81	28	68
Conf 10	74	74	75	54	76	82	30	68
Conf 11	71	71	73	53	74	80	34	69
Conf 12	73	73	74	56	76	82	40	69
Conf 13	73	73	74	55	76	81	32	70
Conf 14	72	72	74	54	75	80	29	71
Conf 15	73	73	74	55	77	82	34	73
Conf 16	73	73	75	53	76	82	34	69
Conf 17	71	71	73	50	75	81	38	68
Conf 18	72	72	73	51	74	80	36	68
Conf 19	73	73	74	56	77	82	32	71
Conf 20	72	72	73	51	76	80	32	71
Conf 21	73	73	74	50	76	82	36	69
Conf 22	73	73	74	50	76	81	32	69
Conf 23	74	74	76	58	78	83	36	70
Conf 24	72	72	74	53	75	81	34	70
Conf 25	73	73	74	55	76	80	33	72
Conf 26	75	75	76	58	77	82	36	70
Conf 27	73	73	74	49	75	80	34	68
Conf 28	73	73	75	58	75	82	36	71
Conf 29	73	73	75	54	77	82	34	71
Conf 30	74	74	75	56	76	81	35	69
Conf 31	73	73	75	51	76	80	32	70
Conf 32	73	73	75	54	77	81	33	73
Conf 33	74	74	75	58	75	82	34	69
Conf 34	74	74	75	52	77	81	35	72
Conf 35	73	73	75	56	75	81	30	69
Conf 36	73	73	75	51	74	80	35	71
Conf 37	74	74	75	54	77	82	31	71
Conf 38	73	73	75	55	76	82	36	70
Conf 39	74	74	75	58	76	81	33	73
Conf 40	72	72	74	51	74	81	34	70
Conf 41	75	75	76	53	76	82	33	70
Conf 42	75	75	76	58	76	81	34	72
Conf 43	73	73	75	55	75	80	36	70
Conf 44	73	73	75	53	76	80	32	69
Conf 45	75	75	76	50	76	79	31	71
Conf 46	75	75	76	56	76	82	32	72
Conf 47	75	75	75	55	76	81	33	71
Conf 48	73	73	75	53	76	81	36	70
Conf 49	75	75	76	56	76	81	32	74
Conf 50	75	75	76	56	77	82	36	73

Table 2.5: I_{NORM} obtained by numerical simulation with different configurations, indices averaged over frequency and drive points

	DSVD			***Tikhonov***			***TSVD***	
	Q. Opt	***GCV***	***L-Curve***	***Q. Opt***	***GCV***	***L-Curve***	***Q. Opt***	***GCV***
Conf 1	71	71	72	51	71	77	29	67
Conf 2	70	70	72	50	71	77	30	64
Conf 3	71	71	73	53	72	77	30	64
Conf 4	71	71	73	52	72	78	27	65
Conf 5	71	71	73	55	72	78	28	65
Conf 6	71	71	73	55	72	77	31	64
Conf 7	71	71	72	50	72	77	29	63
Conf 8	71	71	73	52	72	78	27	65
Conf 9	71	71	73	50	71	78	24	65
Conf 10	73	73	74	52	72	78	27	65
Conf 11	69	69	72	51	71	77	30	65
Conf 12	71	71	73	53	72	77	36	67
Conf 13	71	71	73	52	72	77	27	64
Conf 14	71	71	73	52	72	77	25	65
Conf 15	72	72	73	53	73	78	29	65
Conf 16	71	71	73	51	72	77	30	64
Conf 17	70	70	71	47	71	76	34	62
Conf 18	71	71	72	49	71	77	29	62
Conf 19	72	72	73	53	73	78	28	65
Conf 20	71	71	72	49	71	76	29	64
Conf 21	72	72	73	49	73	79	33	66
Conf 22	71	71	72	48	72	77	29	64
Conf 23	73	73	75	55	74	79	32	69
Conf 24	71	71	72	51	71	77	30	64
Conf 25	71	71	72	53	72	76	28	67
Conf 26	72	72	73	55	72	77	32	67
Conf 27	71	71	72	47	72	76	30	64
Conf 28	72	72	73	56	72	77	32	67
Conf 29	72	72	73	51	72	78	29	65
Conf 30	72	72	74	54	73	77	30	65
Conf 31	70	70	72	49	72	76	27	67
Conf 32	71	71	73	51	72	77	30	68
Conf 33	71	71	72	55	70	76	30	66
Conf 34	72	72	73	49	72	76	31	67
Conf 35	71	71	73	53	71	76	26	65
Conf 36	72	72	73	50	71	77	30	66
Conf 37	72	72	74	52	73	77	28	66
Conf 38	71	71	73	53	72	78	31	65
Conf 39	72	72	73	55	72	77	30	68
Conf 40	71	71	73	49	70	77	32	65
Conf 41	73	73	74	50	72	77	28	65
Conf 42	71	71	72	54	72	76	30	66
Conf 43	70	70	72	52	71	76	33	66
Conf 44	71	71	73	51	71	76	28	66
Conf 45	71	71	72	48	72	74	27	67
Conf 46	73	73	74	53	71	77	28	66
Conf 47	73	73	73	52	72	77	28	65
Conf 48	71	71	73	51	71	77	32	66
Conf 49	73	73	74	54	72	77	28	67
Conf 50	73	73	74	52	73	77	32	67

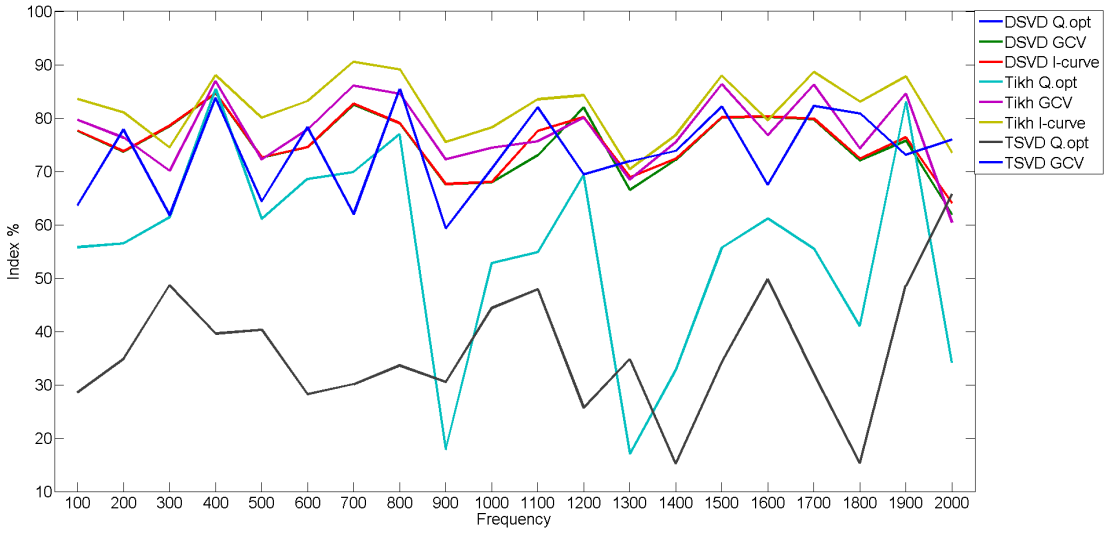

Figure 2.4: Comparison between I_{AVG} obtained by numerical simulation for the configuration 50, indices averaged over frequency and drive points

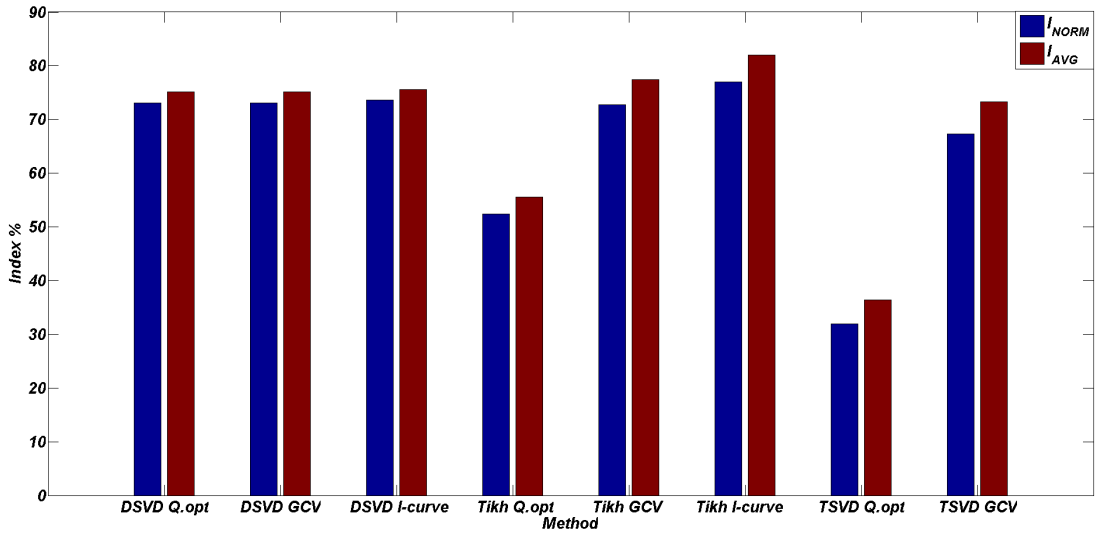

Figure 2.5: Comparison between I_{AVG}(red) and I_{NORM} (blue) obtained by numerical simulation for the configuration 50, indices averaged over frequency and drive points

2.1.2 Results by experimental FRF

In order to validate the proposed procedure, the indices are computed using experimental FRF. The test bed corresponds obviously to the numerical model. To simulate the free

boundary conditions, the structure lays on a soft support as shown in figure 2.6. The experimental FRFs are computed by Single Input Multi Output(SIMO) technique in correspondence of 13 points, chosen among the 24 points of the numerical test (see table 2.6). The system is excited with a white random noise obtained by a hammer multi impulse in correspondence of each measurement point. The acceleration is acquired using a set of accelerometers connected with a 16 channel acquisition system for 20 seconds at 5000 Hz sample frequency. The measurement chain is drawn in figure 2.7.

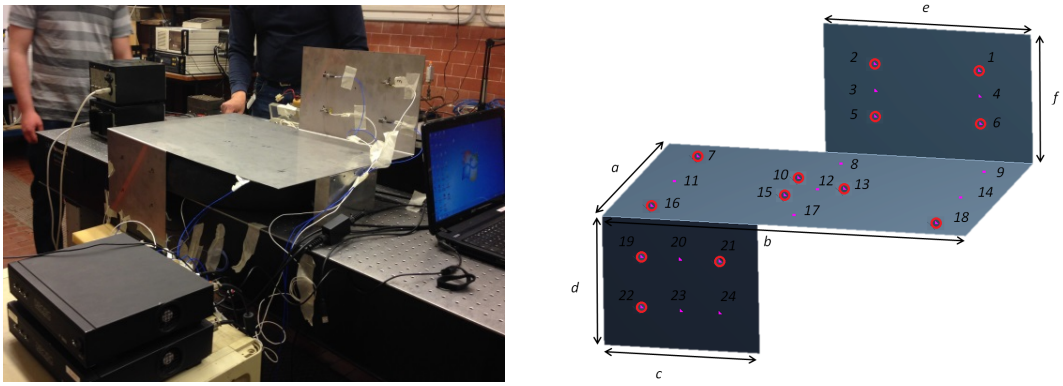

Figure 2.6: Experimental setup

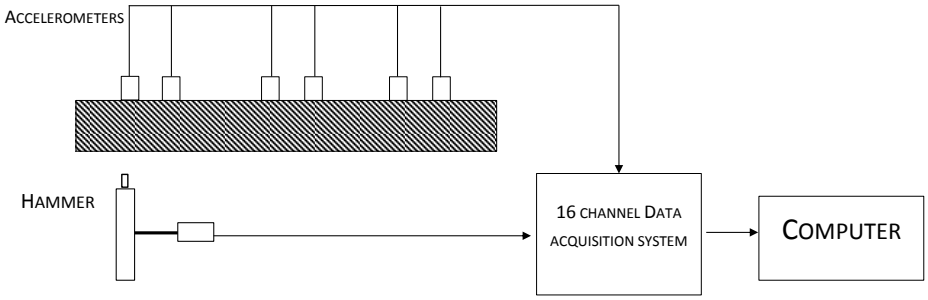

Figure 2.7: Measurement chain

The experimental FRFs are computed up to 2000 Hz. Figure 2.8 shows the comparison between the numerical and the experimental FRFs for one of the chosen points. The correspondence is good up to 1000 Hz: consider that the model is not updated.
In the experimental validation the number N_t of points is 13 (table 2.6) and the number

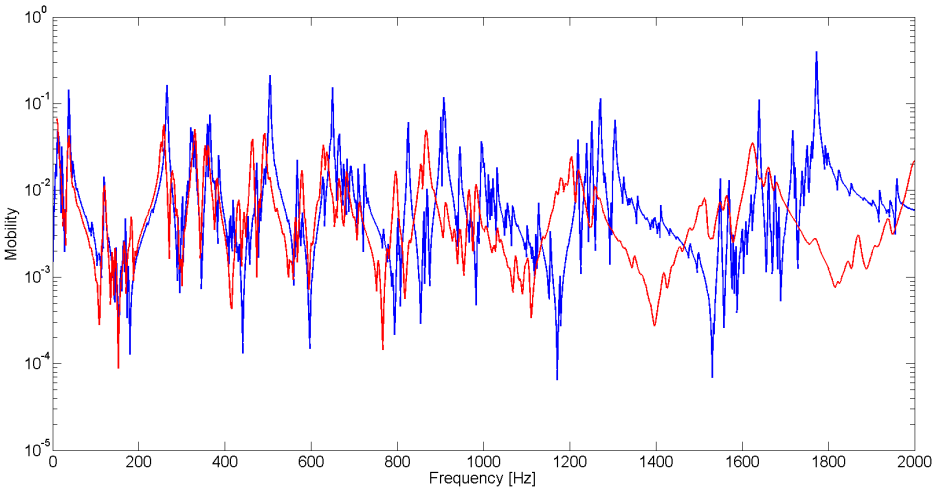

Figure 2.8: Comparison between numerical frequency response function(blue) and experimental one (red).

of points for each configuration is $N_c = 8$. Also in this case, as in the previous section, the input is a numerical signal and the output is calculated by experimental FRF. The computed velocities are polluted by an error proportional to the rms velocity of 10 %. Figure 2.9 shows the comparison between the values of the two indices (averaged over the frequency and the drive points) for all considered configurations. The best configuration is the configuration with the highest indices values. As shown in table 2.8 and 2.9 the configuration 32 gives the highest indices values, so it can be chosen as experimental setup in order to perform loads identification.

Table 2.6: Selected points in experimental setup

1	X	7	X	13	X	19	X
2	X	8		14		20	
3		9		15	X	21	X
4		10	X	16	X	22	X
5	X	11		17		23	
6	X	12		18	X	24	

Figure 2.10 shows the comparison between the average over all frequencies and over all drive points, N_p, of the numerical and experimental indices. The amplitude of the indices obtained from numerical FRF are lower than those obtained from the experimental one, but the trend is strictly consistent for all considered methods. This result is due to the effect of the damping on the experimental FRF, indeed in the numerical model a proportional damping that takes into account only the material dissipation is used; this imply that the experimental FRF is smoother than the numerical one (see figure 2.8).

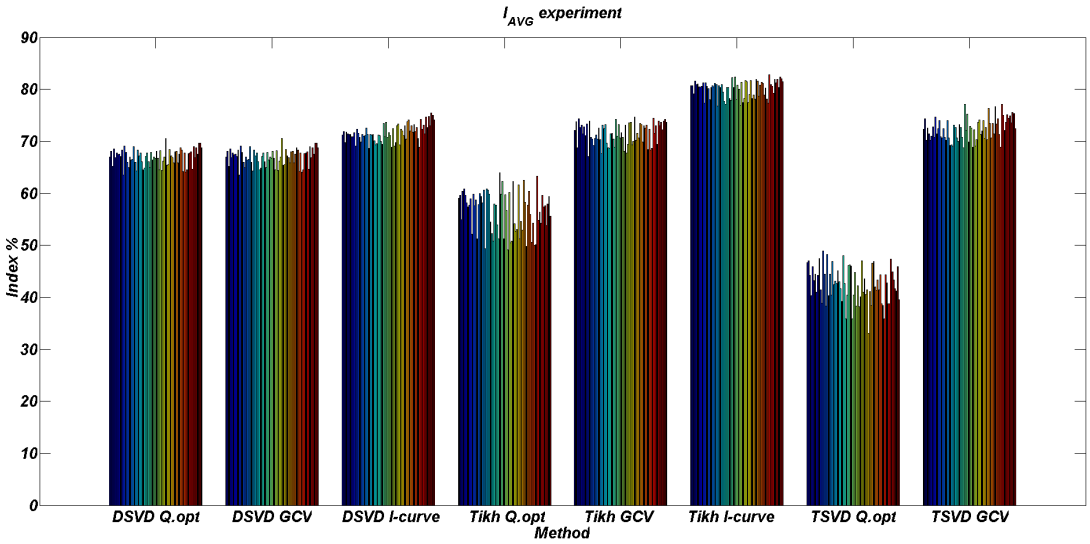

(a) Comparison between I_{AVG}: frequency and drive points average.

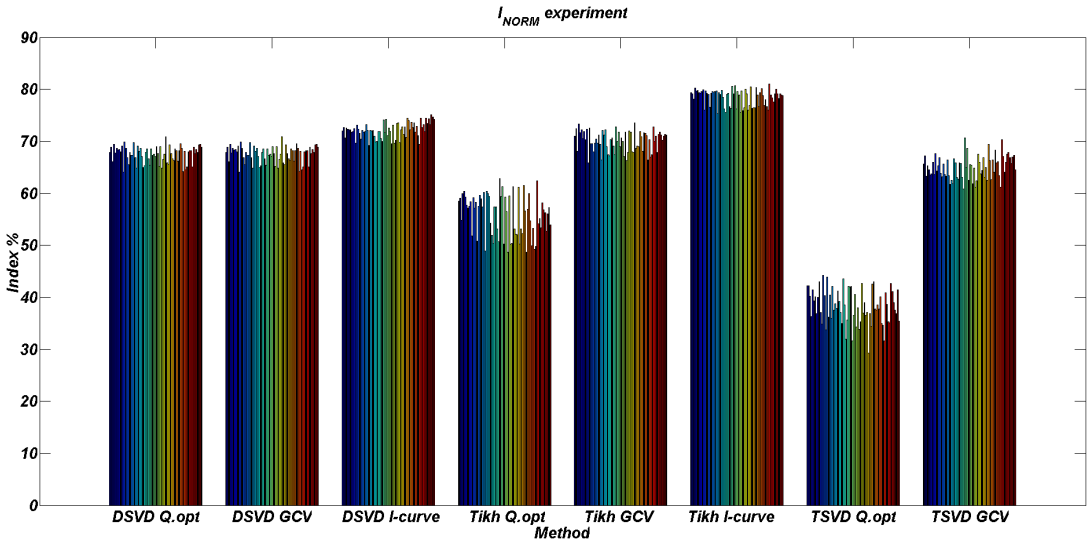

(b) Comparison between I_{NORM}: frequency and drive points average.

Figure 2.9: Comparison between indices obtained by experimental FRF with different configurations, indices averaged over frequency and drive points.

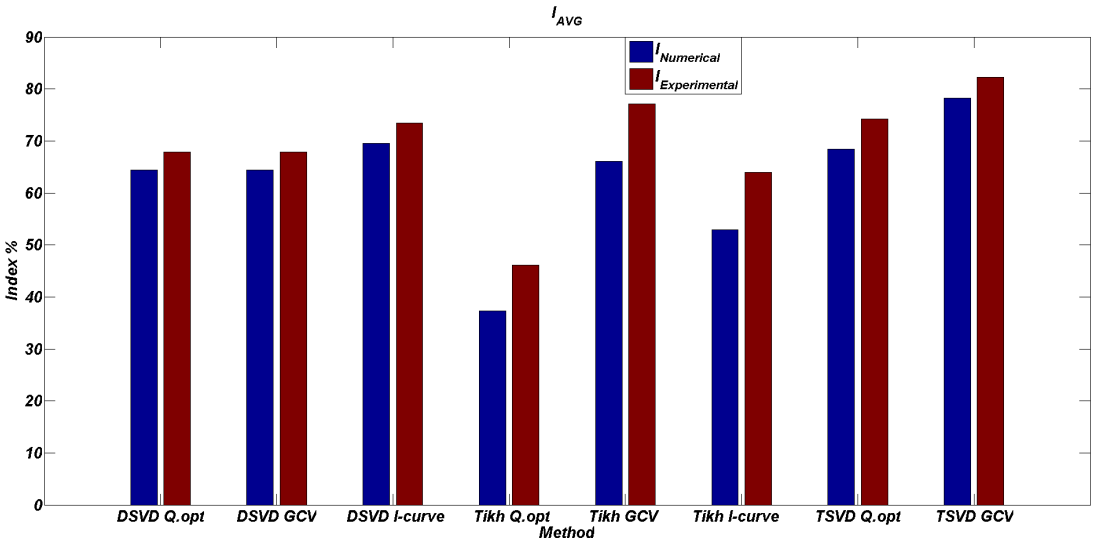

(a) Comparison between I_{AVG} regularised: frequency and drive points average .

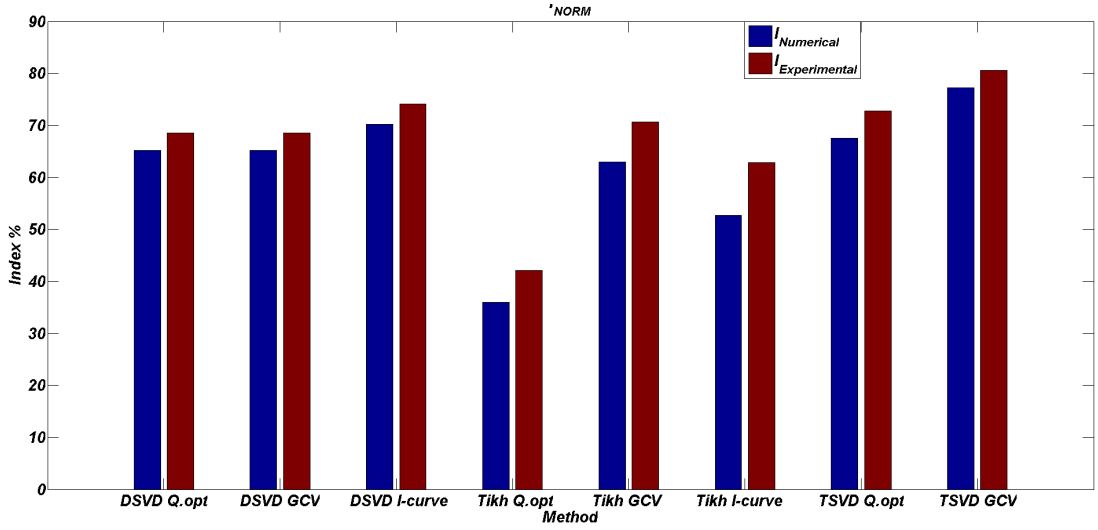

(b) Comparison between I_{NORM} regularised: frequency and drive points average .

Figure 2.10: Comparison between indices obtained for the best configuration (Conf. 32) by numerical FRF (blue) and experimental FRF (red)

The good matching between the results of the numerical and the experimental tests validates the proposed procedure to evaluate the best experimental setup to perform external load identification. The results show also that the procedure works even if the numerical model is not updated.

Table 2.7: Configuration of the points selected for the experimental test

Conf 1	2	6	7	10	13	15	21	22	***Conf 36***	1	6	7	15	16	18	21	22
Conf 2	2	6	10	13	15	16	21	22	***Conf 37***	1	6	7	10	16	18	21	22
Conf 3	1	2	13	15	16	18	21	22	***Conf 38***	2	6	13	15	16	18	19	22
Conf 4	2	6	10	13	16	18	21	22	***Conf 39***	1	2	7	13	15	16	21	22
Conf 5	2	6	7	10	13	16	21	22	***Conf 40***	1	2	10	15	16	18	19	22
Conf 6	2	6	10	15	16	18	21	22	***Conf 41***	1	2	10	13	15	16	19	22
Conf 7	1	6	7	10	13	16	21	22	***Conf 42***	2	5	7	13	15	18	21	22
Conf 8	2	6	13	15	16	18	21	22	***Conf 43***	1	6	7	13	15	16	19	21
Conf 9	1	6	10	13	16	18	21	22	***Conf 44***	1	2	7	13	15	18	19	22
Conf 10	2	6	10	13	15	18	21	22	***Conf 45***	1	5	7	15	16	18	19	22
Conf 11	2	6	7	10	13	15	19	22	***Conf 46***	2	6	7	10	13	18	21	22
Conf 12	2	6	7	13	15	16	21	22	***Conf 47***	2	6	7	13	16	18	19	22
Conf 13	1	6	10	13	15	16	21	22	***Conf 48***	1	5	7	13	15	16	19	22
Conf 14	1	2	7	10	13	15	21	22	***Conf 49***	1	6	7	10	15	16	19	22
Conf 15	2	6	7	10	13	16	19	22	***Conf 50***	5	6	10	13	15	18	21	22
Conf 16	1	6	10	15	16	18	21	22	***Conf 51***	2	5	7	10	16	18	19	21
Conf 17	1	2	10	13	16	18	21	22	***Conf 52***	5	6	7	13	16	18	19	22
Conf 18	1	2	10	15	16	18	21	22	***Conf 53***	5	6	7	13	16	18	21	22
Conf 19	1	6	7	13	15	16	21	22	***Conf 54***	1	2	7	15	16	18	21	22
Conf 20	1	2	7	10	13	16	21	22	***Conf 55***	5	6	10	15	16	18	19	21
Conf 21	1	2	13	15	16	18	19	22	***Conf 56***	1	5	7	10	16	18	19	22
Conf 22	2	6	7	15	16	18	21	22	***Conf 57***	5	6	7	15	16	18	19	21
Conf 23	2	6	7	10	15	16	21	22	***Conf 58***	5	6	7	10	16	18	19	22
Conf 24	2	6	7	13	15	18	21	22	***Conf 59***	1	2	7	10	13	18	19	22
Conf 25	1	6	13	15	16	18	21	22	***Conf 60***	1	5	7	10	16	18	21	22
Conf 26	1	2	7	10	13	15	19	22	***Conf 61***	1	2	7	13	15	18	19	21
Conf 27	2	6	10	13	15	16	19	22	***Conf 62***	5	6	7	10	15	18	19	21
Conf 28	1	6	10	13	15	18	21	22	***Conf 63***	5	6	10	15	16	18	19	22
Conf 29	1	6	7	13	15	18	21	22	***Conf 64***	1	5	7	13	15	18	19	21
Conf 30	2	6	10	13	16	18	19	22	***Conf 65***	5	6	7	10	13	18	21	22
Conf 31	1	2	10	13	16	18	19	22	***Conf 66***	1	5	7	10	16	18	19	21
Conf 32	2	5	7	10	13	16	21	22	***Conf 67***	5	6	7	10	16	18	19	21
Conf 33	1	2	10	13	15	18	21	22	***Conf 68***	1	5	7	13	16	18	19	21
Conf 34	2	5	7	10	13	15	21	22	***Conf 69***	2	5	7	13	16	18	19	21
Conf 35	2	6	7	13	15	16	19	22	***Conf 70***	5	6	7	13	16	18	19	21

However, some limits must be highlighted, the computational cost of the procedure is burdensome and the results obtained from different applications [22, 23] show that the results obtained from different regularisation techniques depend strictly on the FRF matrix of the structure. In particular the use of regularisation techniques implies that

Table 2.8: I_{NORM} obtained by experimental FRF with different configurations, indices averaged over frequency and drive points

	DSVD			Tikhonov			TSVD			DSVD			Tikhonov			TSVD	
	Q. Opt	GCV	L-Curve	Q. Opt	GCV	L-Curve	Q. Opt	GCV		Q. Opt	GCV	L-Curve	Q. Opt	GCV	L-Curve	Q. Opt	GCV
Conf 1	68	68	72	58	71	79	42	66	*Conf 36*	69	69	73	59	71	80	36	66
Conf 2	69	69	73	59	72	79	42	67	*Conf 37*	68	68	72	56	70	79	41	65
Conf 3	66	66	71	55	68	78	40	63	*Conf 38*	65	65	69	49	67	76	34	62
Conf 4	69	69	73	60	73	80	36	65	*Conf 39*	69	69	73	60	72	80	38	65
Conf 5	68	68	72	60	72	80	41	64	*Conf 40*	65	65	70	50	66	76	34	61
Conf 6	69	69	72	59	72	80	39	64	*Conf 41*	67	67	70	50	68	76	35	62
Conf 7	68	68	72	58	71	79	40	64	*Conf 42*	67	67	73	61	72	80	43	68
Conf 8	68	68	72	57	72	79	37	66	*Conf 43*	71	71	74	53	72	79	37	66
Conf 9	68	68	72	58	70	80	40	64	*Conf 44*	66	66	70	52	68	76	39	64
Conf 10	69	69	72	58	72	80	43	68	*Conf 45*	66	66	72	52	68	77	37	64
Conf 11	64	64	70	52	66	76	37	64	*Conf 46*	69	69	73	61	74	80	37	67
Conf 12	70	70	73	59	72	80	35	65	*Conf 47*	68	68	71	50	69	76	29	63
Conf 13	69	69	72	57	70	79	44	67	*Conf 48*	67	67	73	53	69	76	37	65
Conf 14	67	67	72	58	69	79	40	64	*Conf 49*	66	66	71	52	69	76	34	62
Conf 15	66	66	70	51	68	77	34	63	*Conf 50*	69	69	74	62	72	80	43	69
Conf 16	68	68	72	57	70	79	44	66	*Conf 51*	68	68	74	57	71	79	43	66
Conf 17	67	67	72	60	70	80	36	64	*Conf 52*	66	66	72	49	68	77	38	63
Conf 18	67	67	72	59	70	79	40	63	*Conf 53*	68	68	74	57	72	79	38	66
Conf 19	70	70	73	57	71	80	36	66	*Conf 54*	70	70	73	60	72	80	39	64
Conf 20	67	67	72	60	69	80	42	63	*Conf 55*	69	69	74	55	71	79	38	68
Conf 21	65	65	69	49	66	75	37	62	*Conf 56*	64	64	72	50	66	77	40	66
Conf 22	69	69	72	60	72	79	39	62	*Conf 57*	68	68	73	53	70	78	35	66
Conf 23	68	68	72	60	71	79	38	62	*Conf 58*	65	65	71	49	67	77	35	63
Conf 24	69	69	72	59	72	80	41	67	*Conf 59*	65	65	69	50	67	76	32	61
Conf 25	67	67	71	54	69	78	39	66	*Conf 60*	68	68	74	62	73	81	41	70
Conf 26	65	65	70	52	67	76	37	63	*Conf 61*	68	68	73	54	70	79	39	67
Conf 27	65	65	70	50	67	76	35	63	*Conf 62*	68	68	73	55	71	78	35	64
Conf 28	68	68	72	57	70	79	44	66	*Conf 63*	65	65	72	53	68	78	35	66
Conf 29	69	69	72	57	71	79	38	66	*Conf 64*	69	69	74	58	71	79	43	68
Conf 30	67	67	71	53	69	77	32	63	*Conf 65*	68	68	73	57	72	80	41	68
Conf 31	65	65	70	51	67	76	36	61	*Conf 66*	68	68	74	56	71	79	39	67
Conf 32	69	69	74	63	73	81	42	71	*Conf 67*	68	68	73	53	70	78	37	66
Conf 33	67	67	72	59	70	79	42	65	*Conf 68*	69	69	75	56	71	79	37	67
Conf 34	68	68	74	61	72	81	42	69	*Conf 69*	69	69	75	57	71	79	41	67
Conf 35	67	67	71	50	69	76	32	62	*Conf 70*	69	69	74	54	71	79	35	65

Table 2.9: I_{AVG} obtained by experimental FRF with different configurations, indices averaged over frequency and drive points

	DSVD			Tikhonov			TSVD			DSVD			Tikhonov			TSVD	
	Q. Opt	GCV	L-Curve	Q. Opt	GCV	L-Curve	Q. Opt	GCV		Q. Opt	GCV	L-Curve	Q. Opt	GCV	L-Curve	Q. Opt	GCV
Conf 1	67	67	71	59	72	81	47	72	*Conf 36*	68	68	72	60	72	81	40	73
Conf 2	68	68	72	60	74	81	47	74	*Conf 37*	67	67	71	57	71	80	45	73
Conf 3	65	65	70	55	69	79	44	70	*Conf 38*	65	65	69	49	68	77	38	69
Conf 4	69	69	72	60	74	82	40	73	*Conf 39*	68	68	72	60	73	81	42	72
Conf 5	67	67	71	61	73	81	46	71	*Conf 40*	64	64	69	50	68	77	38	69
Conf 6	68	68	71	60	73	81	43	70	*Conf 41*	66	66	70	51	69	78	40	70
Conf 7	67	67	71	58	71	81	44	71	*Conf 42*	67	67	73	62	74	82	47	74
Conf 8	67	67	71	57	73	80	41	73	*Conf 43*	71	71	73	54	74	81	41	74
Conf 9	67	67	71	58	71	81	44	71	*Conf 44*	65	65	69	53	69	77	44	71
Conf 10	68	68	72	59	73	81	47	75	*Conf 45*	66	66	72	53	70	79	41	72
Conf 11	63	63	69	52	67	77	41	71	*Conf 46*	68	68	72	62	75	82	41	74
Conf 12	69	69	72	60	74	81	39	72	*Conf 47*	67	67	71	51	70	78	33	71
Conf 13	68	68	72	58	71	81	49	74	*Conf 48*	67	67	73	55	72	79	41	73
Conf 14	66	66	71	59	70	80	44	71	*Conf 49*	66	66	70	53	71	78	38	70
Conf 15	65	65	70	51	69	78	38	71	*Conf 50*	68	68	74	62	73	82	47	76
Conf 16	67	67	71	58	71	80	48	72	*Conf 51*	68	68	74	58	73	82	47	73
Conf 17	66	66	71	60	71	81	40	71	*Conf 52*	66	66	72	50	70	79	42	71
Conf 18	66	66	71	59	70	81	44	70	*Conf 53*	68	68	73	58	73	81	41	73
Conf 19	69	69	73	58	73	81	40	74	*Conf 54*	69	69	72	60	73	81	43	71
Conf 20	66	66	71	61	70	81	47	71	*Conf 55*	68	68	73	56	73	81	41	77
Conf 21	64	64	69	49	68	77	42	69	*Conf 56*	64	64	72	51	68	79	44	73
Conf 22	68	68	71	61	73	81	43	69	*Conf 57*	68	68	73	54	72	80	39	74
Conf 23	67	67	71	61	72	80	43	69	*Conf 58*	64	64	71	50	68	78	38	71
Conf 24	68	68	71	60	73	81	45	73	*Conf 59*	65	65	69	50	69	77	36	69
Conf 25	66	66	70	54	70	79	43	73	*Conf 60*	68	68	74	63	74	83	44	77
Conf 26	64	64	69	52	69	78	42	71	*Conf 61*	68	68	72	55	72	81	43	75
Conf 27	65	65	70	51	69	77	39	70	*Conf 62*	68	68	73	56	73	81	39	72
Conf 28	67	67	71	58	71	80	48	73	*Conf 63*	65	65	71	54	69	79	39	74
Conf 29	68	68	71	58	72	80	43	73	*Conf 64*	69	69	75	60	74	82	47	75
Conf 30	66	66	70	54	70	78	36	71	*Conf 65*	67	67	73	57	73	81	45	74
Conf 31	65	65	69	51	69	78	40	69	*Conf 66*	69	69	75	58	74	82	43	75
Conf 32	68	68	73	64	74	82	46	77	*Conf 67*	68	68	73	54	72	80	42	74
Conf 33	66	66	71	60	71	80	46	72	*Conf 68*	70	70	75	58	74	82	41	76
Conf 34	67	67	74	62	73	82	46	75	*Conf 69*	70	70	75	59	74	82	46	75
Conf 35	67	67	71	51	71	78	36	70	*Conf 70*	69	69	74	56	74	81	40	72

some information are deleted without knowing exactly the influence of this suppression on the final result. The physical meaning of erasing information by working directly on the singular values is absolutely not evident.

2.2 Reduction of ill-conditioning by a physical approach

The regularisation techniques decrease the wealth of information of the FRF matrix. In fact, as shown in section 1.1.1, these techniques cut the meaningless information that increase the ill-conditioning. The question is: how many information is possible to cut to obtain meaningful results?
An answer can be obtained by investigating the value assumed by the condition number when the degrees of freedom of the FRF are conveniently reduced [24].
First of all it must be considered the distribution of the FRF values in correspondence of each frequency. Consider the FRF of the structure computed, taking into account 24 points and 3 DoF for each point. For a better understanding the values assumed by the mobility in correspondence of two selected frequencies, 99 Hz and 661 Hz (resonance), are shown in figure 2.11. The distribution of the values in the matrix is not uniform and

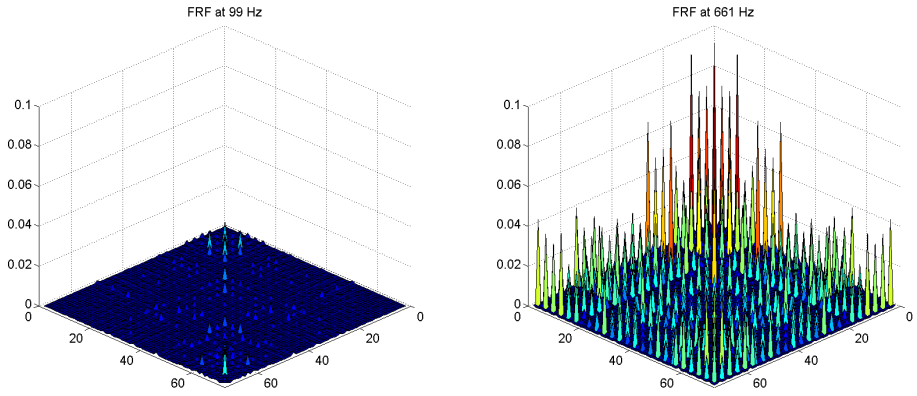

Figure 2.11: Comparison between FRF matrices at 99 Hz and 661 Hz (resonance)

the gap between the values assumed by the mobility at each DoF at the resonance is 10 times higher than the one assumed at the other frequency (99Hz). The FRF values distribution at the resonance has a counterpart in the values assumed by the condition number of the FRF matrix. As known, to reduce the ill-conditioning of the matrix some information must be deleted to avoid an increase of error due to the information loss. This suggests that the ill-conditioning of the FRF matrix, computed by taking into account only the prevailing DoF (one for each point) decreases.
In figure 2.12 it is shown the comparison between the condition number of numerical FRF computed taking into account 3 Degree of Freedom for each point (72 DoF) and

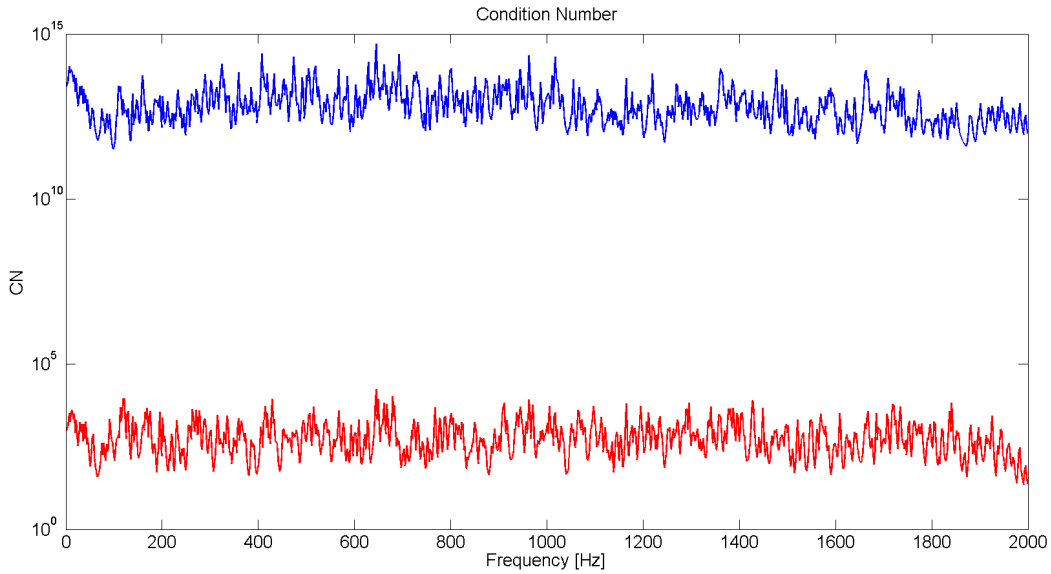

Figure 2.12: Comparison between condition numbers:
72 DoF FRF(blue), and 24 DoF FRF(red).

Frquency Hz	Condition number of 72 DoF	Condition number of 24 DoF
99	3,29E+11	1,64E+02
661	1,16E+14	6,72E+03

Table 2.10: Condition number of FRF at the two considered frequencies

only the principal DoF for each point (24 DoF). As expected the values of the second one is significantly lower.
Figure 2.13 shows the FRF values distribution for both cases (24 DoF and 72 DoF) at the two considered frequencies, 99 Hz and 661 Hz (resonance). The corresponding condition number is reported in table 2.10.
To understand the relationship between these results and the use of regularisation techniques, the singular values of FRF matrix at 661 Hz for the two considered cases are drawn in figure 2.14: the smallest singular values belong to the 72 DoF FRF. These simple results show that the reduction of information due to the deletion of not significant degrees of freedom implies a significant reduction of the ill-conditioning of the problem. This kind of approach allows to reduce the ill-conditioning, knowing exactly what information we are neglecting.

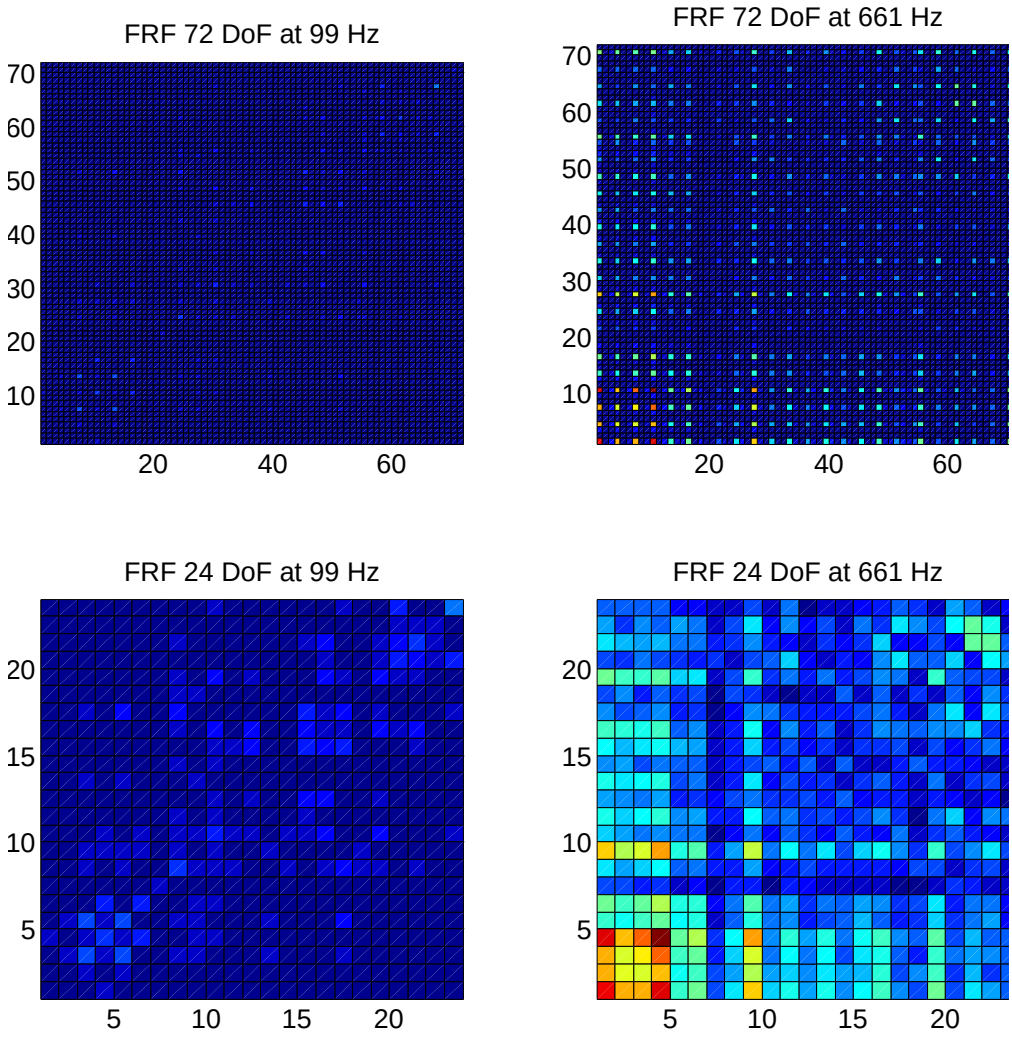

Figure 2.13: Comparison between FRF matrices, 72 DoF and 24 DoF, at 99 Hz and at 661 Hz (resonance)

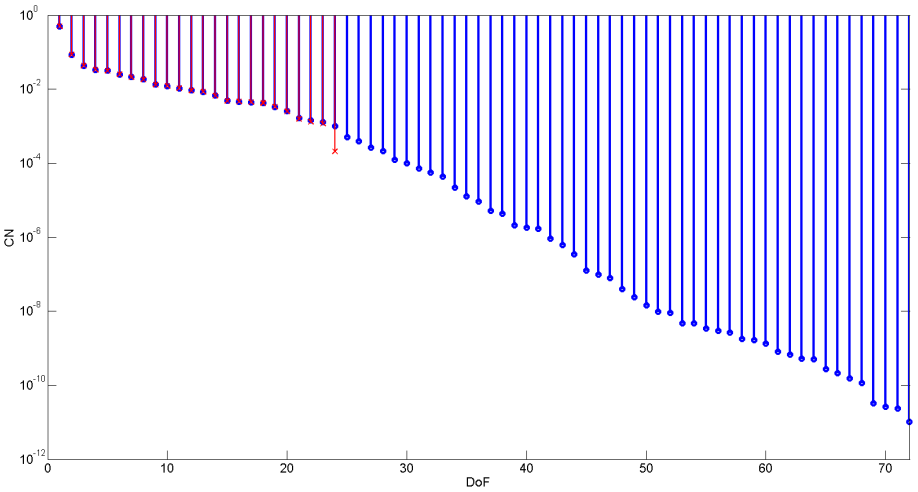

Figure 2.14: Comparison between singular values at 661 Hz. 72 DoF FRF matrix (blue), and 24 DoF FRF matrix (red).

2.3 Force identification: numerical results

In this section, the procedure presented to reduce the ill-conditioning of the FRF matrix is applied to identify different kinds of load (point force, distributed force, deterministic force or random force).
The numerical FRF matrix is calculated using numerical eigenvalues and eigenvectors obtained by FEM. For deterministic loads the velocity of each point is computed by the following equation:

$$\overline{\mathbf{v}}(\omega) = \mathbf{Y}(\omega)\mathbf{f}(\omega) + \varepsilon_v(\omega) \tag{2.6}$$

where $\mathbf{f}(\omega)$ is the external force, $\mathbf{Y}$ is the mobility matrix and $\overline{\mathbf{v}}$ is the calculated velocity that is considered equivalent to the measured velocity. The velocity is polluted by a random noise proportional to the velocity rms, ε_v. The force is identified by inverting the $\mathbf{Y}$ matrix.
The most general case takes into account the lack of knowledge of force position and intensity. In this section, the force identification is performed for deterministic and not deterministic loads and for a set of measurement points overlapping and not entirely overlapping the applied force positions.
Consider the structure shown in figure 2.1. Its FRF matrix is reduced by considering only one DoF for each measurement point: the flexural velocity. This choice reduces the ill-conditioning of the full FRF matrix, as shown in section 2.2.

2.3.1 Deterministic load

The identification of an impulsive force (constant spectrum on the frequency range) is investigated. This kind of load is useful in the analysis of results, indeed it makes possible to evaluate the results averaged on frequency. The identification is carried out for two different cases:

a. $\mathbf{m} = \mathbf{n}$: the measurement points $\boldsymbol{m}$ overlap the set of all $\boldsymbol{n}$ points;
the set of $\boldsymbol{m}$ points where the dynamic response is computed corresponds to the whole set of considered $\boldsymbol{n}$ points on the structure

$$\begin{aligned} \mathbf{f}_{id}(\omega) &= \mathbf{Y}(\omega)^{-1}\overline{\mathbf{v}}(\omega) \\ (n \times 1) &= (n \times n)\,(n \times 1) \end{aligned} \tag{2.7}$$

b. $\mathbf{m} < \mathbf{n}$: the measurement $\boldsymbol{m}$ points do not overlap the whole set of $\boldsymbol{n}$ points;
the set of $\boldsymbol{m}$ points where the dynamic response is computed is a subset of the whole set of considered $\boldsymbol{n}$ points on the structure

$$\begin{aligned} \mathbf{f}_{id}(\omega) &= \mathbf{Y}(\omega)^{+}\overline{\mathbf{v}}(\omega) \\ (n \times 1) &= (n \times m)\,(m \times 1) \end{aligned} \tag{2.8}$$

In this second case the problem is under-determined, therefore, computing the minimum norm solution the amplitude of the identified force could be overestimated in correspondence of the measured points $\boldsymbol{m}$ where the response is calculated. Hence the identified vector is multiply by an appropriate factor. This factor modify the amplitude of the components proportionally to the number of degree of freedom eliminated from the solution.

Point loads The configurations of measurement points are shown in table 2.11,

Table 2.11: point load identification

		Point load
$m = n$	$\boldsymbol{n}$	[1 ... 24]
	$\boldsymbol{m}$	[1 ... 24]
	$\boldsymbol{p}$	[2 ; 9 ; 16 ; 23]
$m < n$	$\boldsymbol{n}$	[1 ... 24]
	$\boldsymbol{m}$	[1; 5; 10; 11; 14; 18; 19; 22]
	$\boldsymbol{p}$	[2 ; 9 ; 16 ; 23]

where n is the number of the whole set of considered points on the structure, m is the number of measurement points and p are the excitation points. When $m < n$ any point of the selected set of points is a measurement point.

In order to select the best configuration of points m, the condition number is evaluated for all the possible combinations of points. The combination that gives the lowest condition number value is selected. Figure 2.15 shows the comparison between the condition number of the FRF matrix for $m = n$ and $m < n$. Note that the values assumed for the reduced set of points are lower at all frequencies.

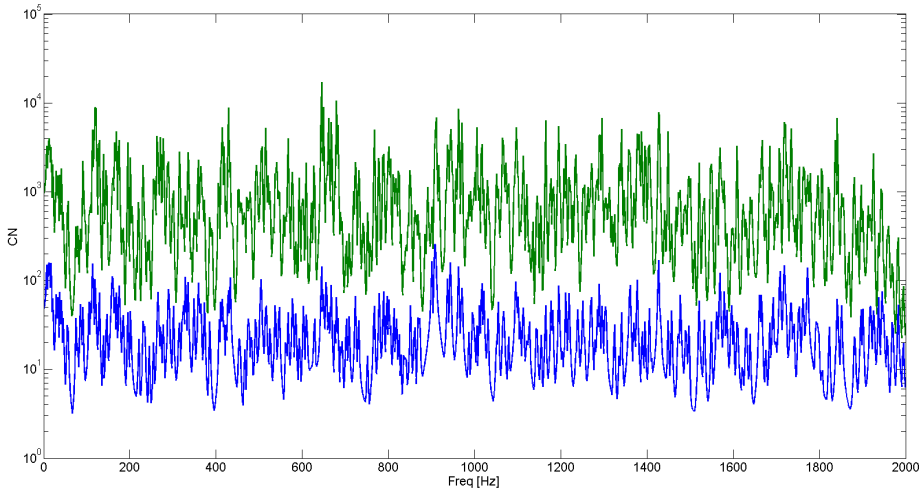

Figure 2.15: Condition number of FRF matrix:
n=m=24 (green) and *n=24, m=8* (blue)

The identification is carried out using the procedure explained in the previous section between 1 Hz and 2000 Hz. The velocity is polluted with a random noise: 5% of its rms. The results shown in figure 2.16 are averaged over the studied frequency range. They are satisfied for both considered configurations. The identification of the position is correct in both cases, the amplitude is correct for $m = n$ and, as expected, is underestimated in the case $m < n$. The mean relative error computed in correspondence of the excited points, in the case $m = n$ is less than 5% and it increases to 15,3% for $m < n$. In the instance $m = n$, the reduction of ill-conditioning, performed taking into account one degree of freedom for each considered point, avoid the error amplification in the data. The results obtained in the instance $m < n$ show that the low ill-conditioning compensates only in part the lack of information due to the reduced set of measurement points.

Distributed load In this application, distributed load means that an impulsive load is applied simultaneously at all points of the second plate as shown in table 2.12. Here, several excitation points coincide with measurement points.
Figure 2.17 shows the result obtained in the two cases, $m = n$ and $m < n$. As in the previous test, the position is estimated correctly in both cases, the spurious components

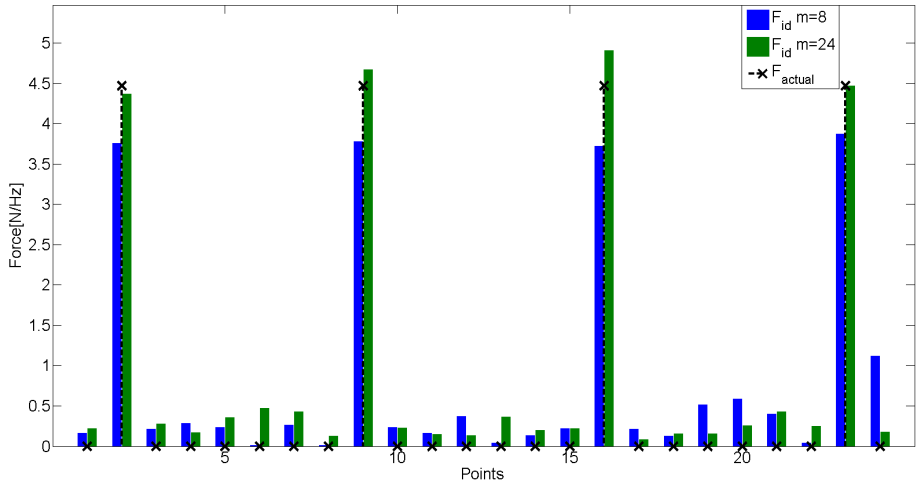

Figure 2.16: Deterministic point loads: comparison between the actual force ($-\times-$), the force identified in the case *n=m=24* (green) and in the case *n=24, m=8* (blue)

Table 2.12: Distributed load identification

		Distributed
$m = n$	$\boldsymbol{n}$	[1 ... 24]
	$\boldsymbol{m}$	[1 ... 24]
	$\boldsymbol{p}$	[7 ... 19]
$m < n$	$\boldsymbol{n}$	[1 ... 24]
	$\boldsymbol{m}$	[1; 5; 10; 11; 14; 18; 19; 22]
	$\boldsymbol{p}$	[7 ... 19]

of the identified force on the plate 1 and 3 being significantly lower than the actual one. The amplitude is close to the actual one in the case $m = n$, the mean relative error is less than 7%, but it grows up to 15% when $n = 24$ and $m = 8$.

2.3.2 Not deterministic load

For random loads, the power spectral densities of force and velocity are taken into account. These are their definitions [25, 26]:

$$\mathbf{S_{vv}}(\omega) = \int_{-\infty}^{+\infty} R_{vv}(\tau) e^{-j\omega\tau} d\tau = \lim_{T\to\infty} \frac{1}{T} E\left[\overline{v}(\omega)^* \overline{v}^T(\omega)\right] \tag{2.9}$$

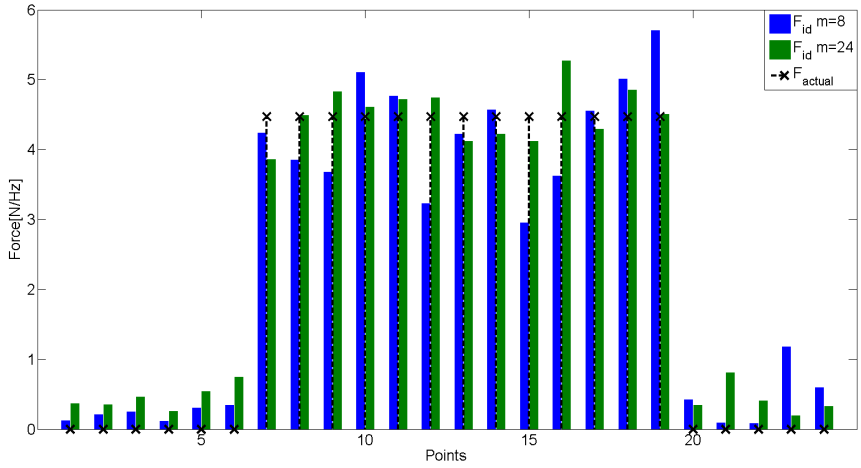

Figure 2.17: Deterministic distributed loads: comparison between the actual force($- \times -$), the identified in the case *n=m=24* (green) and in the case *n=24, m=8* (blue)

$$\mathbf{S_{ff}}(\omega) = \int_{-\infty}^{+\infty} R_{ff}(\tau) e^{-j\omega\tau} d\tau = \lim_{T\to\infty} \frac{1}{T} E\left[\overline{f}(\omega)^* \overline{f}^T(\omega)\right] \tag{2.10}$$

The input-output relationship becomes:

$$\overline{\mathbf{S}}_{vv}(\omega) = \mathbf{Y}(\omega)^* \mathbf{S}_{ff} \mathbf{Y}(\omega)^T + \varepsilon_{S_{vv}} \tag{2.11}$$

where $\overline{\mathbf{S}}_{vv}$ is the calculated velocity power spectral density matrix, $*$ indicates the complex conjugate and $\varepsilon_{S_{vv}}$ is the error proportional to the rms velocity. Matrix S_{ff} is identified by inverting equation (2.11) and considering the reduced $\mathbf{Y}$ matrix as follows:

$$\mathbf{S}_{ff}(\omega) = \mathbf{Y}(\omega)^{*^+} \overline{\mathbf{S}}_{vv}(\omega) \mathbf{Y}(\omega)^{T^+} \tag{2.12}$$

In figure 2.18 the diagram summarizing the procedure is shown.

The identification of a white random noise is investigated. Also this kind of load is a broadband load, therefore it makes possible to evaluate the results averaged on frequency. The identification is performed as shown in figure 2.18: the numerical power spectral density of the velocity is computed by equation (2.11) in correspondence of all the considered points **n** applying a white random noise in correspondence of **p** points. The velocity is polluted by a random noise proportional to 2% of rms value.

a. $\mathbf{m} = \mathbf{n}$. The dimension of the force vector is the same of the measured response, the mobility matrix is squared and the equation has the following dimensions:

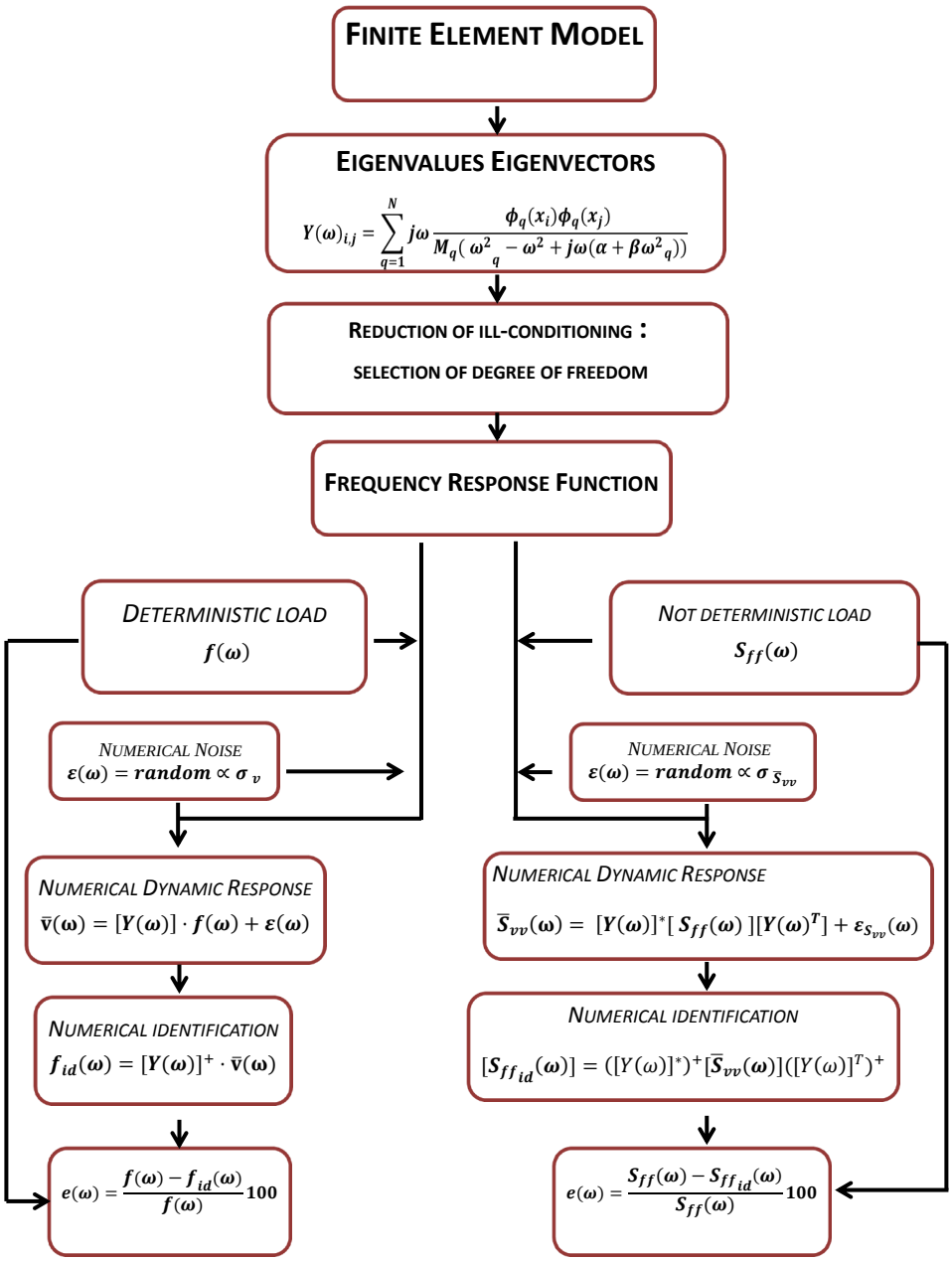

Figure 2.18: Diagram of the numerical identification procedure

$$\begin{aligned} \mathbf{S}_{ff_{id}}(\omega) &= \mathbf{Y}(\omega)^{*^{-1}}\overline{\mathbf{S}}_{vv}(\omega)\mathbf{Y}(\omega)^{T^{-1}} \\ (n \times n) &= (n \times n)\,(n \times n)\,(n \times n) \end{aligned} \tag{2.13}$$

b. $\mathbf{m} < \mathbf{n}$. The dimension of the force vector is larger than the dimension of the measured response, the mobility matrix is rectangular and the problem has the following dimensions:

$$\begin{aligned} \mathbf{S}_{ff_{id}}(\omega) &= Y(\omega)^{*^{+}}\overline{\mathbf{S}}_{vv}(\omega)\mathbf{Y}(\omega)^{T^{+}} \\ (n \times n) &= (n \times m)\,(m \times m)\,(m \times n). \end{aligned} \tag{2.14}$$

As shown by Nelson and Yoon [13] the PSD is more sensitive to the errors in the data. Indeed, considering the errors $\varepsilon_{S_{vv}}$ and $\varepsilon_{S_{ff}}$:

$$\varepsilon_{S_{ff}} = \mathbf{Y}(\omega)^{*^{+}}\varepsilon_{S_{vv}}\mathbf{Y}(\omega)^{T^{+}} \tag{2.15}$$

by using the property of the norm on the above equation and on the equation (2.13):

$$\begin{aligned} ||\varepsilon_{S_{ff}}|| &\leq ||\mathbf{Y}^{*^{+}}||\,||\varepsilon_{S_{vv}}||\,||\mathbf{Y}^{T^{+}}|| \\ ||\mathbf{S}_{ff}|| &\leq ||\mathbf{Y}^{*^{+}}||\,||\mathbf{S}_{vv}||\,||\mathbf{Y}^{T^{+}}|| \end{aligned} \tag{2.16}$$

it is possible to write the follow equation:

$$||\varepsilon_{S_{ff}}||\,||\mathbf{S}_{vv}|| \leq ||\mathbf{Y}(\omega)^{*}||\,||\mathbf{Y}(\omega)^{*^{+}}||\,||\mathbf{Y}(\omega)^{T}|| \quad ||\mathbf{Y}(\omega)^{T^{+}}||\,||\varepsilon_{S_{vv}}||\,||\mathbf{S}_{ff}|| \tag{2.17}$$

Then:

$$\frac{||\varepsilon_{S_{ff}}||}{||\mathbf{S}_{ff}||} \leq CN(\mathbf{Y}^{*})CN(\mathbf{Y}^{T})\frac{||\varepsilon_{S_{vv}}||}{||\mathbf{S}_{vv}||} \tag{2.18}$$

Since the $CN(\mathbf{Y}^{*})$ is equal to $CN(\mathbf{Y}^{T})$ the above equation becomes:

$$\frac{||\varepsilon_{S_{ff}}||}{||\mathbf{S}_{ff}||} \leq CN(\mathbf{Y})^{2}\frac{||\varepsilon_{S_{vv}}||}{||\mathbf{S}_{vv}||} \tag{2.19}$$

The last equation shows that the ratio between the auto spectral densities of velocity and force is more sensitive to errors in the data than the ratio between the respective Fourier transform.

$$\frac{||\mathbf{S}_{vv}||}{||\mathbf{S}_{ff}||} \leq CN(\mathbf{Y})^{2}\frac{||\varepsilon_{S_{vv}}||}{||\varepsilon_{S_{ff}}||} \tag{2.20}$$

while:

$$\frac{||\mathbf{v}||}{||\mathbf{f}||} \leq CN(\mathbf{Y})\frac{||\varepsilon_v||}{||\varepsilon_f||} \tag{2.21}$$

Therefore, in order to identify random loads, the presented reduction techniques of the ill-conditioning could not be enough to get the load identification.

Point loads The structure is excited simultaneously on the p points of table 2.11 by white random noise and the power spectral density of the force is identified in the two cases $m = n$ and $m < n$. The simulation is performed in a frequency range from 1 to 2000 Hz. In the case $m = n$ the identification of the force position fails as shown in figure 2.19.

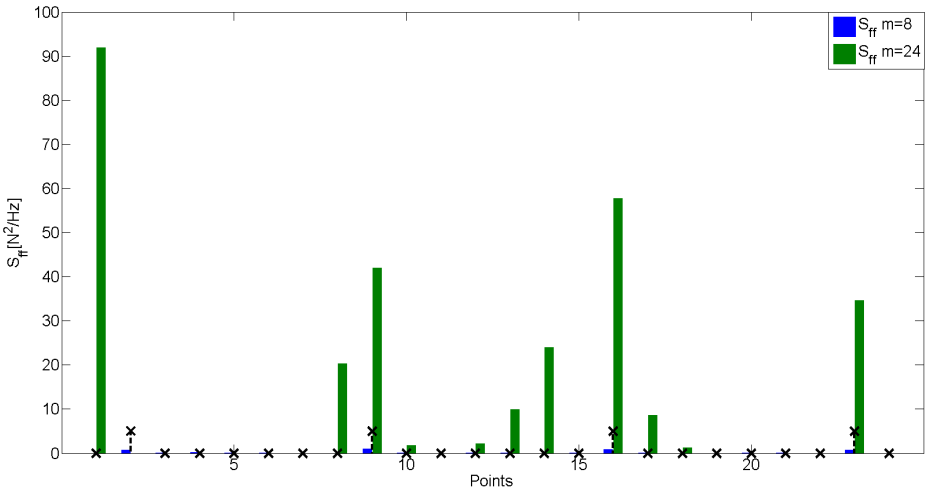

Figure 2.19: Random point loads. Comparison between the actual force ($- \times -$), the identified force in the case *n=m=24* (green) and in the case *n=24, m=8* (blue)

Figure 2.20 shows the comparison between the actual PSD of the force and the identified one in the case $m < n$; the identification of the position is correct, but the amplitude is underestimated.
From the comparison of the results in figure 2.19 and figure 2.20 it is possible to notice that the reduced set of points gives better results than the full set of points, despite the lack of information. The reason of this result could be find in the increased gap between the condition numbers of the two cases, indeed it is at the power 2 in equation (2.20).
Although the identified S_{ff} does not match the actual value, it is interesting to study the behaviour of the power injected into the structure. The cross power spectral density force-velocity, S_{fv}, is calculated by the following equation:

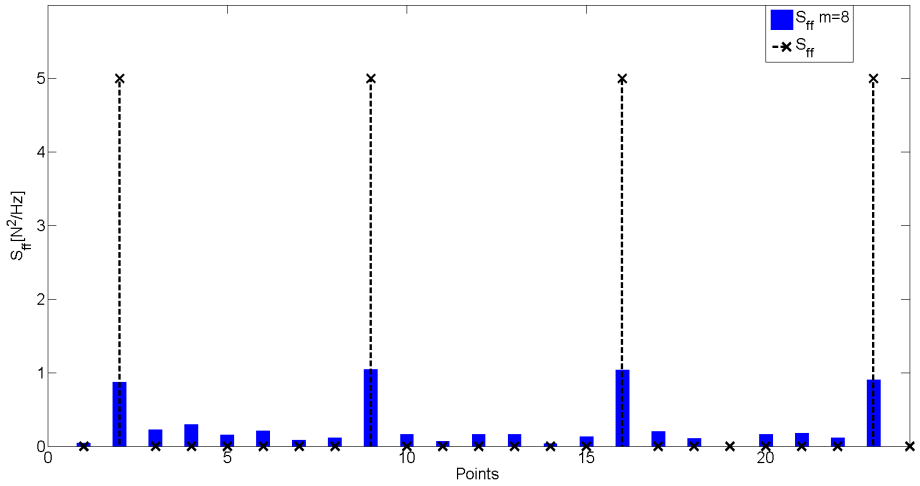

Figure 2.20: Random point loads. Comparison between the actual force $(- \times -)$ and the identified force in the case *n=24, m=8* (blue)

$$\mathbf{S}_{fv}(\omega) = \mathbf{S}_{ff_{id}}(\omega)\mathbf{Y}(\omega)^T \tag{2.22}$$

The power injected is obtained by the following relationship:

$$P_{in} = \int_{\omega_1}^{\omega_2} Re[\,\mathbf{S}_{fv}(\omega)]d\omega \tag{2.23}$$

As shown in figure 2.21, the identified injected power, gives good results regarding to the identification of the position, both for $m = n = 24$ and $m < n$. The amplitude identification gives better results than those obtained for S_{ff}, but the values are not satisfactory. As it is clear from equation (2.22), in the identification of the injected power the influence of the condition number return to be linear; this influence is reflected in the results shown in figures 2.21, indeed it is possible to perform the identification of the actual position of the load.

Distributed loads The structure is excited simultaneously by white random noise on all the points of the second plate (see table 2.12) and the results are shown in figure 2.22.
As in the case of point loads, the identification of the power spectral density of the force does not give good results in the case $m = n$. Figure 2.23 shows the results obtained in the case $m < n$: also in this case it is possible to identify the position of the force while the amplitude of the PSD is underestimated.
Figure 2.24 shows the identified injected power.

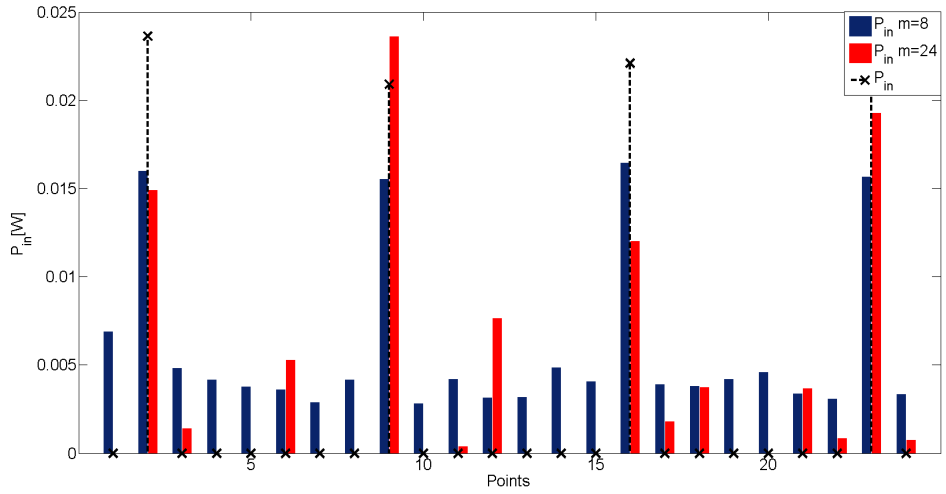

Figure 2.21: Random point loads. Comparison between the actual injected power ($- \times -$), the identified power in the case *n=m=24* (red) and in the case *n=24, m=8* (blue)

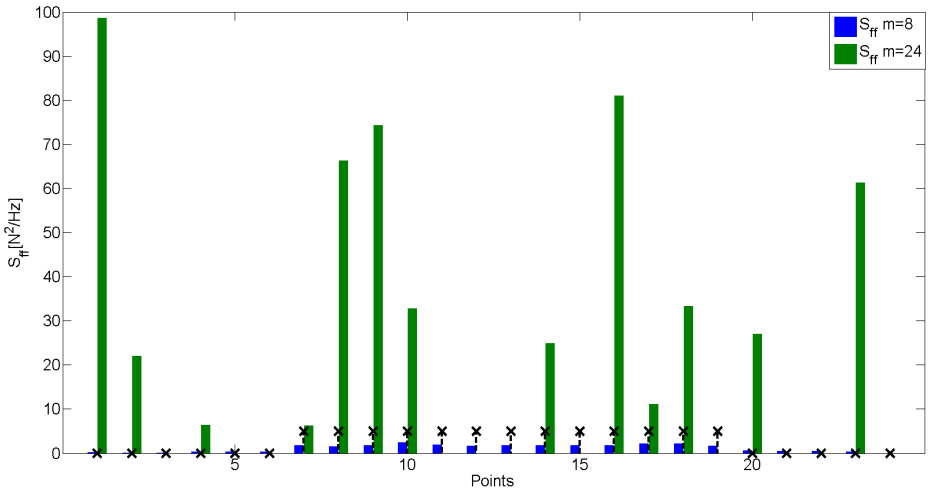

Figure 2.22: Random distributed load. Comparison between the actual force ($- \times -$), the identified force in the case *n=m=24* (green) and in the case *n=24, m=8* (blue)

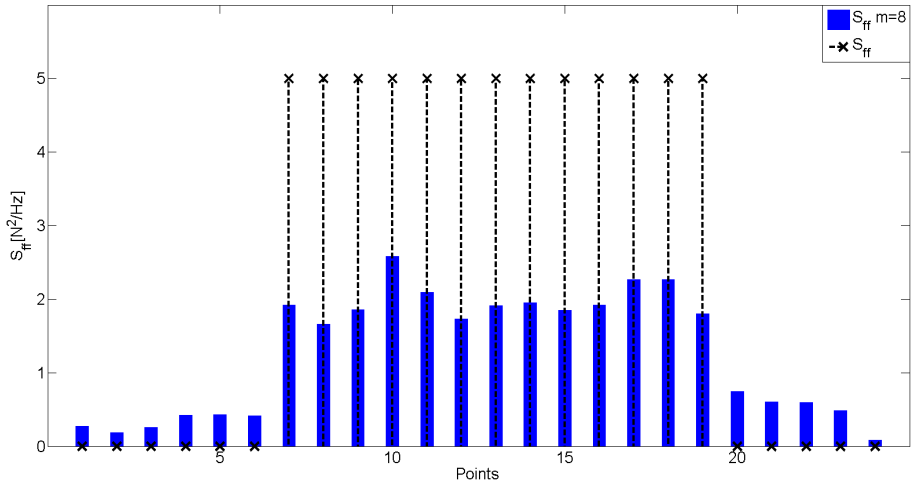

Figure 2.23: Random distributed load. Comparison between the actual force ($-\times-$) and the identified force in the case and *n=24, m=8* (blue)

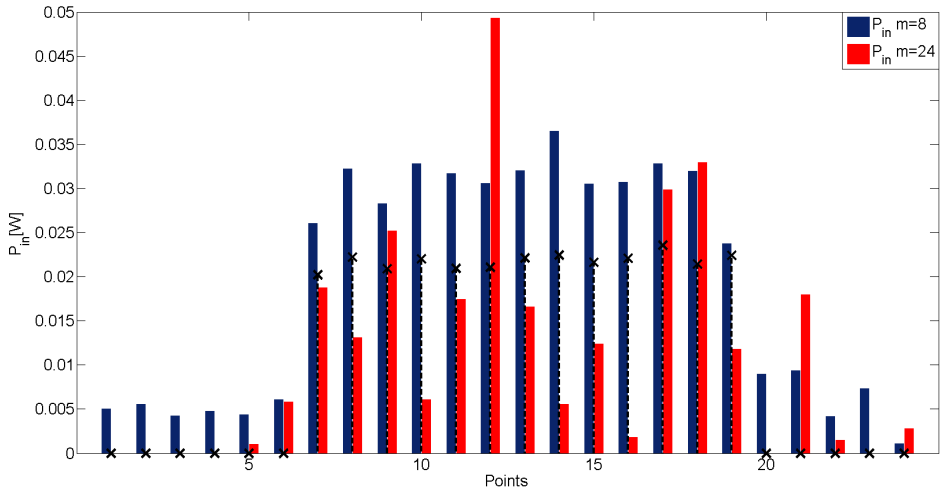

Figure 2.24: Random distributed loads. Comparison between the actual injected power ($-\times-$), the identified power in the case *n=m=24* (red) and in the case *n=24, m=8* (blue)

The identification of the injected power gives good results only for the force location in the case $m < n$.

Conclusions The results presented in this chapter show that the reduction of ill-conditioning by cutting not essential degrees of freedom could be a way to proceed in the solution of the identification of deterministic loads. In fact, it gives good results also by considering a little subset of measuring points on the structure. It is important to emphasize that for the studied structure this concept could seams trivial, but it becomes decisive and not trivial when the geometry of the structure is complex and it is not simple to select the relevant information.
On the contrary, this methodology fails when random forces must be identified. However the result obtained by using the injected power suggests that a possible approach to identify a non deterministic load could be based on an energetic method.

CHAPTER
THREE

IDENTIFICATION BY COHERENCE BASED APPROACH

Until now the thesis is focused on the numerical reduction of the ill conditioning problem by conventional techniques.
The results show that the investigated techniques, although computationally heavy, are suitable in the case of deterministic loads, but are unsatisfactory for the identification of not deterministic forces.
In this case, a different approach is required and this is the topic discussed in this chapter and in the next one.
Since the loads here considered are random, the input-output relationships to develop this new approach follows the linear operator spectral theory of random signals. Consequently physical quantities are expressed in terms of PSD. As it is seen the direct inversion of the FRF fails to identify the applied forces. The idea of this approach is to separate the localization problem from the amplitude identification, treating these two problems by different techniques and to avoid the ill-conditioning problem.
Therefore three steps can be recognized. The first one attends to the identification of the number of the applied forces by the velocity coherence analysis of the measured response. In the second step a factor named C_{vf}, defined as coherence between dummy force and measured responses, allows the identification of the force position. At last, the PSD of the force is identified by the input/output autospectrum relation of single input single output(SISO) models.
The validation of this proposed technique is analyzed in different experimental cases: Single Input Multi Output (SIMO) and Multi Input Multi Output (MIMO).

3.1 Theoretical background

Consider a SIMO model as in figure 3.1 where: $f(\omega)$ is the input force, $x_i(\omega)$ is the output velocity without noise and $v_i(\omega)$ is the output velocity affected by noise.

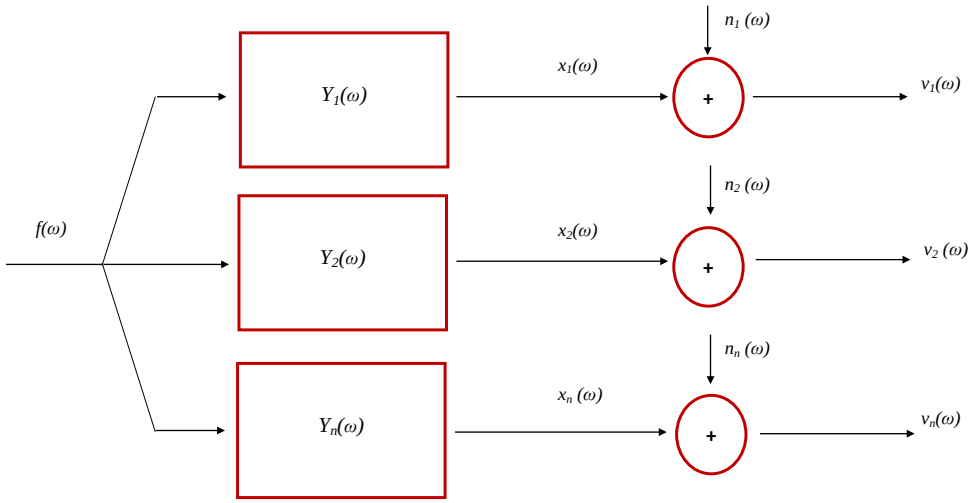

Figure 3.1: Single Input/ Multi Output system

Assuming that the noise signals are not coherent with the input signal and with each other noise, then [27]:

$$S_{fn_1} = S_{fn_2} = S_{fn_3} = S_{x_1n_1} = S_{x_2n_2} = S_{x_3n_3} = S_{n_1n_2} = S_{n_1n_3} = S_{n_2n_3} = 0$$

The PSD of the velocity v_1 is:

$$S_{v_1v_1} = S_{x_1x_1} + S_{n_1n_1} \tag{3.1}$$

and it is put in relation with the PSD force by:

$$S_{v_iv_i} = |Y_i|^2 S_{ff} \tag{3.2}$$

Therefore, by considering equation (3.2), equation (3.1) becomes:

$$S_{v_1v_1} = |Y_1|^2 S_{ff} + S_{n_1n_1}. \tag{3.3}$$

Similarly for the cross power spectral density (CPSD) between $f(\omega)$ and $v_1(\omega)$ the following equations are valid:

$$\begin{aligned} S_{fv_1} &= S_{fx_1} + S_{fn_1} \\ Sfv_1 &= S_{fx_1} = Y_1 S_{ff} \end{aligned} \tag{3.4}$$

and for the cross power spectral density between $v_1(\omega)$ and $v_2(\omega)$ are valid:

$$\begin{aligned} S_{v_1v_2} &= S_{x_1x_2} + S_{n_1n_2} \\ S_{v_1v_2} &= S_{x_1x_2} = Y_1^* Y_2 S_{ff}. \end{aligned} \tag{3.5}$$

Finally the coherence between the two output signals is defined as:

$$\gamma^2_{v_1v_2} = \frac{|S_{v_1v_2}|^2}{S_{v_1v_1}S_{v_2v_2}} \tag{3.6}$$

The numerator of the previous equation can be written by equation (3.5) as :

$$|S_{x_1x_2}|^2 = |Y_1^* Y_2 S_{ff}|^2 \tag{3.7}$$

and, by mathematical manipulation, it becomes:

$$|S_{x_1x_2}|^2 = (|Y_1|^2 S_{ff})(|Y_2|^2 S_{ff}) = S_{x_1x_1}S_{x_2x_2} \tag{3.8}$$

Considering that:

$$\gamma^2_{f_1v_1} = \frac{|S_{fv_1}|^2}{S_{ff}S_{v_1v_1}} = \frac{|Y_1 S_{ff}|^2}{S_{ff}S_{v_1v_1}} = \frac{S_{x_1x_1}}{S_{v_1v_1}} \tag{3.9}$$

equation (3.6) becomes:

$$\gamma^2_{v_1v_2} = \gamma^2_{fv_1}\gamma^2_{fv_2}. \tag{3.10}$$

Consider a multi input/multi output system as in figure 3.2, where the n virtual processes $f_1, ...f_n$ are uncorrelated [25].
It is possible to write:

$$\mathbf{S}_{vv}(\omega) = \mathbf{Y}(\omega)^* \mathbf{S}_{ff} \mathbf{Y}(\omega)^T \tag{3.11}$$

and the terms out of diagonal of matrix $\mathbf{S}_{ff}$ are equal to zero.
Therefore, for each diagonal element of S_{vv} we can write:

$$S_{v_iv_i}(\omega) = \sum_{j=1}^{n} |Y_{ij}(\omega)|^2 S_{f_jf_j}(\omega) \tag{3.12}$$

As Shin and Hammond [25] noticed, in the estimation of the FRF function of a structure excited by two uncorrelated sources, the coherence of the output is strictly related with the values assumed by the coherence of the input-output. In a general case it is possible to write the following equation:

$$S_{yy} = \gamma^2_{fy_1} S_{yy_1} \tag{3.13}$$

where y is the output, due to a set of sources acting simultaneously, and y_1 is the output due to one source only of the set.
The knowledge of the number of sources can be deduced from the values assumed by $\gamma^2_{v_iv_j}$: it gives the indication on how many points are simultaneously excited. Indeed,

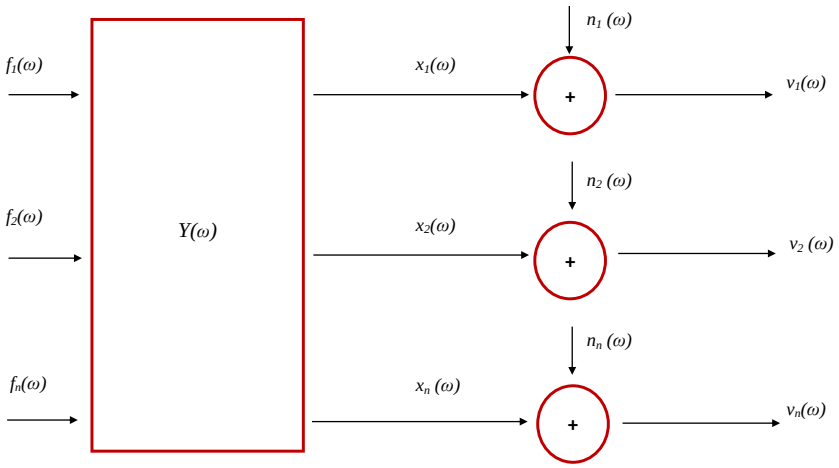

Figure 3.2: Multi Input/ Multi Output system

by considering its physical meaning, the coherence between two signals quantifies how these two signals are coherent with each other.
In a SIMO model, it is expected that the coherence between the velocities is close to one: in fact, all the velocities depend on the single applied load. For a MIMO model, when the loads are not correlated, the coherence between the velocities is less than the correspondent coherence of a SIMO model.
In fact, the responses depend on two or more different sources. Therefore, increasing the uncorrelated loads the values of the velocity coherence decreases proportionally to the number of the excited points.
The velocity coherence is computed by the following equation:

$$\gamma^2_{v_i v_j} = \frac{|S_{v_i v_j}|^2}{S_{v_i v_i} S_{v_j v_j}} \tag{3.14}$$

In order to evaluate how many forces are acting on the structure, first the coherence matrix is averaged on the whole frequencies range, $\bar{\gamma}^2_{vv}$. Each column of $\bar{\gamma}^2_{vv}$ is normalized to 1 by its mean value and Γ_{ij} is obtained. Then for each column of Γ_{ij} the standard deviation is computed and then the mean value of the result is calculated:

$$\begin{aligned} \Gamma_{ij} &= \bar{\gamma}^2_{v_i v_j} / E_i[\bar{\gamma}^2_{v_i v_j}] \\ N_{sources} &= E_i \left[\sqrt{E_j[(\Gamma_{ij} - \bar{\Gamma}_{ij})^2]} \right] \end{aligned} \tag{3.15}$$

The index $N_{sources}$ of equation (3.15) represents the percentage of how many forces are loading the structure. In fact, as shown later in the result section, the value assumed by $N_{sources}$ is close to 0.1 for one force and it is close to 0.2 for two forces.
Once the acting force number is identified, we proceed to identify their position. This procedure is inspired by the work of Fontul and Lage [28, 29], where the concept of transmissibility is used to identify the acting forces, and the work of Zhou [30], where the coherence function is applied to perform damage identification.
Consider a dummy forces distribution applied to all the considered measurement points. Each force is uncorrelated with the other forces and is constant on the chosen frequency range. The power spectral density of these forces distribution, $S_{\tilde{f}\tilde{f}}$, is a diagonal matrix with a constant value at each diagonal element. The cross spectral density between force and velocity is calculated [30] by the equation:

$$\mathbf{S}_{v\tilde{f}}(\omega) = \mathbf{Y}^{*}\mathbf{S}_{\tilde{f}\tilde{f}} \tag{3.16}$$

Then, the following ratio is calculated:

$$c_{v_j f_i} = \frac{|S_{v_j \tilde{f}_i}|^2}{S_{\tilde{f}_i \tilde{f}_i} \overline{S}_{v_j v_j}} \tag{3.17}$$

where $S_{v_j \tilde{f}_i}$ and $S_{\tilde{f}\tilde{f}}$ depend on the dummy forces distribution and $\overline{S}_{vv}$ is the PSD of the measured velocities.
Equation (3.17) is averaged on the whole frequency range as follows:

$$C_{v_j f_i} = \frac{1}{\Delta\omega} \int_{\omega_1}^{\omega_2} \frac{|S_{v_j \tilde{f}_i}|^2}{S_{\tilde{f}_i \tilde{f}_i} \overline{S}_{v_j v_j}} d\omega \tag{3.18}$$

The values of C_{vf} represent a coherence between the dummy forces and the measured responses due to the actual force. Since the dummy forces are applied to all the measurement points, the values assumed by the ratio of equation (3.18) is minimum in correspondence to the point excited by the actual force. This procedure allows to determine the force position.
After the identification of the force position, the amplitude of the PSD force is calculated by:

$$(S_{f_i f_i})_{id} = \frac{\overline{S}_{v_i v_i}}{|Y_{ii}|^2} \tag{3.19}$$

This procedure allows to reduce the error due to the solution of an inverse problem, because it avoids the intrinsic failing of the inversion of an ill-conditioning matrix. In the diagram of figure 3.3 the whole procedure is shown.

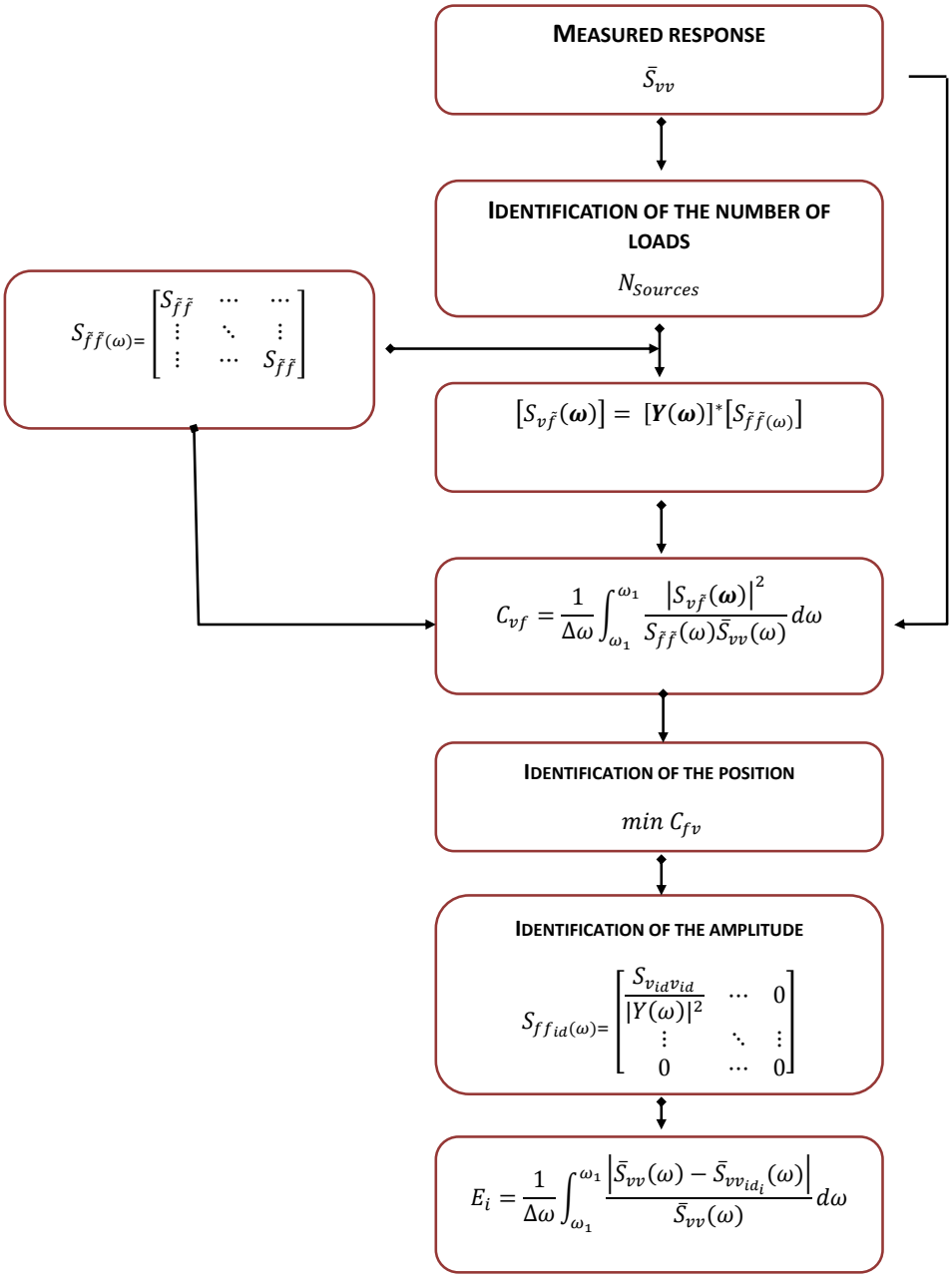

Figure 3.3: Diagram of the identification procedure

3.2 Single input/ multi output model

In this section, the procedure proposed in the previous section is applied to different models to verify the theoretical definitions and the related comments stated in the previous section. Single input/multi output (SIMO) models are discussed.
The structure used for the previous applications is considered (figure 3.4). It is excited

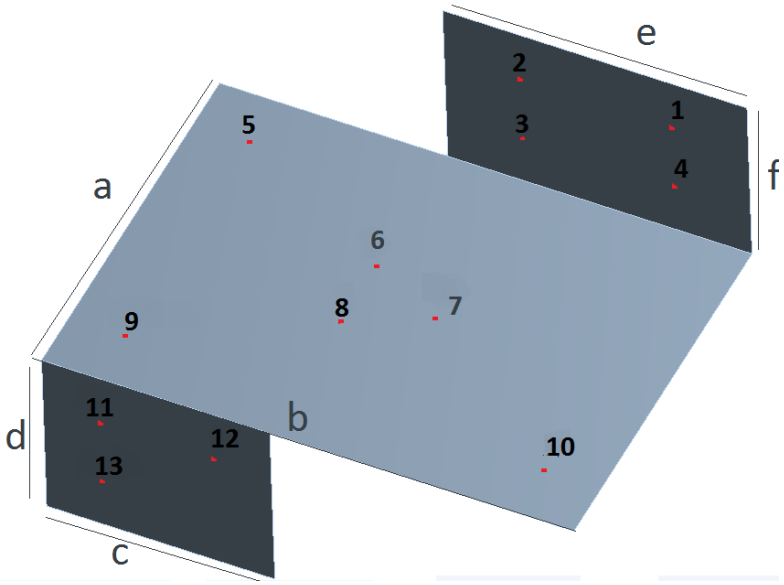

Figure 3.4: Test bed

by a non deterministic load (multi impulse excitation performed by hammer) 13 times, every time in correspondence of one of the chosen 13 points shown in figure 3.4. The acquisition is performed between 1 and 2500 Hz by a 16 channels acquisition system. By this measurement campaign the experimental FRF is calculated for the whole set of 13 points. The following applications, without loss of generality, are based on the same measurements used for the FRF calculation.

3.2.1 SIMO identification: whole measurement points set

For this first application the structure response is measured at each of the chosen 13 points by 13 accelerometers.
First the number of exciting forces is identified by equation (3.15). In table 3.1 the results obtained for $N_{sources}$ and the correspondent number of acting forces k are shown.

Table 3.1: SIMO identification: whole measurement points set. Number of excited points k

	$\mathbf{N_{sources}}$	k		$\mathbf{N_{sources}}$	k
Test 1	0,1	1	***Test 8***	0,1	1
Test 2	0,1	1	***Test 9***	0,1	1
Test 3	0,1	1	***Test 10***	0,1	1
Test 4	0,1	1	***Test 11***	0,1	1
Test 5	0,1	1	***Test 12***	0,1	1
Test 6	0,1	1	***Test 13***	0,1	1
Test 7	0,1	1			

Then the force position is identified by the C_{vf} factor. Figure 3.5 shows the $1/C_{vf}$ trends averaged on the whole frequency range. The reciprocal of C_{vf} is displayed, the maximum values of $1/C_{vf}$ it is more evident then the minimum values of C_{vf}. Each graph of the figure corresponds to the single test in which the excited point is indicated in the title of the graph.
Finally the PSD force is identified by equation (3.19). The results are shown in figure 3.6.
Both the results in figure 3.5 and in figure 3.6 show the ability of this procedure to correctly identify the external forces.
Consider the test case 4, where the point 4 is excited. Figure 3.7 shows the comparison between the actual S_{ff} and the S_{ff} of all the 13 points identified directly by equation (2.12). It is clear that this direct procedure does not allow to identify the location of the applied force, because the amplitude of the identified S_{ff} of each point when the point 4 is excited are quite similar. Furthermore the identified S_{ff} amplitude is very different with respect to the actual one.
This last comment is further confirmed by the comparison of the actual S_{ff}, the identified S_{ff} obtained by the procedure here proposed and the identified S_{ff} achieved by equation (2.12)(see figure 3.8).
Once established that the procedure proposed in this section gives better result then the procedure performed in the previous chapter, a further validation is performed by

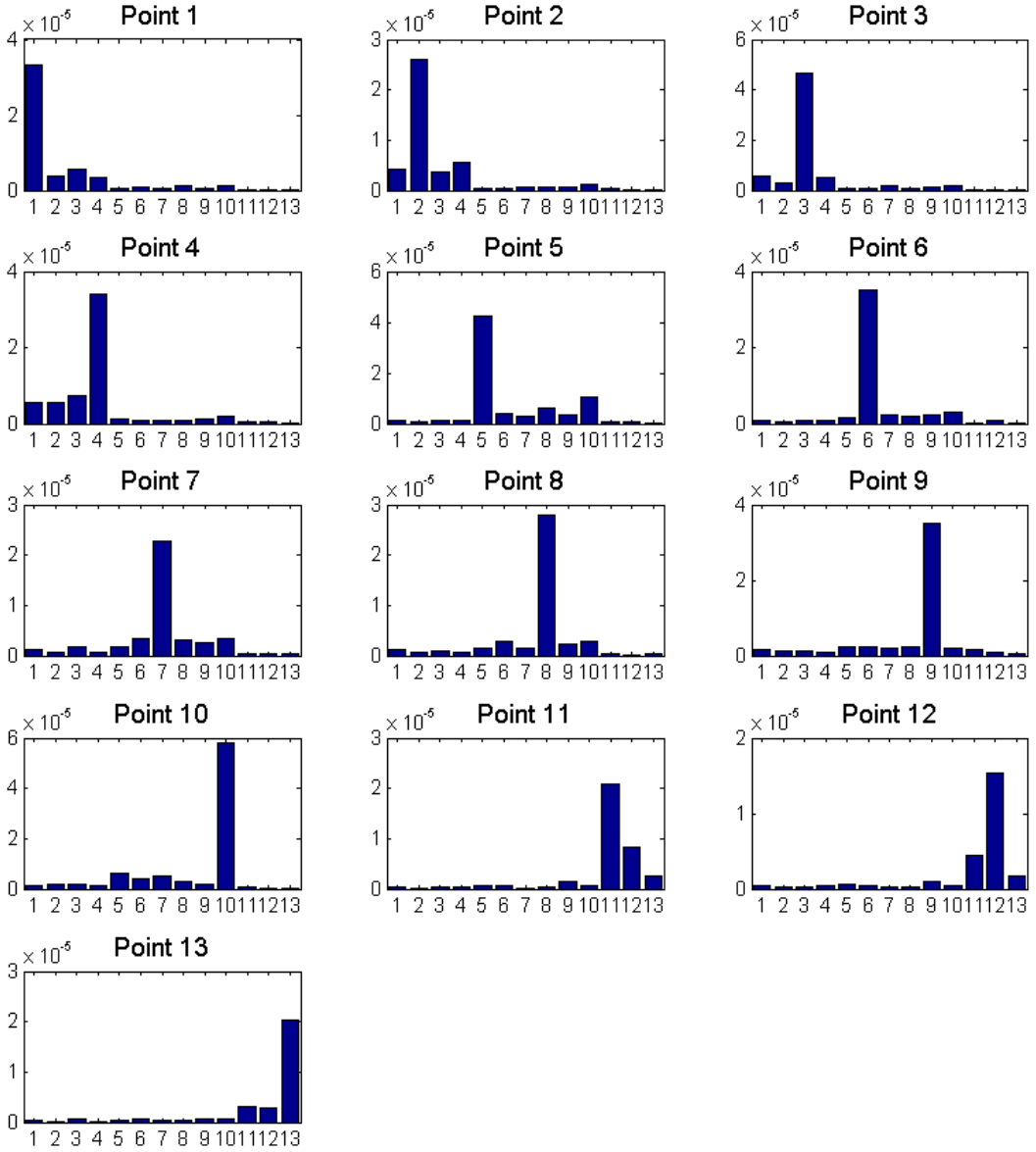

Figure 3.5: Single input/ multi output identification: whole measurement points set. $1/C_{vf}$ averaged on the whole frequency band

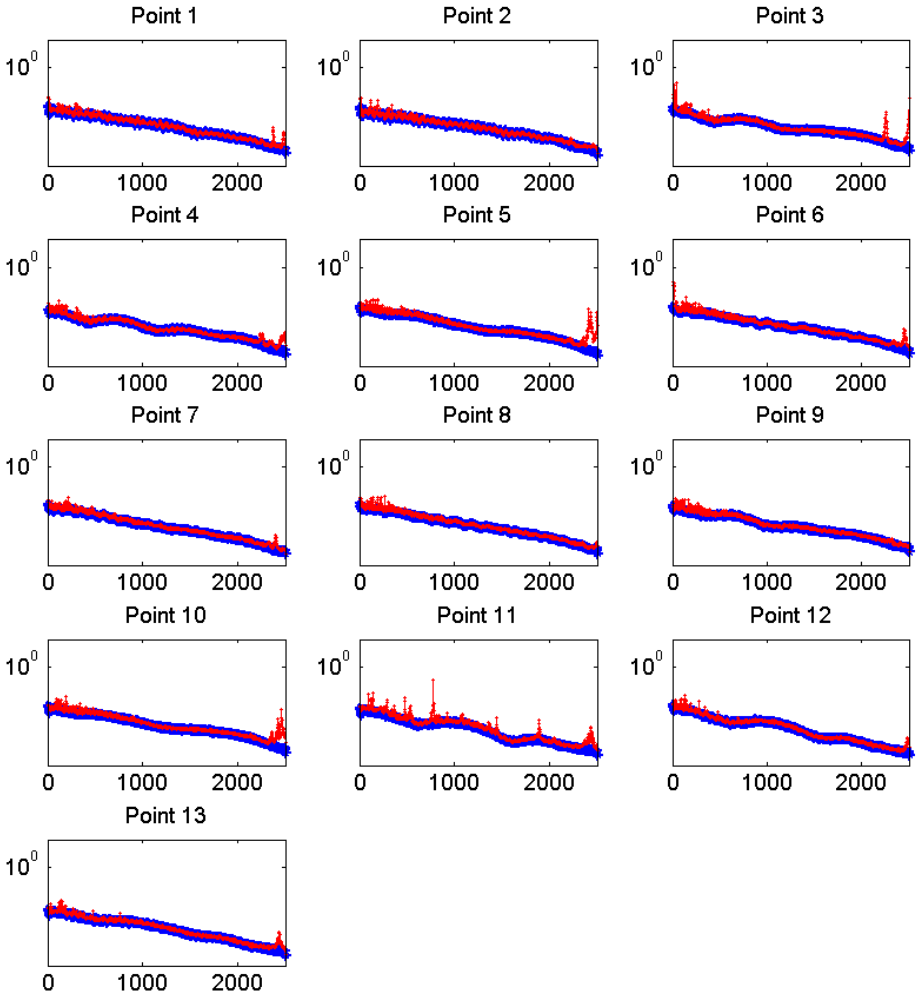

Figure 3.6: Single input/ multi output identification: whole measurement points set. Comparison between S_{ff}: actual PSD force ($-*-$), PSD force identified by equation (3.19)($-\mathbf{o}-$) and PSD force identified by equation by equation (2.12)($--$)

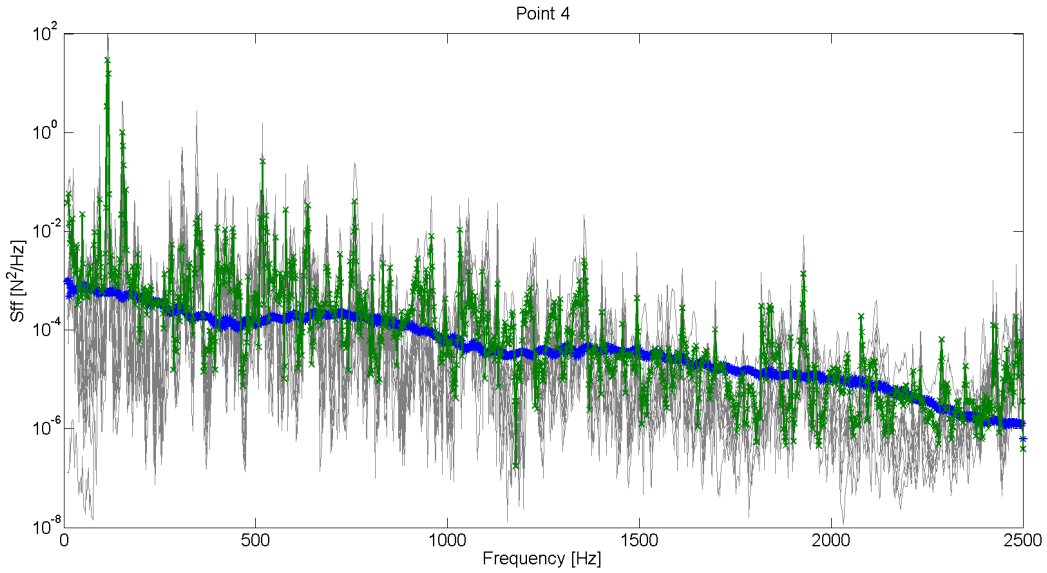

Figure 3.7: Single input/ multi output identification: whole measurement points set. Comparison between the actual PSD force S_{ff} $(-*-)$, the PSD force identified by equation (2.12) at the correct point$(-\mathbf{o}-)$ and the PSD force identified at the other points $(-)$for test 4.

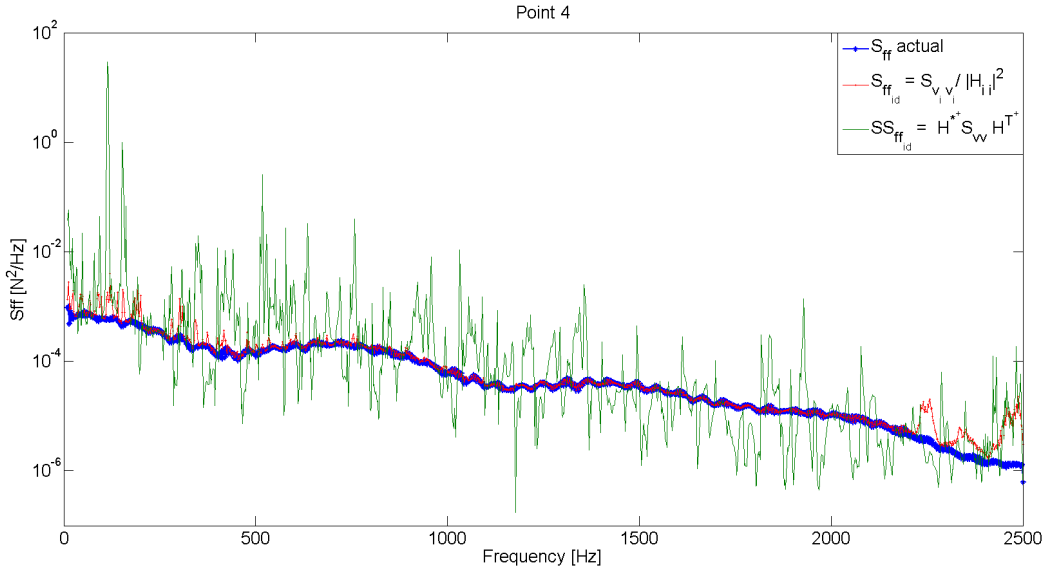

Figure 3.8: Single input/ multi output identification: whole measurement points set. Comparison between the actual PSD force S_{ff} $(-*-)$, the PSD force identified by equation (3.19)$(-\mathbf{o}-)$ and the PSD force identified by equation (2.12)$(--)$ at point 4

calculating the S_{vv} by equation (2.11) using the identified S_{ff}. Figure 3.9 shows that the measured S_{vv} and calculated S_{vv} match very well.

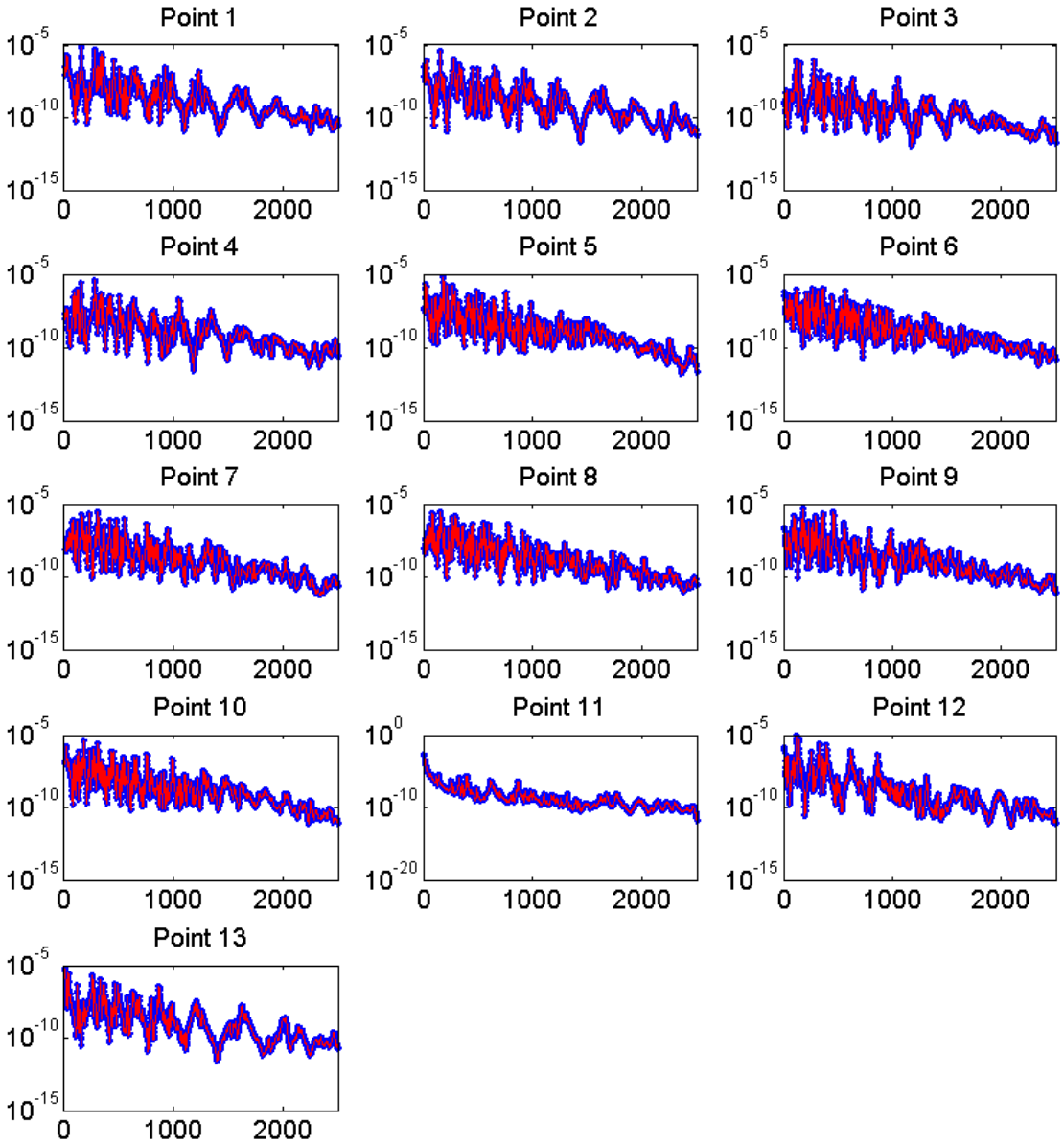

Figure 3.9: Single input/multi output identification: whole measurement points set. Comparison between the actual PSD velocity S_{vv} ($-*-$), the PSD velocity computed by PSD force identified by equation (3.19) ($-\mathbf{o}-$)

3.2.2 SIMO identification: reduced measurement points set

This test is the same of the previous section, but, in this case, the acquired points are a selection of 8 points chosen among the 13 points. The selected points are shown in table 3.2.

Table 3.2: Selected measurement points

measurement points							
2	4	5	6	8	10	11	12

The FRF of the structure is known at 13 points, while the velocities, when the unknown force acts, are measured only on a reduced set of points. This test allows to verify the ability of the proposed procedure when the measurement points do not coincide with excited points. The experimental FRF matrix is always known in correspondence of the exciting points.
First the number of excitations is identified by equation (3.15). The results are shown in table 3.3

Table 3.3: SIMO identification: reduced measurement points set. Number of excited points k

	$\mathbf{N_{sources}}$	k		$\mathbf{N_{sources}}$	k
Test 1	0,1	1	***Test 8***	0,1	1
Test 2	0,1	1	***Test 9***	0,1	1
Test 3	0,1	1	***Test 10***	0,1	1
Test 4	0,1	1	***Test 11***	0,1	1
Test 5	0,1	1	***Test 12***	0,1	1
Test 6	0,1	1	***Test 13***	0,1	1
Test 7	0,1	1			

Then the C_{vf} factor is calculated to identify the force position, but, in this case, the obtained results are approximated, because the point where C_{vf} is minimum can or can not coincide with the excited point. So C_{vf} is calculated by equation (3.18) over the 8 points and the point corresponding to the C_{vf} minimum value is selected. Now we must

decide if this point is actually excited.
In any case the amplitude of PSD force is calculated at the chosen point by equation (3.19). This force is imposed one by one at each of the 13 points and the PSD velocity is calculated for the 13 tests at each point by equation (2.11).
For each test the relative error between the PSD of the measured response and the numerical one is computed and it is averaged over the whole frequency range:

$$E_i = \frac{1}{\Delta\omega} \int_{\omega_1}^{\omega_2} \frac{\overline{S}_{vv}(\omega) - S_{vv_{id_i}}(\omega)}{\overline{S}_{vv}} d\omega \tag{3.20}$$

The minimum value of E_i identifies the excited point. One more time the amplitude of the PSD force is calculated by equation (2.12) at this new point. Figure 3.10 shows the comparison between the actual force PSD, the PSD force here identified and the PSD force identified by equation (2.12). This new approach gives better results than the direct inversion of equation (2.11).
The results obtained from the minimization of the error of equation 3.20 provide the position and the amplitude of the resultant pseudo forces that give the dynamic responses nearest to the measured ones. To improve the confidence of these results it should be necessary the knowledge of the measured response in the neighbourhood of the position identified by the minimization.
Figure 3.11 shows the comparison of the force PSD, the actual, the identified by the proposed procedure and identified by the inversion of equation (2.11), computed over constant bandwidth of 100 Hz. The identified force matches the measured force for each drive point, and obviously the matching is better in correspondence of the measured points.
By using the force already identified the PSD velocity is calculated and compared in figure 3.12 with the PSD of the measured velocity. The results are not good as those of the previous section, but, considering the increase of uncertainty in the identification procedure, they can be considered acceptable anyway.

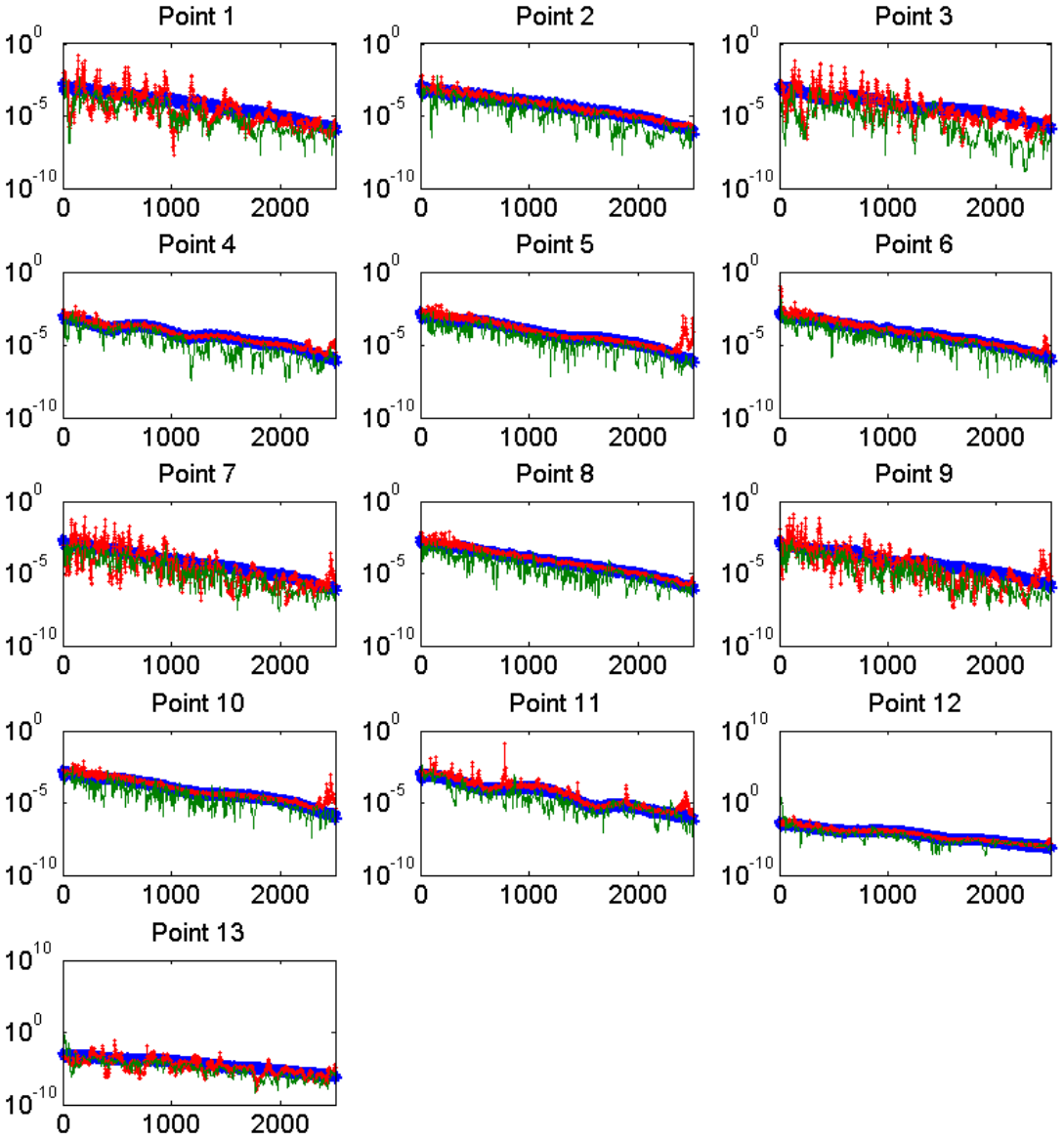

Figure 3.10: Single input/ multi output identification: reduced measurement points set. Comparison between the actual PSD force S_{ff} ($-*-$), the PSD force identified by equation (3.19)($-\mathbf{o}-$), the PSD force identified by equation (2.12)(-)

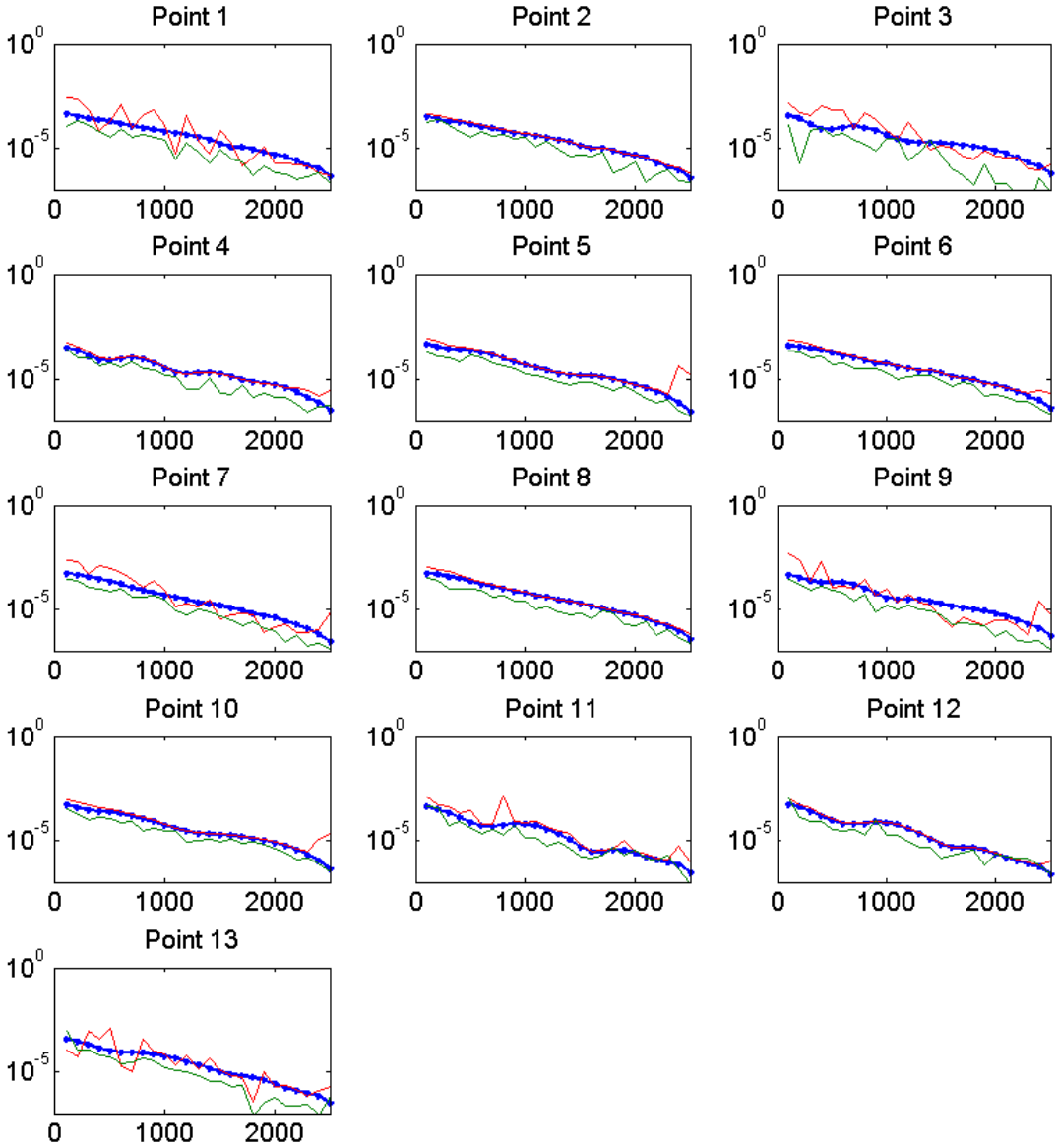

Figure 3.11: Single input/ multi output identification: reduced measurement points set. Comparison between the actual PSD force ($-*-$), the PSD force identified by equation (3.19) ($-\mathbf{o}-$)and the PSD force identified by equation (2.12)(-)

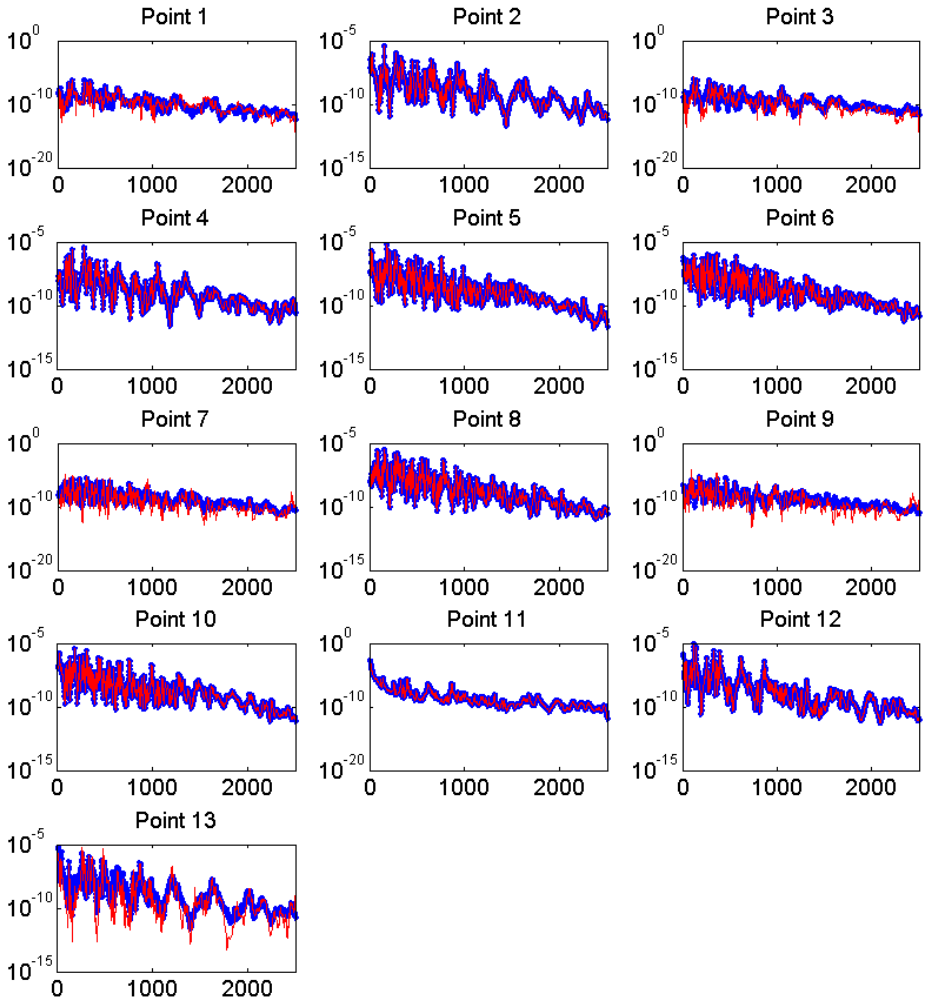

Figure 3.12: Single input/ multi output identification: reduced measurement points set. Comparison between the actual PSD velocity S_{vv} $(-*-)$ and the PSD velocity computed by the PSD force identified by equation (3.19) $(-\mathbf{o}-)$

3.3 Multi input/ multi output model

In this section Multi Input/ Multi Output models are considered. The procedure presented in this chapter is adopted for this kind of input-output model and it is verified if the method is as effective as for the SIMO model.

3.3.1 MIMO identification: whole measurement points set

The structure is excited by two uncorrelated forces generated by two different hammer multi impulse in correspondence of two points of the structure. The response is acquired in correspondence of the whole set of 13 points. As in the SIMO test, the first step of the identification is the evaluation of the number k of applied loads by equation (3.15). The results obtained for the two tests are shown in table 3.4.

Table 3.4: MIMO identification: whole measurement points set. Number of excited points k

	$\mathbf{N_{sources}}$	k
Test 1	0.2	2
Test 2	0.2	2

Then the values of C_{vf} is computed as shown in section 3.2.1.
In this instance, the k minimum values are selected from the organised vector of C_{vf}. As shown in figure 3.13, they correspond to the couple (1,4) in the first test and to the couple (1,2) in the second one. The amplitude of the force is computed, in correspondence of

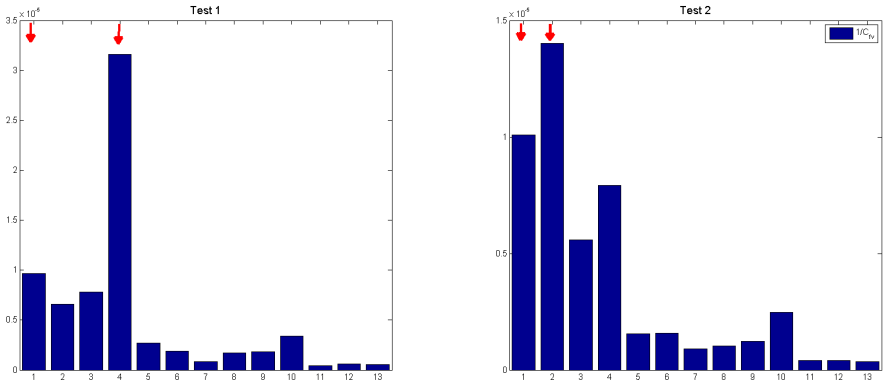

Figure 3.13: Multi input/ multi output identification: whole measurement points set. $1/C_{vf}$ averaged on the whole frequency band

the excited k points by equation (3.19).
Then for a further validation of the obtained results, the forces now calculated are applied at all the combinations $C_{n_{tot},k}$ of points.
$C_{n_{tot},k}$ is the combination of the excited k points on the whole set of n measurement points. The PSD of the velocity is calculated by equation (2.11) for each combination of excitations.
In figures 3.14 and 3.15 the results obtained by two different combinations of drive points are shown. In the first experiment, the excited points are the couple (1,4) and in the second experiment the couple (1,2).
Figure 3.14 shows the comparison between the applied load and the identified ones. Also in this case there is a good correspondence in both considered test.

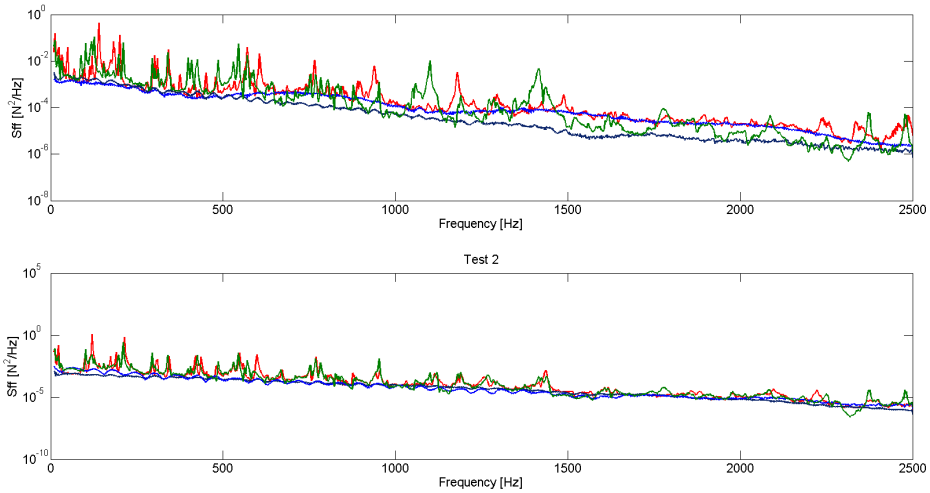

Figure 3.14: Multi input/ multi output identification: whole measurement points set. Comparison between the actual forces PSD S_{ff_1} (*blue*), S_{ff_2} (black) and the forces PSD identified $S_{ff_{id_1}}$ (red) and $S_{ff_{id_2}}$ (green)

Figure 3.15 shows the comparison between the measured PSD velocity and the PSD velocity computed by equation (2.11) using identified forces; also in this case there is a good agreement between measured and identified PSDs.

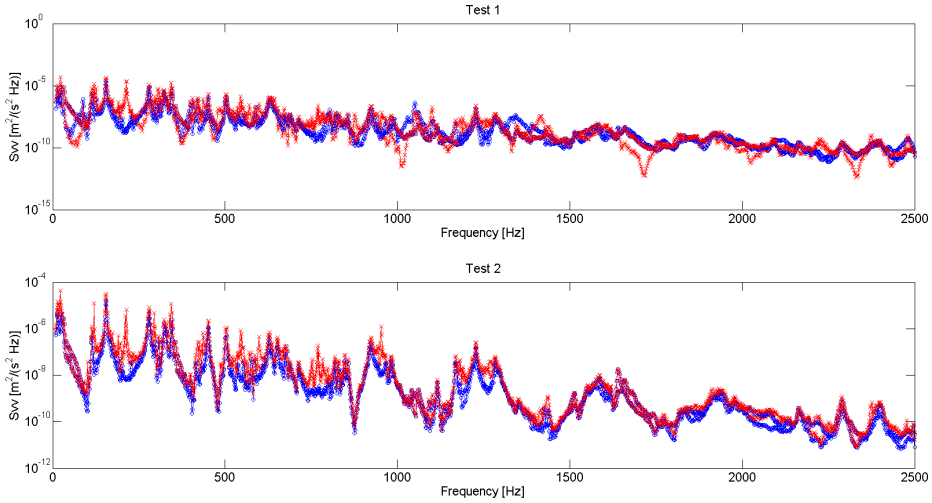

Figure 3.15: Multi input/ multi output identification: whole measurement points set. Comparison between the actual PSD velocity S_{vv} $(-\mathbf{o}-)$and the PSD velocity identified by equation (3.19)$(- \times -)$

3.3.2 MIMO identification: reduced measurement points set

As tested for the SIMO model, the identification of two or more uncorrelated forces is performed also considering a reduced set of measurement points. The number of selected points is the same of section 3.2.2, shown in table 3.2. In this case in the rounding of the value computed through equation (3.15) is assumed at -10% tolerance due to the increasing of the mean value of the coherence resulting from the use of the reduced sets. The results obtained for the two tests are reported in table 3.5.

Table 3.5: MIMO identification: reduced measurement points set. Number of excited points k

	$\mathbf{N_{sources}}$	k
Test 1	0.2	2
Test 2	0.2	2

The reduced number of measurement points together with a multi input excitation make less efficient the use of C_{vf}. Indeed, in this case, the use of the reference forces computed in correspondence of the points given by the minimum values of C_{vf}, does not provide the expected results. Therefore, the reference forces are computed from equation (2.14) and they are applied to all the combination of $C_{n_{tot},k}$ points. Then, for each combination, the error of equation (3.20) is computed; the minimum values of the error gives the

combination of the excited points. Figure 3.16 shows the values of the errors for the two considered cases in which the couple $(1, 4)$ and $(1, 2)$ are excited. The minimum value of the first test is in correspondence of the third combination that actually matches the couple $(1, 4)$; for the second test it is in correspondence of the first combination that matches the couple $(1, 2)$.

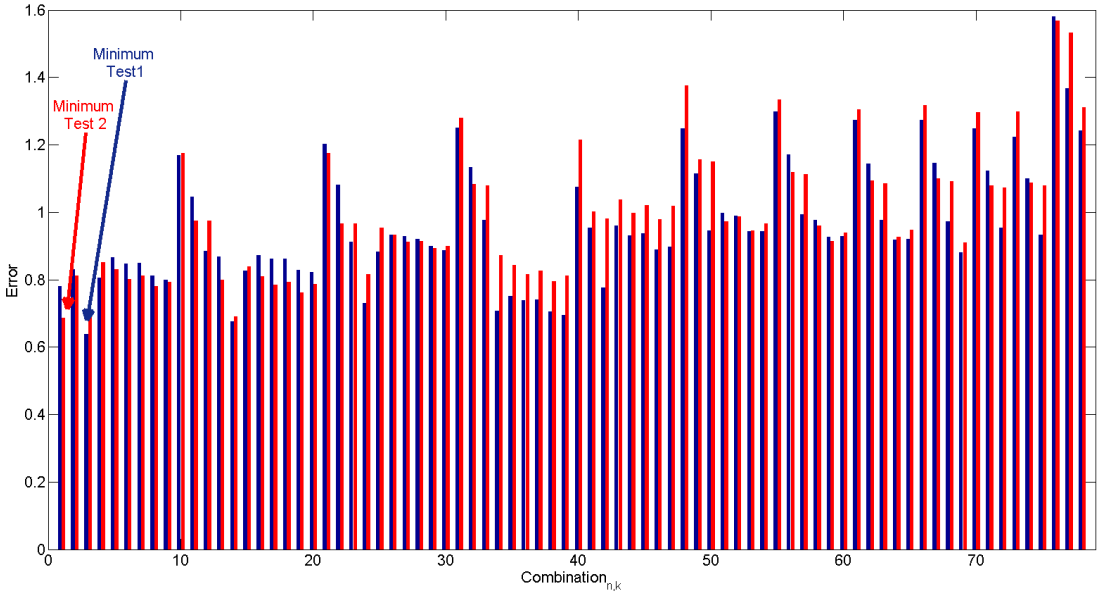

Figure 3.16: Multi input/ multi output identification: reduced measurement points set. Error computed for each configuration of points in the first test (blue) and in the second test (red)

It must be noticed that, as in section 3.2.2, the minimum values of the C_{vf} identify, among the points of the reduced set, those closest to the excited points.
Figures 3.17 and 3.18 show the good agreement of the identified forces with the actual ones, and the comparison between the PSD velocity for the two considered tests respectively.

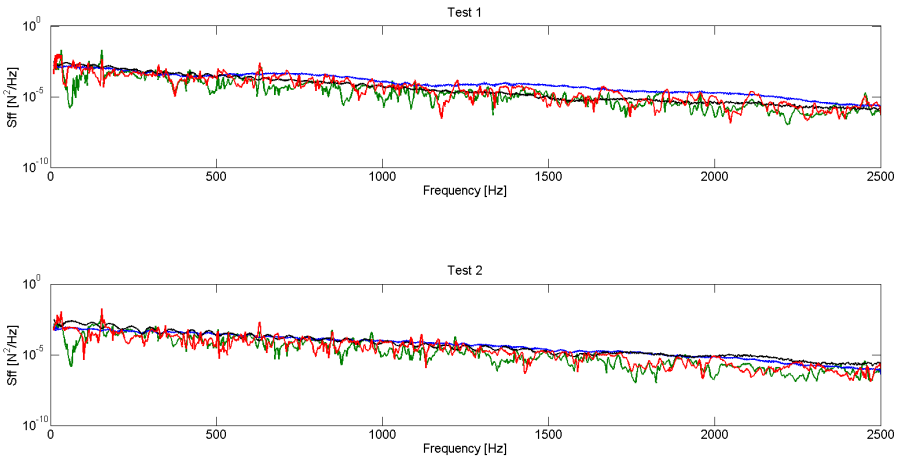

Figure 3.17: Multi input/ multi output identification: reduced measurement points set. Comparison between the actual PSD velocity S_{ff_1} (*blue*), S_{ff_2} (black) and the forces PSD identified $S_{ff_{id_1}}$ (red) and $S_{ff_{id_2}}$ (green)

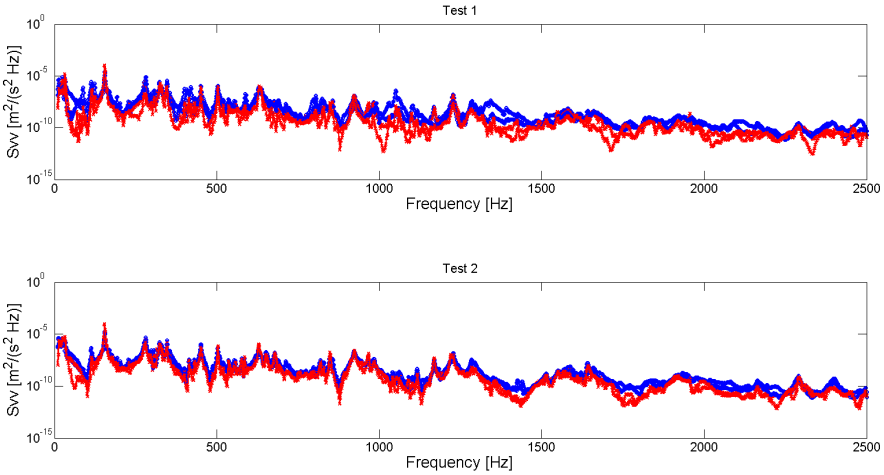

Figure 3.18: Multi input/ multi output test. Comparison between actual PSD velocity S_{vv} ($-\mathbf{o}-$)and the PSD velocity computed by the PSD force identified by equation (3.19) ($-\times-$)

Conclusions In this chapter an alternative approach is proposed, to identify random loads acting on a structure. The procedure is carried out in three steps: first the number of acting forces is established, then the position and the amplitude are identified.
Finally the goodness of the identified load is evaluated by the computation of the PSD velocity relative error.
The number of sources is established by an index based on the velocity coherence.
The identification of the position of the applied loads is performed by the C_{vf} index, it is computed as a virtual coherence between a dummy load, applied numerically to the structure, and the actual velocity. The results show that the proposed index allows to identify the correct position of the applied loads for both single input and multi input tests. Once the position is identified, the amplitude of the load is computed by equation (3.19); the use of this formulation reduces the effect of the ill-conditioning of the problem, indeed the inversion of the FRF matrix is not required.
For both the considered cases (SIMO and MIMO), the identification is also obtained with a reduced measurement points set, in order to evaluate the limit of the proposed procedure: the measurement points could either be or not be drive points.
The C_{vf} index can be computed only in correspondence of the measurement points. Indeed, the knowledge of the PSD velocity is required. In the single input/ multi output model the index gives good results, the amplitude of the reference force is calculated in correspondence of the point selected by the index. This allows to excite numerically the structure to calculate the relative error between the actual PSD velocity and that computed by the identified forces. The minimum value of the error corresponds to the position of the identified force.
In the case of multi input/multi output model the use of the index does not give good results. The knowledge of the number of applied loads allows to consider all the exciting points combination, then a load of amplitude computed by the inversion of classical random loads is numerically applied to the structure and the correct position is given by the minimization of the relative error computed for each combination. This procedure is obviously expansive in terms of computational costs.

CHAPTER
FOUR

IDENTIFICATION BY USING ENERGY BASED MODEL

The solution of high frequency problems can be performed by Energy Based (EB) models, that allow to bypass the ill-conditioning of the FRF matrix.
One of the most prominent technique that allows to predict the energy stored into mechanical systems by a power exchanged model is the Statistical Energy Analysis (SEA) [31–37]. The difference between a generic EB model and SEA is the basic hypothesis of SEA. In fact SEA and EB models are both based on a power balance which relates, by linear algebraic equations, the power injected into a mechanical system and the energy stored into the same system. Whereas the coefficient matrix of SEA model must follow some hypothesis, on the contrary this condition must not be respected by a generic EB model.
The results shown in the third chapter and in the second part of the second chapter suggest that the energetic approach could be a good way to solve the identification problem in the instance of not deterministic loads. Hence, in this chapter a procedure, based on energetic method, to identify first the injected power and then the load spectrum of the applied loads, in operative condition is proposed.
The procedure is performed in two steps [37]: the first step is focused on the identification of the coefficients of an EB model of the structure by using the Power Injection Method (PIM). This technique allows to obtain the EB model parameters of the structure by experimental tests. The second step is the identification of the power injected by using the identified model and solving the "*inverse problem*" of the EB model. It is useful precise that the identified model is not properly a SEA model, indeed, some particular hypotheses of Statistical Energy Analysis are not satisfied.

4.1 Theoretical background of Statistical Energy Analysis

A high frequency problem is defined when a characteristic dimension of the studied structure is much larger than the propagating wavelength. Classical techniques, as FEM

and BEM allowing to solve low-medium frequency problems, are not appropriate to approach this kind of problem for several reasons. First, the use of classical techniques imply that when increasing the modal density, the numbers of required DoFs grow up: this entails high computational costs. Moreover, also when the solution can be find, it is necessary to consider that at high frequency the higher order eigenvalues are more sensitive to uncertainties of the geometry, the boundary condition and the material properties. This implies that an increase of the modal density prevents to find the correct solution. These reasons lead to suggest that an energetic method based on exchanged power balance between mechanical subsystems could be more efficient then the classical methods based on the force balance. The power balance is true at all frequencies anyway. The challenge is to find a model that allows to obtain the relation between the power exchanged and the energy stored in each subsystem, to obtain finally a linear system that links the injected power to the energy stored trough a coefficient matrix. Therefore in the solution of high frequency problem the Statistical Energy Analysis, when some particular hypothesis are satisfied, allows to obtain an energetic model based on linear equation that gives the high frequency problem solution.
The greatest advantage of the use of this techniques is the reduction of the number of DoF. SEA in fact uses spatial and frequency averages on suitable subsystems that allow to reduce the dimension of the problem and the difficulties related to the increase of the ill-conditioning in correspondence of the resonances.
Consider the 2 DoF system in figure 4.1.

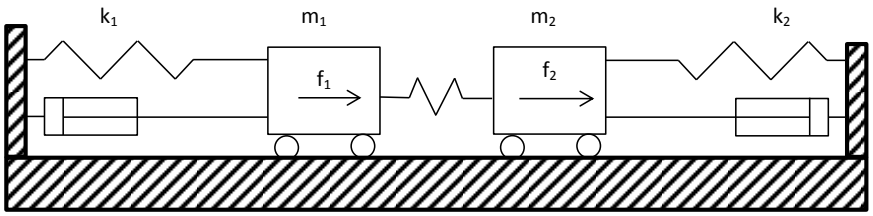

Figure 4.1: Two Degrees of Freedom system

The equations of the force balance are:

$$\begin{cases} m_1\ddot{x}_1 + c_1\dot{x}_1 + (k_1 + k_c)x_1 = f_1 + k_c x_2 \\ m_2\ddot{x}_2 + c_2\dot{x}_2 + (k_2 + k_c)x_2 = f_2 + k_c x_1 \end{cases} \tag{4.1}$$

By multiplying the first equation by $\dot{x}_1$ and by integrating on the period T, the equation

of the power balance on m_1 is achieved [38]:

$$\frac{1}{T}\int_0^T \ddot{x}_1\dot{x}_1 dt + \frac{1}{T}\int_0^T \frac{c_1}{m_1}\dot{x}_1\dot{x}_1\ dt + \frac{1}{T}\int_0^T \frac{k_1+k_c}{m_1}x_1\dot{x}_1\ dt = \\ = \frac{1}{T}\int_0^T \frac{k_c}{m_1}x_2\dot{x}_1\ dt + \frac{1}{T}\int_0^T f_1\dot{x}_1 dt \quad (4.2)$$

Notice that in the steady state the first and the third integral of equation (4.2) are null, so that the equation becomes:

$$\frac{1}{T}\int_0^T f_1(t)\dot{x}_1(t)\ dt = \frac{1}{T}\int_0^T \frac{c_1}{m_1}\dot{x}_1\dot{x}_1\ dt - \frac{1}{T}\int_0^T \frac{k_c}{m_1}x_2\dot{x}_1\ dt \quad (4.3)$$

Nevertheless an equation equivalent to equation (4.3) can be written for the power balance on m_2 by multiplying the second equation of (4.1) for $\dot{x}_2$. The physical meaning of each term of equation (4.3) is:

$\frac{1}{T}\int_0^T f_1(t)\dot{x}_1(t)\ dt$	the power injected
$\frac{1}{T}\int_0^T \frac{c_1}{m_1}\dot{x}_1\dot{x}_1\ dt$	the power losses
$\frac{1}{T}\int_0^T \frac{k_c}{m_1}x_2\dot{x}_1\ dt$	the power exchanged

Therefore, for this two DoF system, it can be written:

$$\begin{array}{lcll} P_{injected_1} & = & P_{lost_1} & + & P_{exchanged_{1,2}} \\ P_{injected_2} & = & P_{lost_2} & + & P_{exchanged_{2,1}} \end{array} \quad (4.4)$$

Note that the power lost is proportional to the total energy of each mass and the power exchanged is proportional to the difference between the total energies of the two masses. By considering each DoF as a subsystem, the system of figure 4.1 can be displayed by the diagram of figure 4.2.
For a M DoF system it is possible to consider a group of DoFs as a subsystem. In this case the energy balance becomes:

$$P_{i,inj} = P_{i,lost} + \sum_{j\neq i}^{N} P_{i,j} - \sum_{j\neq i}^{N} P_{j,i} \quad (4.5)$$

where i and j are the subsystems indices and N is the number of subsystems.
In Statistical Energy Analysis it is posed that, under some particular hypotheses [39], the energy flow between two subsystems is proportional to the difference of the energy stored in each subsystem. This assumption is close to truth when:

- all the modes of the subsystem are similar;

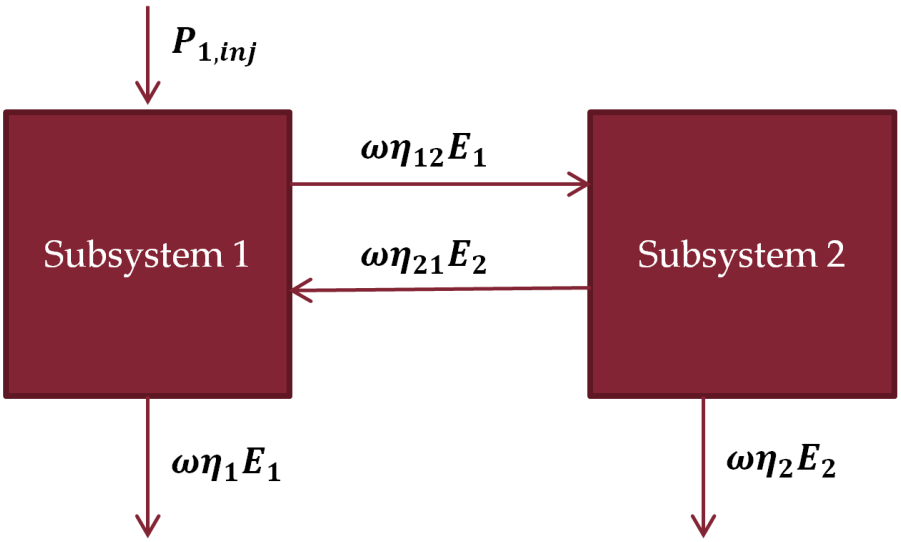

Figure 4.2: Two subsystems SEA model

- the subsystems couplings are conservative;
- the eigenfrequencies are uniformly probable in a frequency band;
- the force exciting the subsystems are random and uncorrelated;
- the interactions between the subsystem are weak.

Therefore, the power exchanged between subsystem i and subsystem j is:

$$P_{i,j} = \omega\eta_{i,j}\left(\frac{E_i}{n_i} - \frac{E_j}{n_j}\right) \tag{4.6}$$

where n_i and n_j are the modal density of subsystems (the number of modes over the bandwidth), η_{ij} is the Coupling Loss Factor (CLF) of the junction between subsystems i and j, ω is the central frequency of the considered band and E is the energy stored in each subsystem. The power lost is:

$$P_{i,lost} = \omega\eta_i E_i \tag{4.7}$$

where η_i are the Internal Loss Factors (ILF).
Therefore the energy balance equations for N coupled subsystems are [26, 33, 34]:

$$P_{i,inj} = \omega\,\eta_i\,E_i + \omega\sum_{j=1,j\neq i}^{N}(\eta_{ij}\,E_i - \eta_{ji}\,E_j) \quad i = 1,\ldots,N \tag{4.8}$$

Equation (4.8) can be written as follow:

$$\begin{bmatrix} P_1 \\ \dots \\ \dots \\ P_m \end{bmatrix} = \omega \left\{ \begin{bmatrix} \eta_{11} & 0 & \dots & 0 \\ 0 & \dots & \dots & \dots \\ \dots & \dots & \dots & \dots \\ 0 & \dots & \dots & \eta_{mm} \end{bmatrix} + \begin{bmatrix} \sum_{j=1, j\neq 1}^{N} \eta_{1j} & -\eta_{21} & \dots & -\eta_{m1} \\ -\eta_{12} & \dots & \dots & \dots \\ \dots & \dots & \dots & \dots \\ -\eta_{1m} & \dots & \dots & \sum_{j=1, j\neq 1}^{N} \eta_{mj} \end{bmatrix} \right\} \begin{bmatrix} E_1 \\ \dots \\ \dots \\ E_m \end{bmatrix} \tag{4.9}$$

or, synthetically:

$$\mathbf{P} = \omega \left(\mathbf{A} + \mathbf{C} \right) \mathbf{E} \tag{4.10}$$

The sum of $\mathbf{A}$ and $\mathbf{C}$ can be expressed by the matrix $\boldsymbol{\eta}$:

$$\mathbf{P} = \omega \, \boldsymbol{\eta} \, \mathbf{E}. \tag{4.11}$$

Focusing on equation (4.8), it is interesting to notice that, to obtain the energy from the knowledge of the injected power in the classical SEA problem, it is necessary to invert the matrix $\boldsymbol{\eta}$. On the contrary, in this case the scope of the analysis is to evaluate the injected power starting from the knowledge of the energy stored in each subsystem. Therefore the force identification problem is a *direct problem*, where no matrix inversion is required and the ill-conditioning is avoided.

4.2 Power Injection Method

The presented procedure is an identification of external load based on an EB model. Therefore the model parameters of the structure, CLFs and ILFs, must be known. The values of CLFs and ILFs can be obtained by numerical computation through theoretical relationships or experimental techniques as the Power Injection Method [31–33,40]. Since the scope of the proposed methodology is the load identification, the procedure is already an operative procedure. Therefore rather than to calculate the theoretical parameters and then to update the model, it is better to identify directly the CLFs and ILFs by PIM. This benefit must be weighed against the cost due to the inversion of the energy matrix that proposes again the ill-conditioning problem.
The identification of SEA parameters by PIM implies that some independent experiments must be performed on the structure. In each experiment one of the subsystems is excited by an external known load and the response of the structure in correspondence of all subsystems is measured. Then, by the knowledge of the applied forces and of the responses, the total energy stored in each subsystem and the power injected are computed. Therefore, the described procedures need one independent experiment for each subsystem. Considering each experiment and equation (4.11), for N subsystems

the following equation are written:

$$\begin{bmatrix} P_1 \\ 0 \\ ... \\ 0 \end{bmatrix} = \omega\eta \begin{bmatrix} E_{11} \\ ... \\ ... \\ E_{n1} \end{bmatrix} ; \begin{bmatrix} 0 \\ P_2 \\ ... \\ 0 \end{bmatrix} = \omega\eta \begin{bmatrix} E_{12} \\ ... \\ ... \\ E_{n2} \end{bmatrix} ; ...; \begin{bmatrix} 0 \\ ... \\ 0 \\ P_n \end{bmatrix} = \omega\eta \begin{bmatrix} E_{1n} \\ ... \\ ... \\ E_{nn} \end{bmatrix} \tag{4.12}$$

where E_{nj} indicates the energy of subsystem n when the subsystem j is excited. Equation (4.12) can be collected together in order to write the following equation:

$$\begin{bmatrix} P_1 & ... & 0 \\ ... & ... & ... \\ ... & ... & ... \\ 0 & ... & P_m \end{bmatrix} = \omega \begin{bmatrix} \eta_{11} + \sum_{j=1,j\neq 1}^{N} \eta_{1j} & -\eta_{21} & ... & -\eta_{m1} \\ -\eta_{12} & ... & ... & ... \\ ... & ... & ... & ... \\ -\eta_{1m} & ... & ... & \eta_{mm} + \sum_{j=1,j\neq 1}^{N} \eta_{mj} \end{bmatrix} \begin{bmatrix} E_{11} & ... & E_{1m} \\ ... & ... & ... \\ ... & ... & ... \\ E_{m1} & ... & E_{mm} \end{bmatrix} \tag{4.13}$$

The CLFs and the ILFs can be identified by the inversion of the energy matrix:

$$\begin{bmatrix} \eta_{11} + \sum_{j=1,j\neq 1}^{N} \eta_{1j} & -\eta_{21} & ... & -\eta_{m1} \\ -\eta_{12} & ... & ... & ... \\ ... & ... & ... & ... \\ -\eta_{1m} & ... & ... & \eta_{mm} + \sum_{j=1,j\neq 1}^{N} \eta_{mj} \end{bmatrix} = \frac{1}{\omega} \begin{bmatrix} E_{11} & ... & E_{1m} \\ ... & ... & ... \\ ... & ... & ... \\ E_{m1} & ... & E_{mm} \end{bmatrix}^{-1} \begin{bmatrix} P_1 & ... & 0 \\ ... & ... & ... \\ ... & ... & ... \\ 0 & ... & P_m \end{bmatrix} \tag{4.14}$$

By mathematical manipulation equation (4.14) can be rewritten so that CLFs and ILFs are collected in a vector. The following equation shows the algorithm for three coupled subsystems:

$$\begin{bmatrix} \eta_1 \\ \eta_{12} \\ \eta_{13} \\ \eta_{21} \\ \eta_2 \\ \eta_{23} \\ \eta_{31} \\ \eta_{32} \\ \eta_3 \end{bmatrix} = \begin{bmatrix} E_{11} & E_{11} & E_{11} & -E_{21} & 0 & 0 & -E_{31} & 0 & 0 \\ 0 & -E_{11} & 0 & E_{21} & E_{21} & E_{21} & 0 & -E_{31} & 0 \\ 0 & 0 & -E_1 1 & 0 & 0 & -E_{21} & E_{31} & E_{31} & E_{31} \\ E_{12} & E_{12} & E_{12} & -E_{22} & 0 & 0 & -E_{32} & 0 & 0 \\ 0 & -E_{12} & 0 & E_{22} & E_{22} & E_{22} & 0 & -E_{32} & 0 \\ 0 & 0 & -E_1 2 & 0 & 0 & -E_{22} & E_{32} & E_{32} & E_{32} \\ E_{13} & E_{13} & E_{13} & -E_{23} & 0 & 0 & -E_{33} & 0 & 0 \\ 0 & -E_{13} & 0 & E_{23} & E_{23} & E_{23} & 0 & -E_{33} & 0 \\ 0 & 0 & -E_1 3 & 0 & 0 & -E_{23} & E_{33} & E_{33} & E_{33} \end{bmatrix}^{-1} \begin{bmatrix} P_1 \\ 0 \\ 0 \\ 0 \\ P_2 \\ 0 \\ 0 \\ 0 \\ P_3 \end{bmatrix} \tag{4.15}$$

Since the estimation of the energy in equations (4.14) and (4.15) and of the power injected is performed by experimental measurements, that are necessarily affected by noise, and since both proposed procedures imply the inversion of the energy matrix it is necessary to tackle the ill-conditioning of the energy matrix. Whit regard to this problem it must be considered that the EB approach involves the use of energy and injected power averaged on each subsystem. Therefore, whatever the number of subsystems that are assembled in the model, their number is lower than the typical number of DoFs of a FRF matrix. The classical approach to the reduction of ill-conditioning, as the regularisation techniques, is based on the suppression of the information that amplify the error of the data in the solution (see chapter 2). In this case a complete information are needed to carry out the model parameters, thus the ill-conditioning reduction approach is not recommended. Hence, instead of a direct approach to the ill-conditioning, a method less sensitive to the noise in the data has been sought; with this purpose the two techniques proposed in equations (4.14) and (4.15) are tested. In fact, even if these equations are theoretically equivalent, the inverse problems can differ due to the different ill-conditioning of the energy matrices.
The energy of subsystem i can be carried out by the the following equation:

$$E_{i,k} = \frac{\rho h}{N_{sub}} \sum_{j=1}^{N_{sub}} \Delta S_j \int_{\omega_1}^{\omega_2} S_{v_j v_{j\,i,k}} d\omega \tag{4.16}$$

where N_{sub} is the number of the measurement points for each subsystem i, m_j is the mass assigned to each measurement point and $S_{v_{ij,k} v_{ij,k}}$ [25] is the velocity of the measurement point j of the subsystem i when the subsystem k is excited. The power injected into subsystem i is computed by the knowledge of the cross spectral density between the applied force and the velocity measured at the drive point j by the following relationship:

$$P_{inj,i} = \frac{1}{N_{sub}} \sum_{j=1}^{N_{sub}} Re \left\{ \int_{\omega_1}^{\omega_2} S_{f_j v_{j\,i,k}} d\omega \right\} \tag{4.17}$$

4.3 Identification of the injected power

Once CLFs and ILFs are identified by PIM, the model is completely fixed. Then it is possible to proceed to identify the injected power. In operative condition, when the force that must be identified acts, the response of the structure on each subsystem is acquired. The energy at each subsystem can be calculated by the equation:

$$E_i = \frac{1}{N_{sub}} \sum_{j=1}^{N_{sub}} m_j \int_{\omega_1}^{\omega_2} S_{v_{j,i} v_{j,i}} d\omega \tag{4.18}$$

and the vector $\mathbf{E}$ of equation (4.11) is known. The injected power is calculated by solving the direct problem stated by the following equation:

$$\hat{P} = \omega \boldsymbol{\eta} \mathbf{E}. \tag{4.19}$$

$\hat{P}$ is the vector of the identified injected powers.

4.4 Force model

The previous section present a procedure allowing to identify the power injected into a structure represented by an Energy Based model. Let us remember that the purpose of this thesis is the identification of the position and of the amplitude of external forces acting on a structure. So the approach presented in this chapter allows to identify the excited subsystems (this is the counterpart of the position identification for a classical model), but it needs a law relating the injected power to the acting force in order to identify the amplitude of the exciting load.
The injected power averaged on a frequency band is defined by equation (4.17) and it can be alternatively written as:

$$P_{i,inj} = \int_{\Delta\omega} S_{ff} Re\left\{\bar{Y}(\omega)\right\} d\omega \tag{4.20}$$

where $\bar{Y}$ is the mobility averaged on the subsystem. By considering $\mathbf{S}_{ff}$ constant in band and $Re\{\bar{Y}(\omega)\}$, the real part of the mobility averaged on the band, the equation can be written as follows:

$$P_{i,inj}(\hat{\omega}) = S_{ff}(\hat{\omega}) Re\left\{\bar{Y}(\hat{\omega})\right\} \tag{4.21}$$

where $\hat{\omega}$ is the center band frequency.
So the power spectral density of the force averaged over the subsystem and over the frequency band is:

$$S_{ff}(\hat{\omega}) = \frac{P_{i,inj}(\hat{\omega})}{Re\left\{\bar{Y}(\hat{\omega})\right\}} \tag{4.22}$$

The information obtained by equation (4.22) could be not complete for some particular kind of loads as turbulent boundary layer or pressure wave propagating over the structure surface, but it is exhaustive if a "rain on the roof" load is supposed. In fact this kind of load is a random excitation with delta-correlation spatial resolution and its amplitude is proportional to the local mass density. This hypothesis implies that the force power spectral density of the force depends only on frequency and not on space [31]. Therefore, the mean square force over a frequency band is given by:

$$\langle F \rangle_{\omega}^2 = S_{ff}(\omega) \rho \Delta\omega \tag{4.23}$$

4.5 Model parameters identification

The test bed chosen to verify the efficiency of the investigated technique is the same structure used for the previous applications. Three coupled steel plates, 1.5 mm thick, laying on a soft support, are connected as shown in figure 4.3 and in table 4.1 are reported the dimensions of the structure.

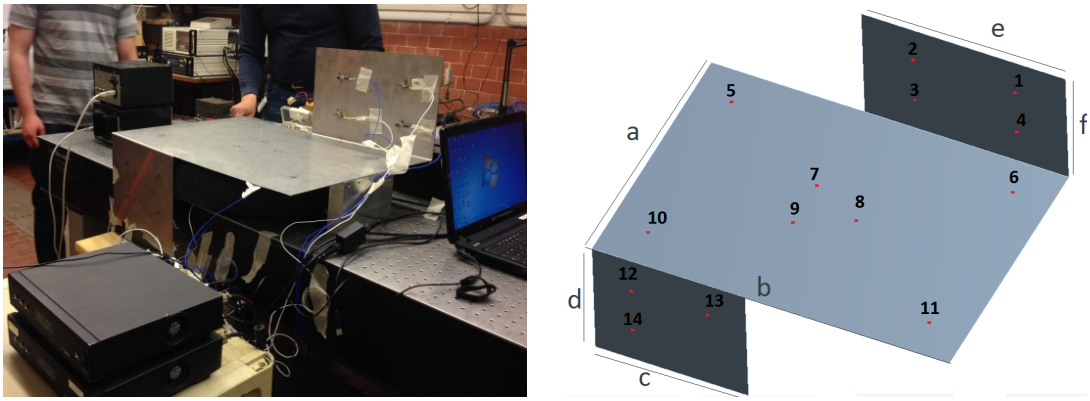

Figure 4.3: Experimental setup

Fourteen measurement points are considered on the structure: 4 on the first plate, 7 on the second plate and 3 on the third one. The distribution of the points is not uniform in space; indeed, as said also for the application showed in the previous chapter, in operative condition the uniform distribution of the acquiring points is not applicable [41].

Table 4.1: Structure dimensions

a[mm]	b[mm]	c[mm]	d[mm]	e[mm]	f[mm]
500	700	300	250	400	250

For the SEA parameters identification, fourteen independent experiments are performed. In each experiment one point, among the all set of points, is excited by random noise obtained by hammer multi impulse and the acceleration is acquired with a 5000 Hz sampling frequency for 20 seconds. This first test enables to perform PIM by the two procedures described in section 4.2. Then the quality of the identified model is verified by two tests and a last experiment is performed applying a *quasi* "rain-on-the-roof" load on the first plate. The meaning of *quasi* is: the load is imposed on different points of the first plate by two hammers, but the structure is not excited simultaneously at all points.
Each point of each subsystem is excited by a multi impulse force, and its amplitude is measured by the force transducer of the hammer. The acceleration is measured at each of the 14 points. The stored energy and the power injected are calculated for each

experiment and the parameters of the EB model are calculated by equation (4.14) and (4.15).

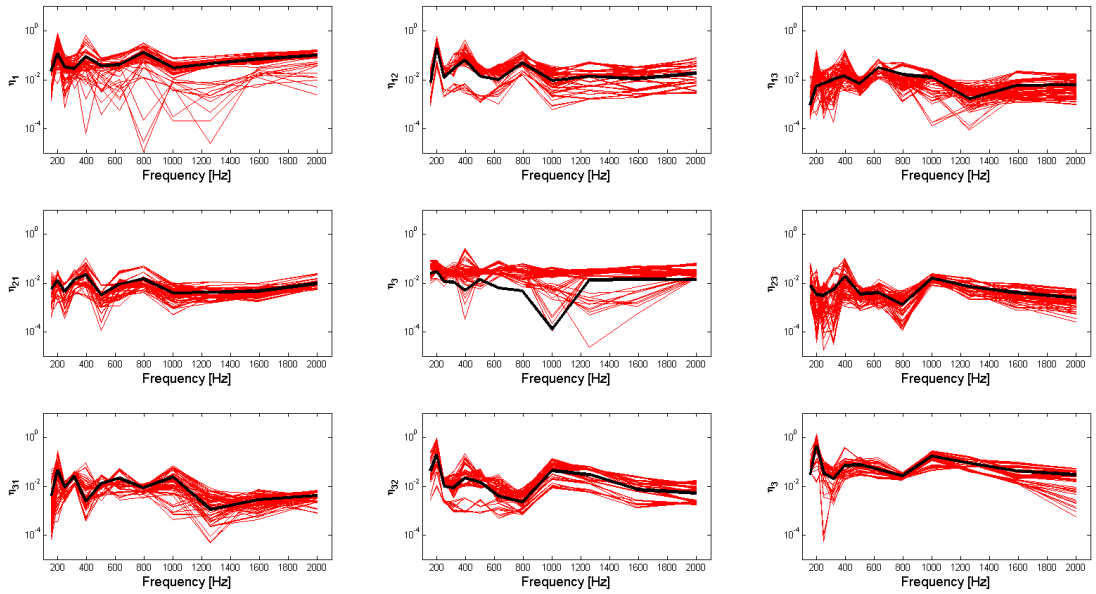

Figure 4.4: Comparison between absolute values of ILFs and CLFs computed for each measurement($--$) and their average ($--$)

Therefore, by considering all the combinations the PIM is carried out 84 times (4 first plate points for 7 second plate points for 3 third plate points) and 84 parameters sets are identified. These 84 results are averaged to obtain the CLFs and ILFs used in the model. Figure 4.4 shows the results of each experiment and their average. The effect of the ill-conditioning of the energy matrix is evaluated comparing the results obtained by the two procedures presented in section 4.2.
Figure 4.4 shows the comparison between CLFs and ILFs computed by equation (4.14) and (4.15). As shown, the parameters identified by the two methods are equal.
Another consideration must be stated for the CLF η_{13} and η_{31}. A proper SEA model expects that the CLFs of not connected subsystems is null. Since in our test bed, subsystem 1 and 3 are not linked, η_{13} and η_{31} should be null but the results show a behaviour not coherent with SEA [35]. However, let us remember that the coefficients obtained by PIM are coefficients of a EB model which is not obliged to follow SEA restrictions. In this application, the Energy Based model is a tool to identify the applied load, and a more complex formulation would frustrate the use of this technique.

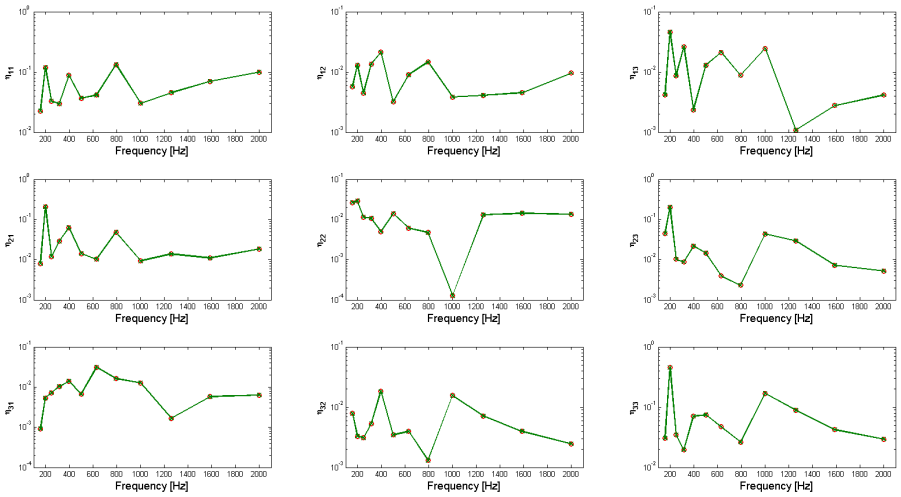

Figure 4.5: Comparison between terms of the η matrix computed by equation (4.14) ($-\mathbf{o}-$) and equation (4.15)($- \times -$)

4.6 Model validation and power identification

In this section the results of three different tests are proposed. The first test is an experimental validation of the identified parameters.
The injected power (the hammer multi impulse at each point) is identified and compared with the actual power. For a further validation of the identified model and of the possibility to use the SEA energy balance equation, a numerical test is performed. The injected power due to the application of 4 contemporary random numerical loads acting at all the 4 points of the first plate is identified.
The last test carries out the identification of the injected power, and the applied force when a rain on the roof load loads the first plate.

4.6.1 Single input/ multi output: experimental test

With the purpose to validate the results obtained from PIM, the identification of the injected power is carried out for the 14 experiments performed to identify the model parameters. In each experiment one of the 14 points of the structure is excited by a random noise obtained by hammer multi impulse, and the response is acquired at all points. Through equation (4.18) the energy of each subsystem is computed and the position and the amplitude of the injected power is identified. Figures 4.6 - 4.7 show the comparison between the sum, over the considered frequency range (100-2500 Hz), of

the identified power of the 3 subsystems.

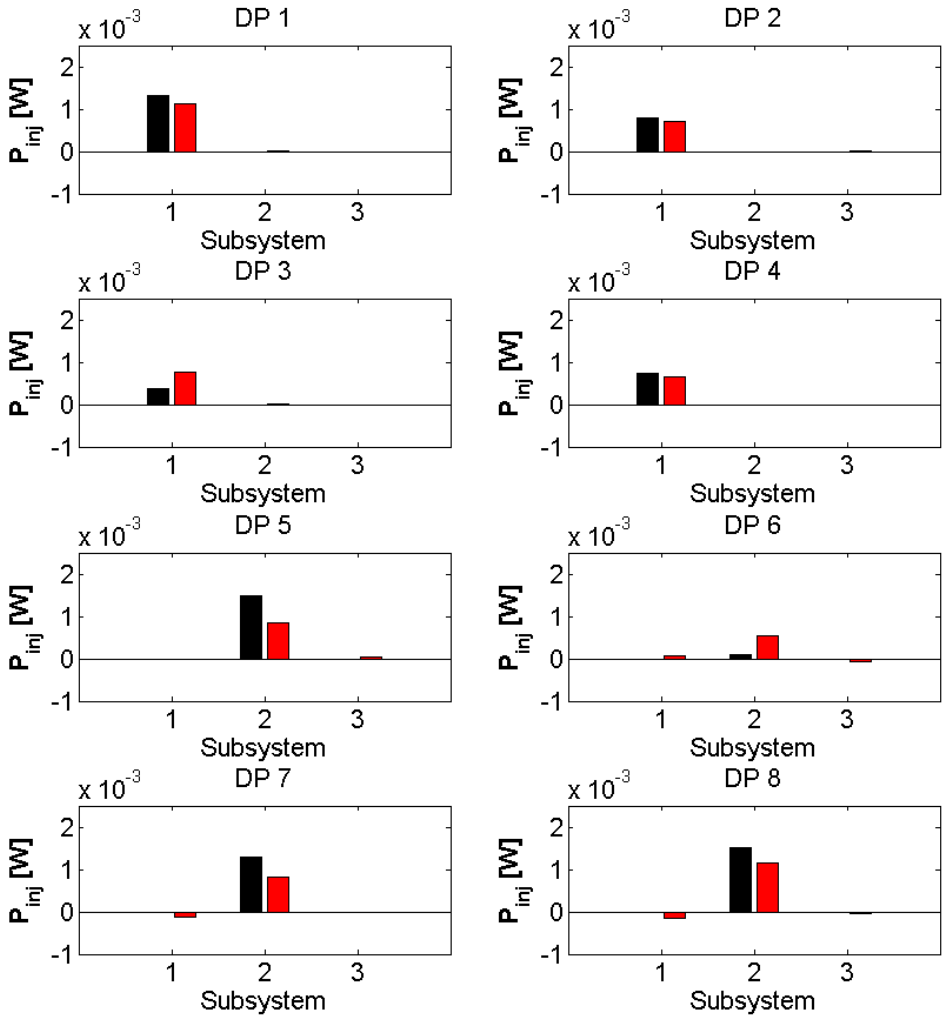

Figure 4.6: Identification of the position in SIMO experimental test: actual power (black), identified power (red)

The results show that the correct position of the power is identified for each test. The differences between the sum of the amplitudes can be assessed from the graphs shown in figures 4.8 - 4.11. Here the comparison between the actual injected power and the identified powers in correspondence of the correct subsystem is shown. It is clear that at the lower frequency bands there are large differences between the actual and the

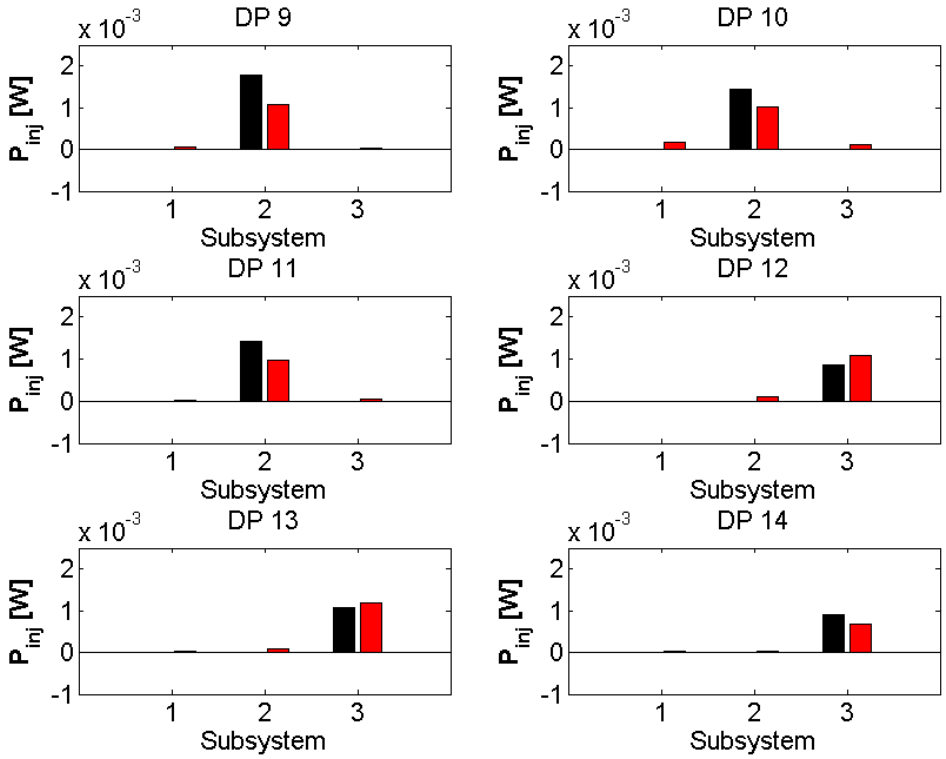

Figure 4.7: Identification of the position in SIMO experimental test: actual power (black), identified power (red)

identified powers.

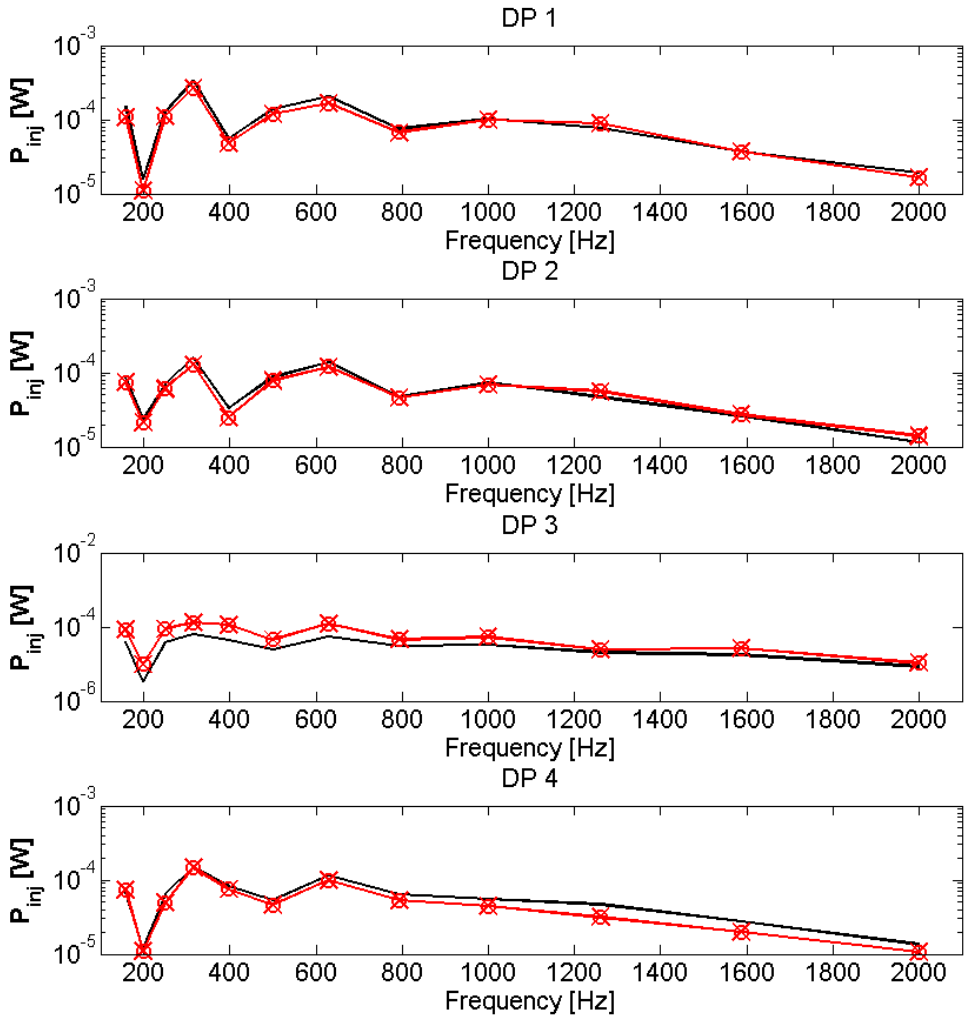

Figure 4.8: Comparison between injected power in SIMO test: actual power ($--$), identified power ($-\times-$)

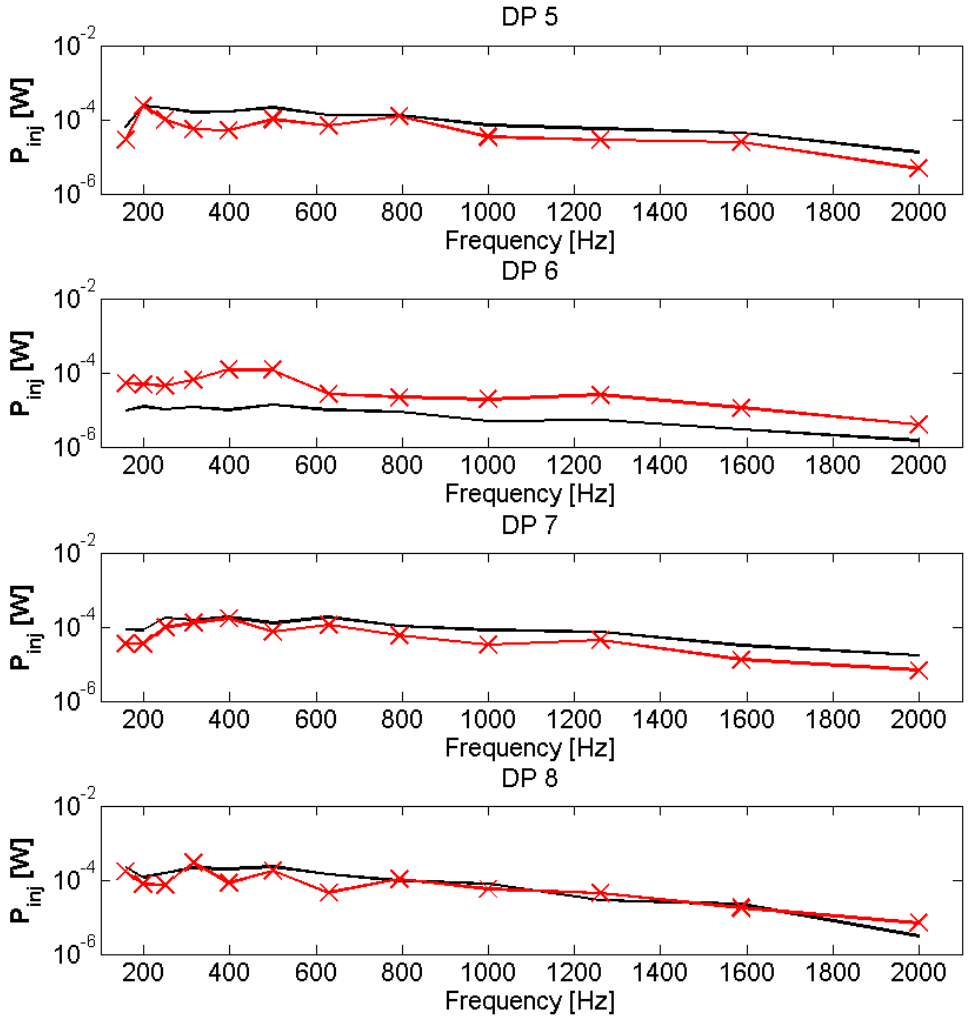

Figure 4.9: Comparison between injected power in SIMO test: actual power ($--$), identified power ($-\times-$)

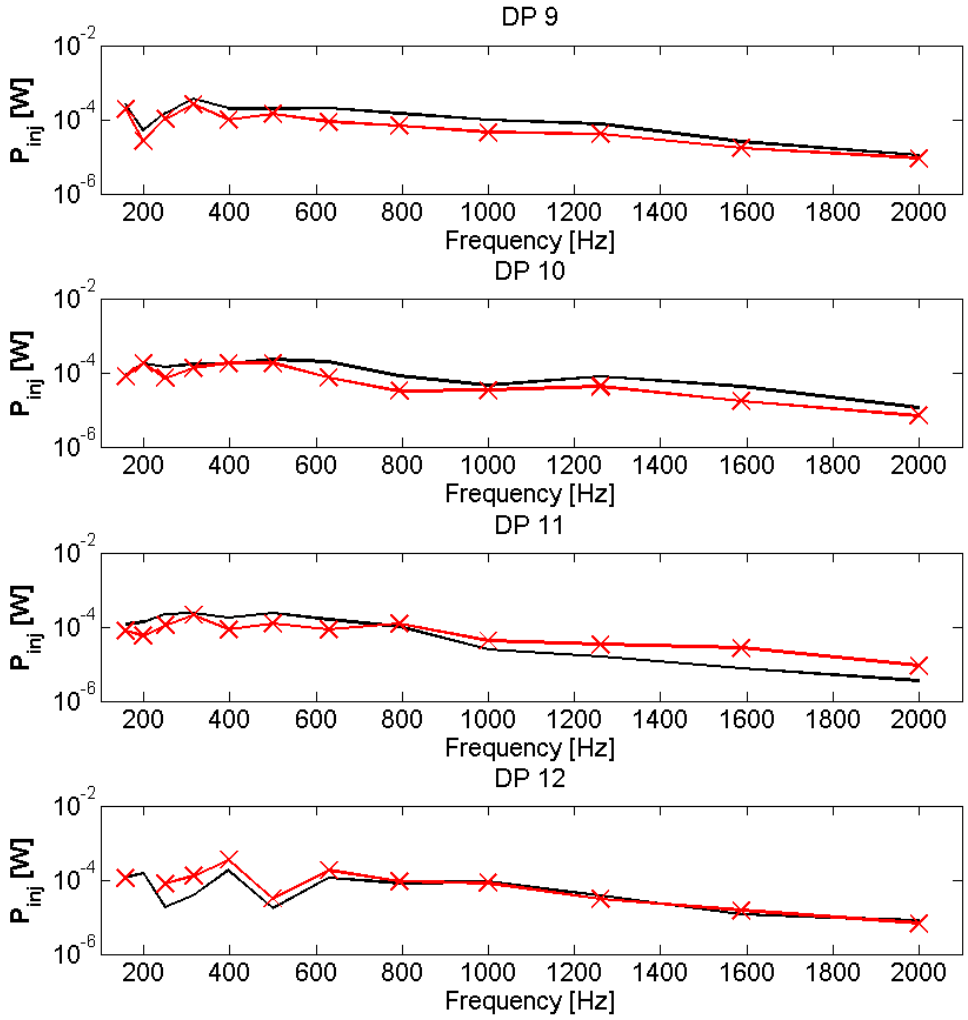

Figure 4.10: Comparison between injected power in SIMO test: actual power ($--$), identified power ($- \times -$)

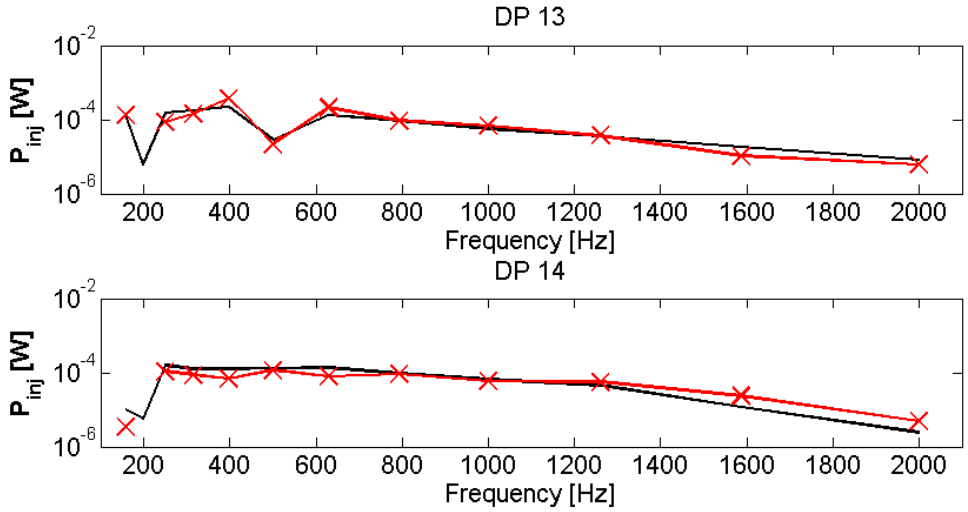

Figure 4.11: Comparison between injected power in SIMO test: actual power ($--$), identified power ($-\times-$)

4.6.2 Multi input/ multi output: numerical test

For a further validation of the identified model parameters a numerical test is carried out. The structure is excited simultaneously at all the 4 points of the subsystem 1 by 4 different random loads numerically generated and the numerical response at all the points of the structure is computed by the experimental FRF. The energy of each subsystem is calculated by equation (4.18) and the injected power is identified by equation (4.19). The sum of injected power over all the considered frequency bands is shown in figure 4.13. The actual injected power is only on subsystem 1, so the identification of the excited subsystem is successful.
Figure 4.12 displays the comparison between the actual and the identified amplitude of the injected power. Also these results validate the model obtained by PIM

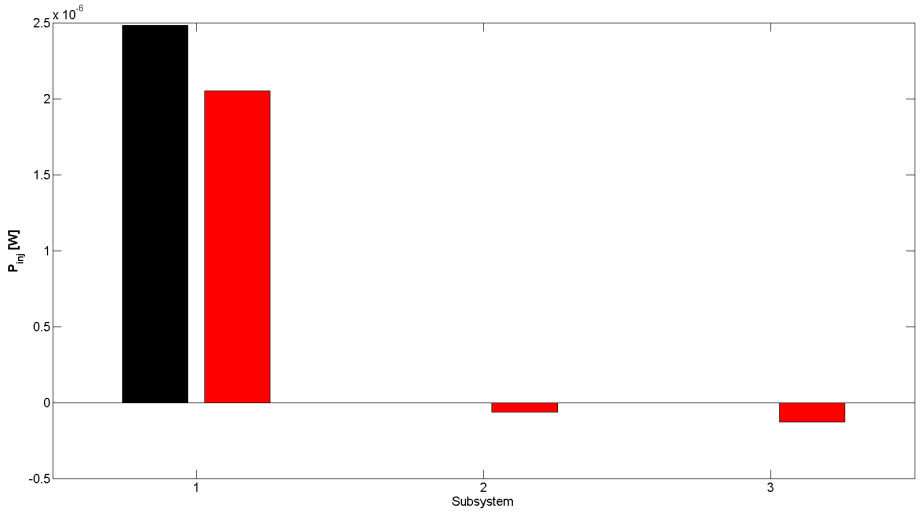

Figure 4.12: Comparison between injected power in MIMO numerical test: actual power (black), identified power (red)

From the knowledge of the identified injected power the load identification is performed by equation (4.22). The identified power spectral density of the force and the actual one are compared and shown in figure 4.14.

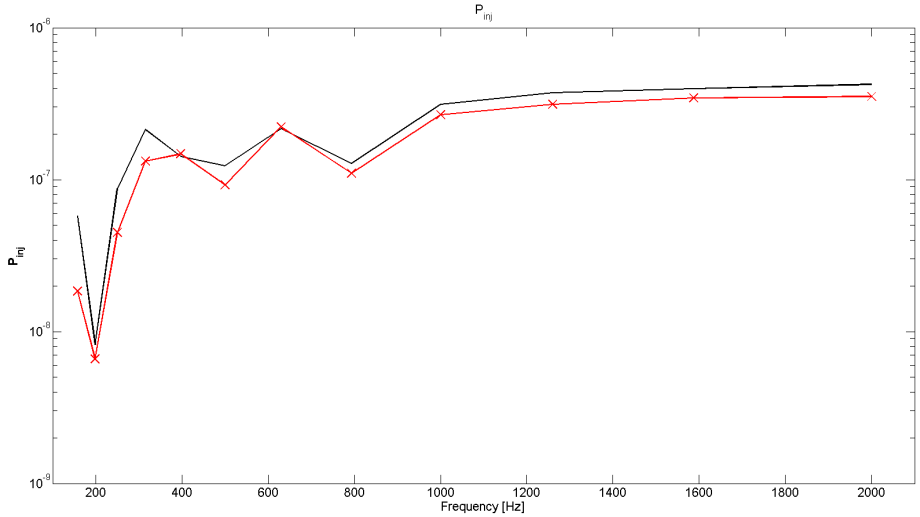

Figure 4.13: Comparison between injected power in MIMO numerical test: actual power $(--)$, identified power $(- \times -)$

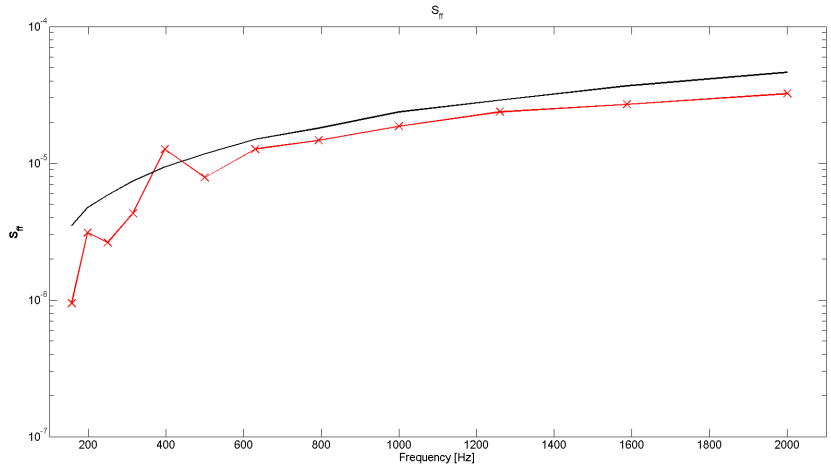

Figure 4.14: Comparison between force power spectral density in MIMO numerical test: actual S_{ff} $(--)$, identified S_{ff} $(- \times -)$

4.7 "Rain-on-the-roof": experimental test

The last test presented is an experimental test in which the structure is excited by a *quasi* "rain on the roof" load. Subsystem 1 is excited simultaneously by two uncorrelated hammer multi impulse loads. The position of the impacts changes during the measurement. The response is measured in correspondence of the whole set of points and, as in the previous test, through the knowledge of the energy of each subsystem, the injected power is identified.
The comparison of the sum over the all considered frequency range of the actual injected power versus the sum of the identified one is shown in figure 4.16. The identification of the position of the force is correct.

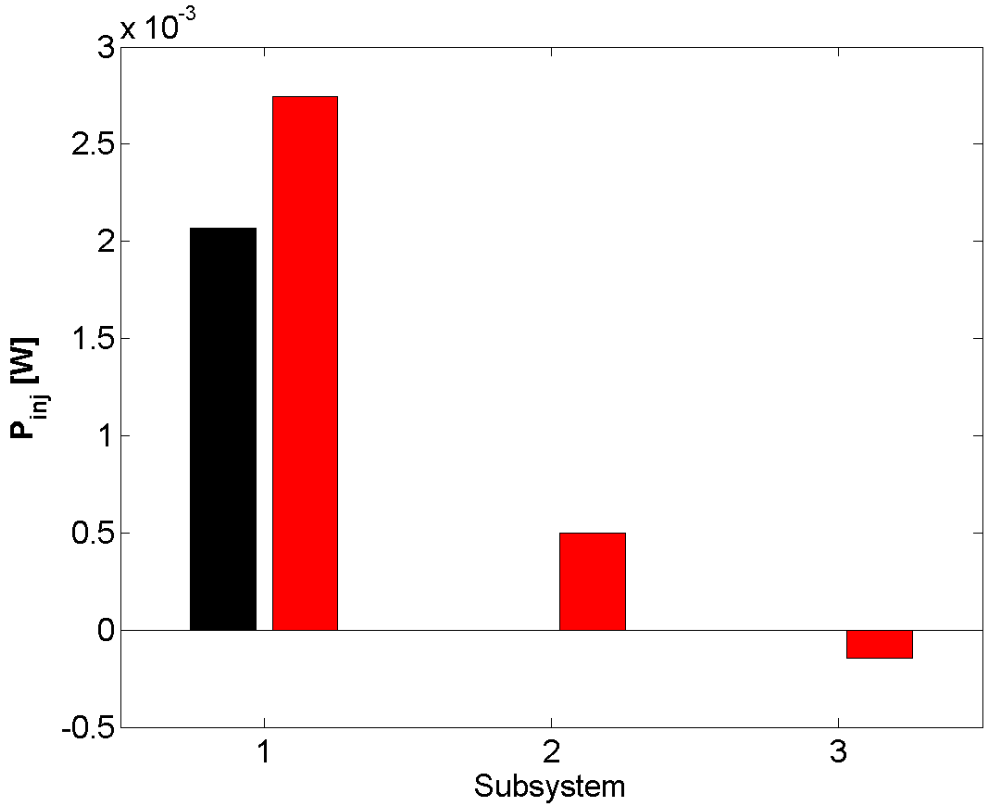

Figure 4.15: Comparison between injected power in MIMO experimental test: actual power (black), identified power (red)

Figure 4.16 shows the comparison between the amplitude of the actual and of the identified injected power at each frequency. By inverting equation (4.22), the power spectral density of the correspondent force is calculated and drawn in figure 4.17

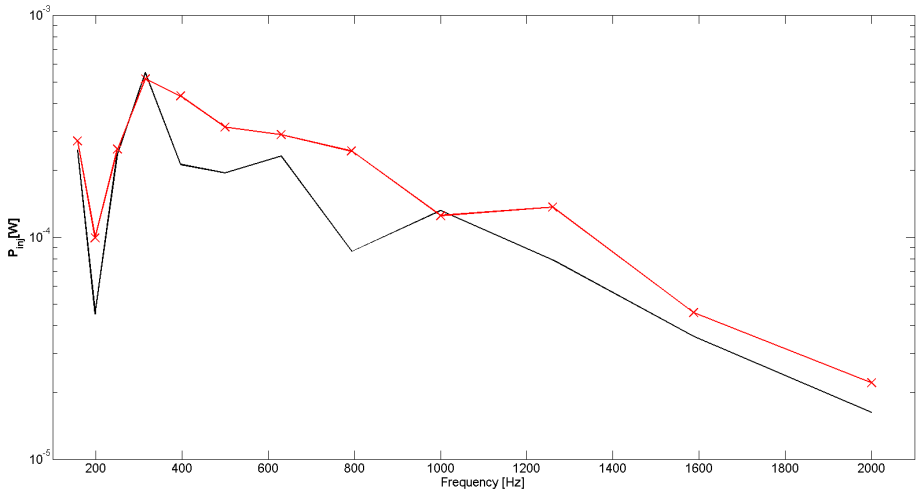

Figure 4.16: Comparison between injected power in MIMO experimental test: actual power $(--)$, identified power $(- \times -)$

As expected the identification of the power spectral density of the force is good almost at all the considered frequency bands.

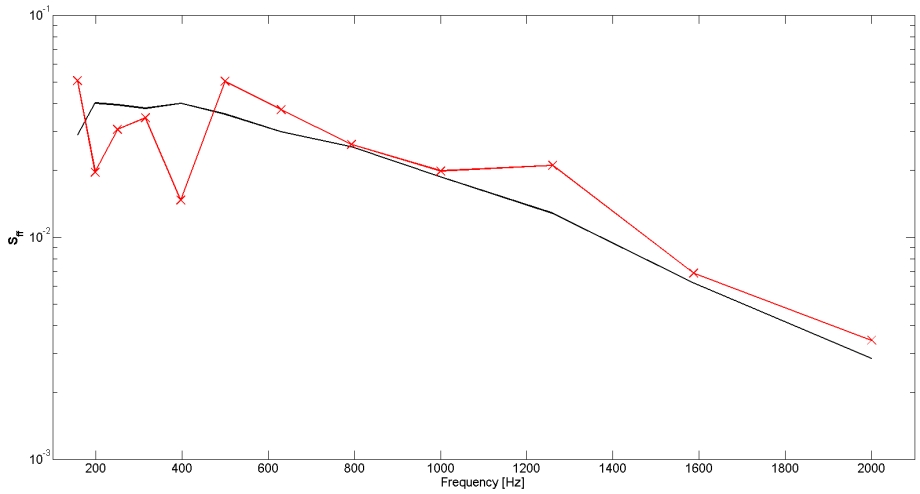

Figure 4.17: Comparison between force power spectral density in MIMO experimental test: actual S_{ff} $(--)$, identified S_{ff} $(- \times -)$

Consideration on the validity of the model

In order to establish the frequency range of SEA validity the modal overlap factor (MOF) is computed. The asymptotic modal density is computed for each subsystem by the following equation [38]:

$$n(f) = \frac{A}{2}\sqrt{\frac{12\rho(1-\nu)}{Eh^2}} \tag{4.24}$$

The modal overlap factors are calculated by equation (4.25), using the modal densities of table 4.2 and the identified ILFs.

$$MOF_i = f\,\eta_i\,n_i(f) \tag{4.25}$$

Table 4.2: Asymptotic modal densities

Subsystem 1	Subsystem 2	Subsystem 3
0,0212	0,0743	0,0159

Figure 4.18 shows the comparison between the modal overlap factor, of the whole subsystems, computed by the identified ILFs and their values averaged over all considered frequency range. As shown the modal overlap factors computed through the identified ILFs are strictly dependent on the ILFs fluctuations over the frequency; the MOFs computed by averaged ILFs is greater than one: up to 700 Hz for the subsystem 3, 800 Hz for subsystem 1 and 1100 Hz for subsystem 2.
The variance is calculated by the variance prediction method of Langley and Cotoni [42]. The energy variance is computed by the following equation:

$$\begin{aligned} Var(E_j) = \Sigma_k (D^{-1}_{0,jk})^2 Var(P_{ran,k}) + \\ + \Sigma_k \Sigma_{s\neq k} [(D^{-1}_{0,jk} - (D^{-1}_{0,js})E_s]^2 Var(D_{ran,ks}) \end{aligned} \tag{4.26}$$

The variance of the input power and of the energy matrix is evaluated by the following equations:

$$Var(P_{ran,k}) = P_{0,k}\,r^2(\alpha_k, m^1_k, B^1_k) \tag{4.27}$$

$$Var(D_{ran,ks}) = D_{0,ks}\,r^2(\alpha_{ks}, m^1_k, B^1_k) \tag{4.28}$$

where the terms r^2 is a function of the parameters α_{ks} and α_k describing the nature of the coupling between subsystems and of applied loads. It can be calculated through the following relationship:

$$\begin{aligned} r^2(\alpha, m, B) = \frac{1}{m\pi}\{\alpha - 1 + \frac{1}{2m\pi}[1 - e^{-2\pi m}] + \\ + E_1(\pi m)[cosh(\pi m) - \frac{1}{m\pi} sinh(\pi m)]\} \end{aligned} \tag{4.29}$$

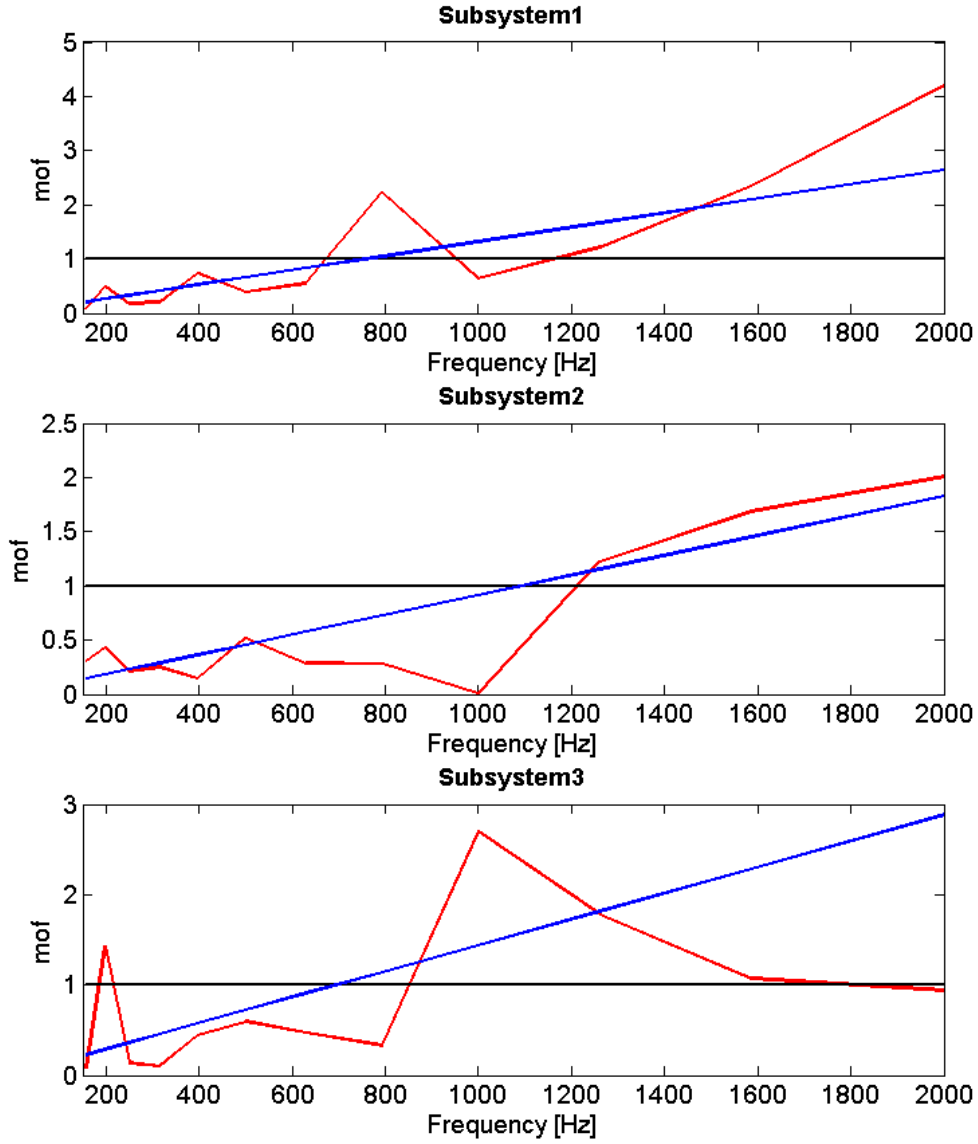

Figure 4.18: Comparison between modal overlap factors computed by identified ILF (red) and its value averaged over the frequency range (blue)

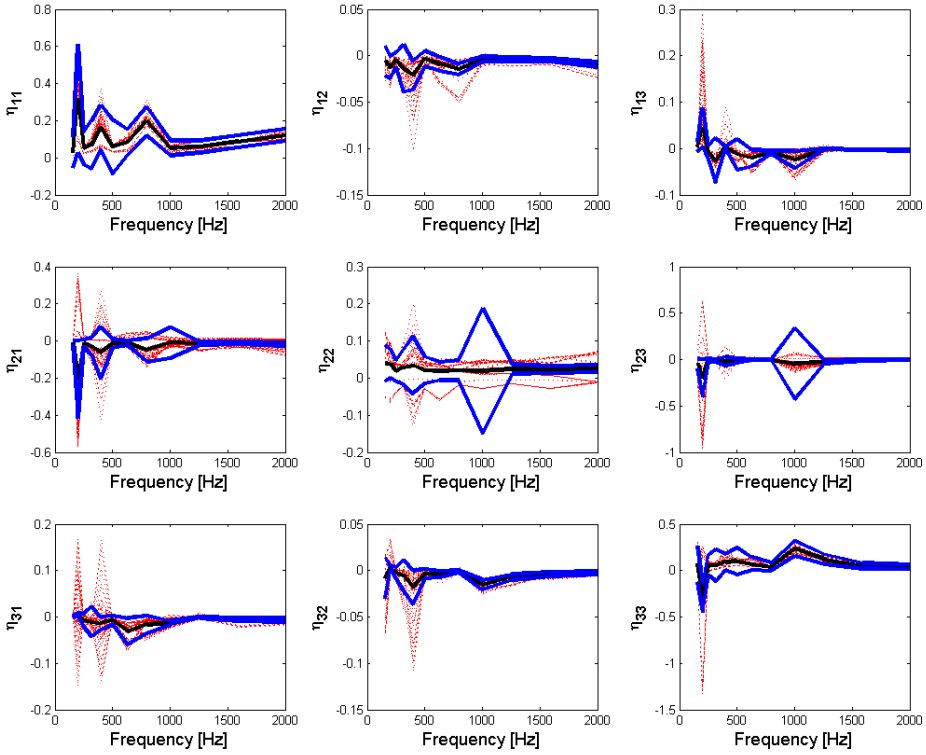

Figure 4.19: CLF matrix standard deviations bounds

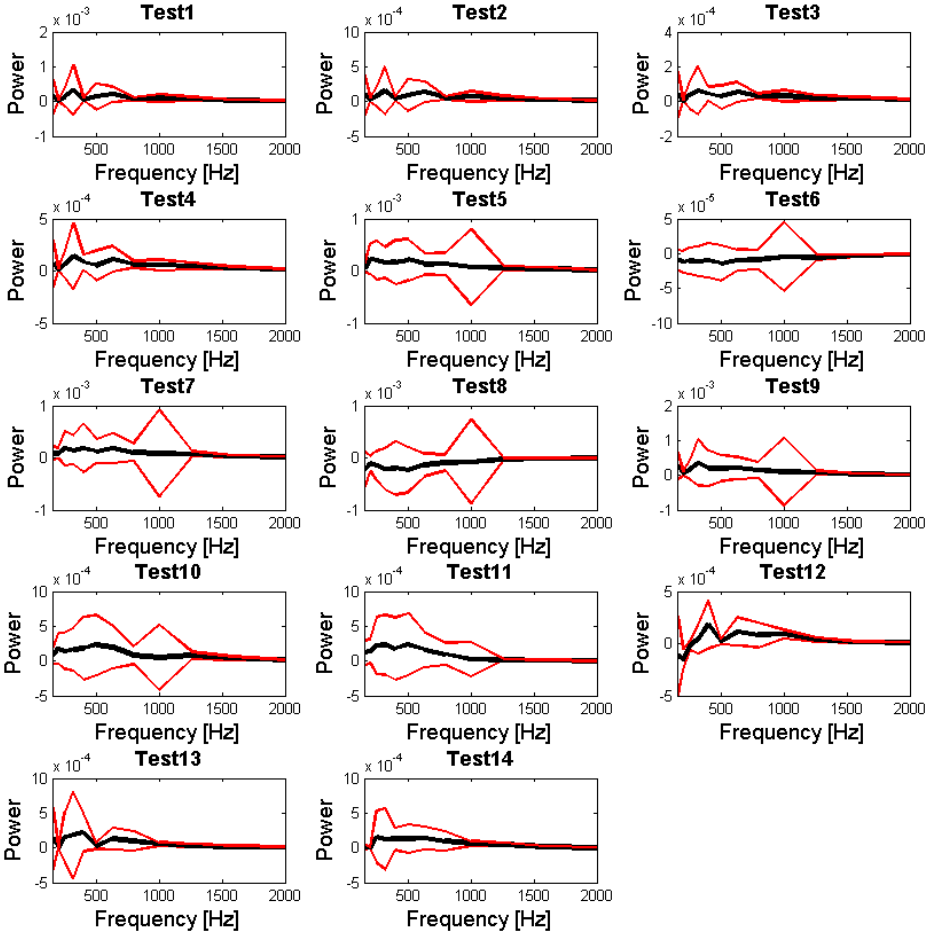

Figure 4.20: Power standard deviations bounds

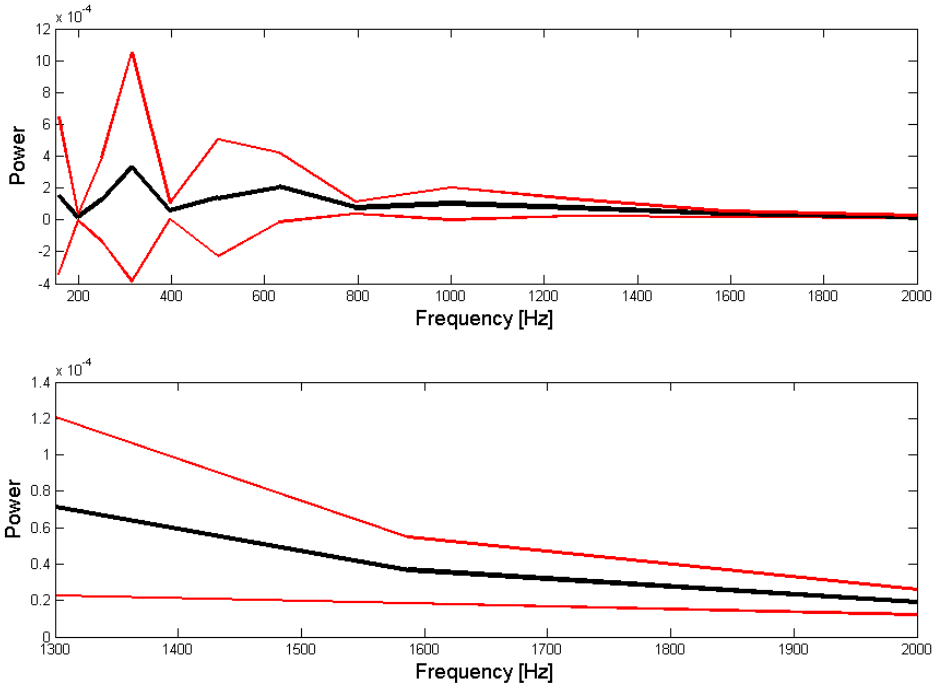

Figure 4.21: Power standard deviations bounds of test 1

The results of figure 4.19 show that most of the identified CLFs and of ILFs are in the bounds of the computed variance. Figures 4.20 shows the energy variance bounds for all the tests performed in order to use the PIM, and figure 4.21 shows the energy, together with the variance bounds, computed for the first test. These results are computed by the theoretical variance proposed for the solution of the direct SEA problem. Thus the validity of these relationship must be verify.

Conclusions In this chapter, an operative identification procedure based on Statistical Energy Analysis is presented. The procedure is carried out in two steps: the first step is focused on the identification of the coefficients of an EB model of the structure by using the Power Injection Method (PIM). The second step is the identification of the power injected by using the identified model and solving the "*inverse problem*" of the EB model. The results of three different tests are proposed. The first test is an experimental validation of the identified parameters. The second test is numerical, and gives a further validation of the identified model confirming the possibility of using SEA energy balance equation in this model. The results show that it is possible to identify the model by a reduced set of measurement points. The last test presented is an experimental test in which the structure is excited by a *quasi* "rain on the roof" load.
Since the proposed EB model is not dependent on the SEA hypotheses, it can be used also at low-medium frequencies, where the modal density is not appropriate for a SEA solution. The results show that it is possible to identify both the injected power and the PSD force on the whole frequency range, even if the best results are obtained in correspondence of higher frequency bands.
The major advantage of this technique is the possibility to have an operative load identification on very complex structures by simple models that allow to avoid the ill-conditioning of the FRF matrix and to reduce the computational costs. For example, for a very large and complex structure, where it is not possible to perform suitable experimental measurements, this technique allows to identify the subsystem excited and the amplitude of this excitation, by a lower number of information.

CHAPTER
FIVE

GENERAL CONCLUSION

In this thesis the problem of load identification in frequency domain is approached by an operative point of view. The identification of broadband deterministic and random loads is investigated and different tests are performed on both SIMO and MIMO models. The first part of the thesis is focused on the study of a low frequency problem. First the relationship between the degrees of freedom taken into account and the ill-conditioning of the FRF matrix are investigated through a numerical procedure, based on SVD regularization technique. This methodology is focused on the identification of the best experimental setup to perform load identification. It is carried out by numerical and experimental FRF, and the results show that, even if the computational cost is high, it gives an indication about the best distributions of measurement points that allow to perform load identification.
While in the first part of chapter two the analysis is based on the results obtained from the numerical identification, in the second part of the chapter the relationship between the selected degrees of freedom and the ill-conditioning of the problem is directly investigated. The results show that, when a broadband load must be identified, the reduction of the ill-conditioning by cutting not essential degrees of freedom could be a way to proceed; in fact, it gives good results also by considering a little subset of measuring points coincident or not with the drive points. On the contrary this methodology fails when random forces must be identified. The results obtained from the identification of the injected power suggest that, for non deterministic loads, an energetic approach could be more efficient.
In the third chapter a coherence based approach is proposed, to identify random loads. The procedure is performed in three steps and both SIMO and MIMO applications are presented. First the number of acting forces is identified; this number is computed through the analysis of the measured velocity coherence of the responses. As shown from the results of the experimental tests, the $N_{sources}$ index gives the number of acting loads. In this thesis only the cases of one and two forces are studied, but we are confident that similar results can be obtained for a higher number of forces, because the velocity coherence must decrease when the number of input increases. The second step, of the

proposed procedure, is the identification of the position obtained by C_{vf} index; it is computed by applying dummy uncorrelated forces at all the points of the structure and by the virtual coherence between these dummy forces and the measured velocities. The results obtained by the tests carried out on the whole set of points show that, since the number of acting forces is correctly established, the C_{vf} index allows to identify the position of the actual forces.
Once the number and the position of acting forces is identified it is possible to calculate their amplitudes as the ratio between the measured PSD velocity and the square of the absolute value of the mobility in correspondence of the selected points. The use of SISO formulation allows to bypass the ill-conditioning of the FRF matrix, in that its inversion is not required.
For both the considered cases (SIMO and MIMO), the identification is also executed with a reduced measurement points set, in order to evaluate the limit of the proposed procedure: the measurement points could either be or not drive points. Also in this case the analysis of the velocity coherence, obtained through the $N_{sources}$ index, gives a good indication about the number of acting load. It must be noticed that C_{vf} index, by definition, can be computed only in correspondence of the measurement points, and indeed the knowledge of the PSD velocity is required.
In the single input/ multi output model the procedure has been slightly changed. The reference force is calculated in correspondence of the point selected by the index. This allows to excite numerically the structure to calculate the relative error between the actual PSD velocity and that computed by the identified forces. The minimum value of the error corresponds to the position of the identified force that gives the dynamic responses nearest to the measured ones.
In the multi input/ multi output model the use of the index does not give good results. The knowledge of the number of applied loads allows to consider all the exciting points combination. Then a load (its amplitude is computed by the inversion of classical formulation for random loads) is numerically applied on the structure and the correct position is given by the minimization of the relative error computed for each combination. This procedure is obviously expensive in terms of computational costs.
The forth chapter is focused on the identification at high frequencies. An operative identification procedure based on Energy Based/Statistical Energy Analysis model is presented. The procedure is performed in two steps: the first step is focused on the identification of the coefficients of the EB model of the structure by using the Power Injection Method. The second step is the identification of the power injected by using the identified model and solving the "*inverse problem*" of the EB model. The model parameters are identified by experimental measurements; then, to validate the identified model, the results of two different tests are presented. First, the injected power is identified using the measured PSD velocity used in the identification of the model parameters. The second test is a numerical test: four different random loads are numerically generated and applied simultaneously on the four points of the first subsystem, then the numerical PSD velocity is computed through the experimental FRF. The injected power and the PSD force are identified and are compared to the actual ones. The result of this

test gives a further validation of the identified model and confirms the possibility to use the SEA energy balance equation. The last presented test is an experimental test: the first subsystem is excited by a quasi "rain on the roof" load generated by two hammer multi impulse. The comparison between the actual injected power and the identified one shows a good agreement.
The comparison between the results obtained from the second and the last test shows that in the numerical test, where the PSD force grows with the frequency, the best results are obtained in correspondence of the highest frequency bands; while in the experimental test, where the PSD force decreases with the frequency, it does not happen.
The major advantage of this technique is the possibility to have operative load identification on very complex structures by simple models that allow to avoid the ill-conditioning of the FRF matrix and to reduce the computational cost. For example, for a very large and complex structure, where it is not possible to perform suitable experimental measurements, this technique allows to identify the subsystem excited and the amplitude of this excitation, by a lower information.

ACKNOWLEDGEMENTS

This work is supported by the University of Rome "La Sapienza".

BIBLIOGRAPHY

[1] T Uhl. The inverse identification problem and its technical application. *Archive of Applied Mechanics*, 77(5):325–337, 2007.

[2] J Hadamard. Lectures on cauchy's problem in linear partial differential equations, 1923.

[3] Hyuk Lee and Youn-sik Park. Error analysis of indirect force determination and a regularisation method to reduce force determination error. *Mechanical Systems and Signal Processing*, 9(6):615–633, 1995.

[4] J.A Fabunmi. Effects of structural modes on vibratory force determination by the pseudoinverse technique. *AIAA journal*, 24(3):504–509, 1986.

[5] C Pezerat and JL Guyader. Two inverse methods for localization of external sources exciting a beam. *Acta Acustica*, 3(1):1–10, 1995.

[6] C Pezerat and J.L Guyader. Force analysis technique: reconstruction of force distribution on plates. *Acta Acustica united with Acustica*, 86(2):322–332, 2000.

[7] Q Leclere and C Pézerat. Vibration source identification using corrected finite difference schemes. *Journal of Sound and Vibration*, 331(6):1366–1377, 2012.

[8] Q Leclère, F Ablitzer, and C Pézerat. Practical implementation of the corrected force analysis technique to identify the structural parameter and load distributions. *Journal of Sound and Vibration*, 351:106–118, 2015.

[9] A Fregolent and A Sestieri. Force identification from vibration measurements in the wavenumber domain. *Proceeding of ISMA 21*, pages 517–526, 1996.

[10] A Fregolent. *Problemi mal condizionati di dinamica strutturale*. PhD thesis, University of Rome "La Sapienza", Rome, 2 1994. An optional note.

[11] S.R Ibrahim, A Fregolent, and A Sestieri. Structural force identification at unmeasured locations. *Proceedings-Spie The International Society for Optical Engineering. Spie International Society for Optical*, pages 927–933, 1996.

[12] G H Golub and C Reinsch. Singular value decomposition and least squares solutions. *Numerische mathematik*, 14(5):403–420, 1970.

[13] P.A Nelson and Seong-Ho Yoon. Estimation of acoustic source strength by inverse methods: Part i, conditioning of the inverse problem. *Journal of sound and vibration*, 233(4):639–664, 2000.

[14] P.C Hansen. Regularization tools: A matlab package for analysis and solution of discrete ill-posed problems. *Numerical algorithms*, 6(1):1–35, 1994.

[15] MP Ekstrom and RL Rhoads. On the application of eigenvector expansions to numerical deconvolution. *Journal of Computational Physics*, 14(4):319–340, 1974.

[16] G.H Golub, P. C Hansen, and D. P O'Leary. Tikhonov regularization and total least squares. *SIAM Journal on Matrix Analysis and Applications*, 21(1):185–194, 1999.

[17] P. C. Hansen. The truncated svd as a method for regularization. *BIT Numerical Mathematics*, 27(4):534–553, 1987.

[18] P.C Hansen. Truncated singular value decomposition solutions to discrete ill-posed problems with ill-determined numerical rank. *SIAM Journal on Scientific and Statistical Computing*, 11(3):503–518, 1990.

[19] Frank Bauer and Stefan Kindermann. The quasi-optimality criterion for classical inverse problems. *Inverse Problems*, 24(3):035002, 2008.

[20] Seong-Ho Yoon and Philip A Nelson. Estimation of acoustic source strength by inverse methods: Part ii, experimental investigation of methods for choosing regularization parameters. *Journal of sound and vibration*, 233(4):665–701, 2000.

[21] G.H Golub, M Heath, and G Wahba. Generalized cross-validation as a method for choosing a good ridge parameter. *Technometrics*, 21(2):215–223, 1979.

[22] S. Milana, A. Fregolent, and A. Culla. Observation dof's optimization for structural forces identification. In *Model Validation and Uncertainty Quantification, Volume 3*, pages 27–34. Springer, 2015.

[23] P Donello. Identificazione delle forze agenti su una struttura complessa. Master's thesis, University of Rome "La Sapienza", Rome, 7 2014.

[24] SY Khoo, Z Ismail, KK Kong, ZC Ong, S Noroozi, WT Chong, and AGA Rahman. Impact force identification with pseudo-inverse method on a lightweight structure for under-determined, even-determined and over-determined cases. *International Journal of Impact Engineering*, 63:52–62, 2014.

[25] K Shin and J Hammond. *Fundamentals of signal processing for sound and vibration engineers*. John Wiley & Sons, 2008.

[26] A Le Bot. *Foundation of statistical energy analysis in vibroacoustics*. OUP Oxford, 2015.

[27] J.S Bendat and A.G Piersol. *Random data: analysis and measurement procedures*, volume 729. John Wiley & Sons, 2011.

[28] M Fontul, AMR Ribeiro, JMM Silva, and NMM Maia. Transmissibility matrix in harmonic and random processes. *Shock and Vibration*, 11(5, 6):563–571, 2004.

[29] YE Lage, NMM Maia, MM Neves, and AMR Ribeiro. Force identification using the concept of displacement transmissibility. *Journal of Sound and Vibration*, 332(7):1674–1686, 2013.

[30] Yun-Lai Zhou, E Figueiredo, N Maia, and R Perera. Damage detection and quantification using transmissibility coherence analysis. *Shock and Vibration*, 2015, 2015.

[31] B Mace. Statistical energy analysis, energy distribution models and system modes. *Journal of Sound and Vibration*, 264(2):391–409, 2003.

[32] F.J Fahy. An alternative to the sea coupling loss factor: rationale and method for experimental determination. *Journal of Sound and Vibration*, 214(2):261–267, 1998.

[33] K De Langhe and P Sas. Statistical analysis of the power injection method. *The Journal of the Acoustical Society of America*, 100(1):294–303, 1996.

[34] R.H Lyon. *Theory and application of statistical energy analysis*. Elsevier, 2014.

[35] GM Gladwell and Frank Fahy. Iutam symposium on statistical energy analysis, 8-11 july 1997, programme. Technical report, DTIC Document, 1997.

[36] A Culla, W D'Ambrogio, A Fregolent, and S Milana. Medium-high frequency optimization using sea sensitivity. In *ISMA 2014 International Conference on Noise and Vibration Engineering*, 2014.

[37] A Culla, A Fregolent, W D'Ambrogio, and S Milana. Vibroacoustic optimization using a statistical energy analysis model. *Journal of Sound and Vibration*, 375:102–114, 2016.

[38] S De Rosa, F Franco, and F Ricci. *Introduzione alla tecnica statistico-energetica (SEA) per la dinamica strutturale e l'acustica interna*. Attuale-LIGUORI Editore srl Via Posillipo 394 80123 NAPOLI (Italy)., 1999.

[39] A Culla and A Sestieri. Is it possible to treat confidentially sea the wolf in sheep's clothing? *Mechanical systems and signal processing*, 20(6):1372–1399, 2006.

[40] A Culla and A Sestieri. Energy flow analysis in vibrating systems by laser vibrometer measurements. In *Fifth International Conference on Vibration Measurements by Laser Techniques*, pages 199–206. International Society for Optics and Photonics, 2002.

[41] S Milana and A Culla. Load identification by operational statistical energy analysis inverse approach. In *ISMA2016, International Conference on Noise and Vibration Engineering*, 2016.

[42] Robin S Langley and Vincent Cotoni. Response variance prediction in the statistical energy analysis of built-up systems. *The Journal of the Acoustical Society of America*, 115(2):706–718, 2004.

LIST OF TABLES

2.1 Structure dimensions 11
2.2 Coordinates of the selected points 11
2.3 Configuration of the points selected for the numerical test 14
2.4 I_{AVG} obtained by numerical simulation with different configurations, indices averaged over frequency and drive points 16
2.5 I_{NORM} obtained by numerical simulation with different configurations, indices averaged over frequency and drive points 17
2.6 Selected points in experimental setup 20
2.7 Configuration of the points selected for the experimental test 23
2.8 I_{NORM} obtained by experimental FRF with different configurations, indices averaged over frequency and drive points 24
2.9 I_{AVG} obtained by experimental FRF with different configurations, indices averaged over frequency and drive points 24
2.10 Condition number of FRF at the two considered frequencies 26
2.11 point load identification 29
2.12 Distributed load identification 31

3.1 SIMO identification: whole measurement points set. Number of excited points k 47
3.2 Selected measurement points 52
3.3 SIMO identification: reduced measurement points set. Number of excited points k 52
3.4 MIMO identification: whole measurement points set. Number of excited points k 57
3.5 MIMO identification: reduced measurement points set. Number of excited points k 59

4.1 Structure dimensions 71
4.2 Asymptotic modal densities 84

LIST OF FIGURES

1.1 Input-Output model 4
1.2 Comparison between the filters factor of different regularisation techniques 8
1.3 L-curve. 9

2.1 Test structure 11
2.2 Diagram of the numerical identification procedure 12
2.3 Comparison between indices obtained by numerical simulation with different configurations, indices averaged over frequency and drive points. . . 15
2.4 Comparison between I_{AVG} obtained by numerical simulation for the configuration 50, indices averaged over frequency and drive points 18
2.5 Comparison between I_{AVG}(red) and I_{NORM} (blue) obtained by numerical simulation for the configuration 50, indices averaged over frequency and drive points 18
2.6 Experimental setup 19
2.7 Measurement chain 19
2.8 Comparison between numerical frequency response function(blue) and experimental one (red). 20
2.9 Comparison between indices obtained by experimental FRF with different configurations, indices averaged over frequency and drive points. 21
2.10 Comparison between indices obtained for the best configuration (Conf. 32) by numerical FRF (blue) and experimental FRF (red) 22
2.11 Comparison between FRF matrices at 99 Hz and 661 Hz (resonance) . . . 25
2.12 Comparison between condition numbers:
72 DoF FRF(blue), and 24 DoF FRF(red). 26
2.13 Comparison between FRF matrices, 72 DoF and 24 DoF, at 99 Hz and at 661 Hz (resonance) 27
2.14 Comparison between singular values at 661 Hz. 72 DoF FRF matrix (blue), and 24 DoF FRF matrix (red). 28
2.15 Condition number of FRF matrix:
n=m=24 (green) and *n=24, m=8* (blue) 30

2.16 Deterministic point loads: comparison between the actual force ($-\times-$), the force identified in the case *n=m=24* (green) and in the case *n=24, m=8* (blue) . . . 31
2.17 Deterministic distributed loads: comparison between the actual force($-\times-$), the identified in the case *n=m=24* (green) and in the case *n=24, m=8* (blue) . . . 32
2.18 Diagram of the numerical identification procedure . . . 33
2.19 Random point loads. Comparison between the actual force ($-\times-$), the identified force in the case *n=m=24* (green) and in the case *n=24, m=8* (blue) . . . 35
2.20 Random point loads. Comparison between the actual force ($-\times-$) and the identified force in the case *n=24, m=8* (blue) . . . 36
2.21 Random point loads. Comparison between the actual injected power ($-\times-$), the identified power in the case *n=m=24* (red) and in the case *n=24, m=8* (blue) . . . 37
2.22 Random distributed load. Comparison between the actual force ($-\times-$), the identified force in the case *n=m=24* (green) and in the case *n=24, m=8* (blue) . . . 37
2.23 Random distributed load. Comparison between the actual force ($-\times-$) and the identified force in the case and *n=24, m=8* (blue) . . . 38
2.24 Random distributed loads. Comparison between the actual injected power ($-\times-$), the identified power in the case *n=m=24* (red) and in the case *n=24, m=8* (blue) . . . 38

3.1 Single Input/ Multi Output system . . . 41
3.2 Multi Input/ Multi Output system . . . 43
3.3 Diagram of the identification procedure . . . 45
3.4 Test bed . . . 46
3.5 Single input/ multi output identification: whole measurement points set. $1/C_{vf}$ averaged on the whole frequency band . . . 48
3.6 Single input/ multi output identification: whole measurement points set. Comparison between S_{ff}: actual PSD force ($-*-$), PSD force identified by equation (3.19)($-\mathbf{o}-$) and PSD force identified by equation by equation (2.12)($--$) . . . 49
3.7 Single input/ multi output identification: whole measurement points set. Comparison between the actual PSD force S_{ff} ($-*-$), the PSD force identified by equation (2.12) at the correct point($-\mathbf{o}-$) and the PSD force identified at the other points ($-$)for test 4. . . . 50
3.8 Single input/ multi output identification: whole measurement points set. Comparison between the actual PSD force S_{ff} ($-*-$), the PSD force identified by equation (3.19)($-\mathbf{o}-$) and the PSD force identified by equation (2.12)($--$) at point 4 . . . 50

3.9 Single input/multi output identification: whole measurement points set. Comparison between the actual PSD velocity S_{vv} ($-*-$), the PSD velocity computed by PSD force identified by equation (3.19) ($-\mathbf{o}-$) 51
3.10 Single input/ multi output identification: reduced measurement points set. Comparison between the actual PSD force S_{ff} ($-*-$), the PSD force identified by equation (3.19)($-\mathbf{o}-$), the PSD force identified by equation (2.12)(-) 54
3.11 Single input/ multi output identification: reduced measurement points set. Comparison between the actual PSD force ($-*-$), the PSD force identified by equation (3.19) ($-\mathbf{o}-$)and the PSD force identified by equation (2.12)(-) 55
3.12 Single input/ multi output identification: reduced measurement points set. Comparison between the actual PSD velocity S_{vv} ($-*-$) and the PSD velocity computed by the PSD force identified by equation (3.19) ($-\mathbf{o}-$) 56
3.13 Multi input/ multi output identification: whole measurement points set. $1/C_{vf}$ averaged on the whole frequency band 57
3.14 Multi input/ multi output identification: whole measurement points set. Comparison between the actual forces PSD S_{ff_1} (*blue*), S_{ff_2} (black) and the forces PSD identified $S_{ff_{id_1}}$ (red) and $S_{ff_{id_2}}$ (green) 58
3.15 Multi input/ multi output identification: whole measurement points set. Comparison between the actual PSD velocity S_{vv} ($-\mathbf{o}-$)and the PSD velocity identified by equation (3.19)($-\times-$) 59
3.16 Multi input/ multi output identification: reduced measurement points set. Error computed for each configuration of points in the first test (blue) and in the second test (red) 60
3.17 Multi input/ multi output identification: reduced measurement points set. Comparison between the actual PSD velocity S_{ff_1} (*blue*), S_{ff_2} (black) and the forces PSD identified $S_{ff_{id_1}}$ (red) and $S_{ff_{id_2}}$ (green) 61
3.18 Multi input/ multi output test. Comparison between actual PSD velocity S_{vv} ($-\mathbf{o}-$)and the PSD velocity computed by the PSD force identified by equation (3.19) ($-\times-$) 61

4.1 Two Degrees of Freedom system 64
4.2 Two subsystems SEA model 66
4.3 Experimental setup 71
4.4 Comparison between absolute values of ILFs and CLFs computed for each measurement($--$) and their average ($--$) 72
4.5 Comparison between terms of the η matrix computed by equation (4.14) ($-\mathbf{o}-$) and equation (4.15)($-\times-$) 73
4.6 Identification of the position in SIMO experimental test: actual power (black), identified power (red) 74

4.7 Identification of the position in SIMO experimental test: actual power (black), identified power (red) 75
4.8 Comparison between injected power in SIMO test: actual power (−−), identified power (− × −) 76
4.9 Comparison between injected power in SIMO test: actual power (−−), identified power (− × −) 77
4.10 Comparison between injected power in SIMO test: actual power (−−), identified power (− × −) 78
4.11 Comparison between injected power in SIMO test: actual power (−−), identified power (− × −) 79
4.12 Comparison between injected power in MIMO numerical test: actual power (black), identified power (red) 80
4.13 Comparison between injected power in MIMO numerical test: actual power (−−), identified power (− × −) 81
4.14 Comparison between force power spectral density in MIMO numerical test: actual S_{ff} (−−), identified S_{ff} (− × −) 81
4.15 Comparison between injected power in MIMO experimental test: actual power (black), identified power (red) 82
4.16 Comparison between injected power in MIMO experimental test: actual power (−−), identified power (− × −) 83
4.17 Comparison between force power spectral density in MIMO experimental test: actual S_{ff} (−−), identified S_{ff} (− × −) 83
4.18 Comparison between modal overlap factors computed by identified ILF (red) and its value averaged over the frequency range (blue) 85
4.19 CLF matrix standard deviations bounds 86
4.20 Power standard deviations bounds 87
4.21 Power standard deviations bounds of test 1 88